

I. A STUDY OF VACANCIES IN QUENCHED  
TUNGSTEN

II. DESIGN AND CONSTRUCTION OF A  
FIELD ION MICROSCOPE SYSTEM WITH A MULTIPLE  
SAMPLE CAPABILITY

Thesis for the Degree of Ph. D.  
MICHIGAN STATE UNIVERSITY  
MOHSEN KHOSHNEVISAN  
1973



This is to certify that the

thesis entitled

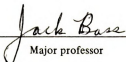
- I. A STUDY OF VACANCIES IN QUENCHED TUNGSTEN  
II. DESIGN AND CONSTRUCTION OF A FIELD ION  
MICROSCOPE SYSTEM WITH A MULTIPLE SAMPLE  
CAPABILITY

presented by

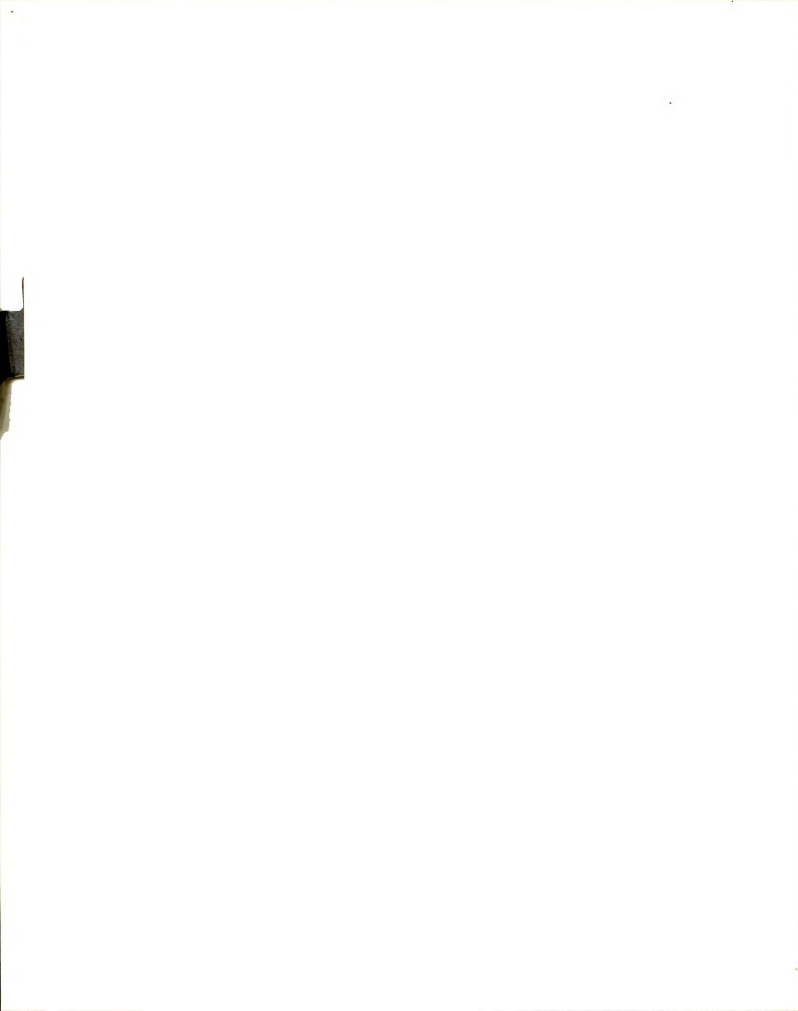
**Mohsen Khoshnevisan**

has been accepted towards fulfillment  
of the requirements for

Ph. D. degree in Physics

  
Major professor

Date May 18, 1973



## ABSTRACT

### I. A STUDY OF VACANCIES IN QUENCHED TUNGSTEN

### II. DESIGN AND CONSTRUCTION OF A FIELD ION MICROSCOPE SYSTEM WITH A MULTIPLE SAMPLE CAPABILITY

By

Mohsen Khoshnevisan

I. We have studied the dependence of quenched-in resistances upon quench temperature and quenching speed for a fine wire of very pure single crystal tungsten quenched under superfluid helium, and for a number of pure polycrystalline wires quenched under superfluid helium and in an ultra-high ( $p < 1.5 \times 10^{-9}$  torr) vacuum. The vacuum quenches yielded results substantially the same as those obtained for superfluid helium quenches, thereby eliminating external impurities as the source of the observed quenched-in resistances. We ascribe these resistances to vacancies trapped in the samples by the rapid quench. Extrapolation of the data to infinite quench speed produced a vacancy formation energy larger than the value of 3.3eV proposed by Schultz. Analysis in terms of the theory of Flynn, Bass, and Lazarus yielded a vacancy formation energy of  $3.6 \pm 0.2$ eV and a vacancy motion energy of  $2.5 \pm 0.5$ eV, assuming an activation energy for



self-diffusion of  $6.1 \pm 0.3\text{eV}$ . We have also examined the isochronal annealing spectrum after quenches from above 2800K. Over 80% of the quenched-in resistance annealed away in a single, narrow stage, centered in the temperature range 850 to 1150K. After quenches from below 3100K, this stage was centered in the upper portion of this temperature range and contained essentially all of the quenched-in resistance. After quenches from higher temperatures, the annealing stage shifted toward lower temperatures, and some resistance remained after the stage was completed. Finally, isothermal annealing studies were made in the range 800 to 1040K after quenches from above 3200K. The isothermal annealing curves had a complex shape--the rate of annealing initially increasing with increasing annealing time. Measurements of changes in the rate of annealing upon changing the annealing temperature yielded an activation energy for migration of  $1.5 \pm 0.2\text{eV}$ . This is considerably smaller than the high temperature estimate of 2.5eV for the single vacancy motion energy. This low activation energy, the complex form of the isothermal annealing curves, and the persistence of some quenched-in resistance to high temperatures during isochronal annealing are all suggestive of vacancy clustering during the quench and subsequent annealing. These results confirm and extend those previously obtained by Gripshover for less pure samples. The apparent inconsistency between our conclusion that

clustering is important, and Gripshover's tentative conclusion that it is not, can be traced to the then accepted value of 5.2eV used by Gripshover for the activation energy of self diffusion in tungsten. Analysis of his data using the more recently obtained value of 6.1eV yields results entirely consistent with our interpretation. In order to observe single vacancies and vacancy clusters directly, we began to design and construct a field ion microscope system.

II. An outline is given of the basic principles of a new method for loading multiple samples into a field ion microscope, which allows sequential examination of the samples without loss of cooling or degradation of vacuum. Two operating systems are described: a liquid nitrogen cooled, glass high vacuum microscope with a four sample capacity; and a liquid helium cooled, all metal ultra-high vacuum microscope with a five sample capacity.

The experimental techniques for quantitative defect studies in a field ion microscope are also described. These include techniques for screen and sample preparation for the microscope, pulsed field evaporation of the tip, recording of the atomic details on 35mm movie film after each pulse, and the analysis of the resulting data.



I. A STUDY OF VACANCIES IN QUENCHED TUNGSTEN

II. DESIGN AND CONSTRUCTION OF A FIELD ION MICROSCOPE  
SYSTEM WITH A MULTIPLE SAMPLE CAPABILITY

By  
Mohsen Khoshnevisan

A THESIS

Submitted to  
Michigan State University  
in partial fulfillment of the requirements  
for the degree of

DOCTOR OF PHILOSOPHY

Department of Physics

1973

6172801

## ACKNOWLEDGMENTS

I would like to express my appreciation to my advisor, Dr. Jack Bass, for his invaluable advice, encouragement, and assistance throughout the course of this work. I am indebted to Dr. J. M. Galligan for kindly supplying us with the very pure 2.4 mil tungsten specimen used in our investigation. I wish to thank Dr. C. H. Stephan for his assistance in the development of our field ion microscope (FIM) system, and for many helpful discussions.

Thanks are also due Mr. Earl Stone for his assistance in our vacuum quenching experiments and FIM sample preparation, Dr. John Zetts for assistance in taking much of our superfluid helium quenching data, Mr. M. Ford for designing our FIM temperature control unit and for valuable design suggestions for the sample rotator in our metal FIM, and Mr. R. Anderson for designing the camera control and pulse shaper circuits for our FIM system.

The ultra-high vacuum chamber and metal FIM double dewar system were designed at Michigan State University and built by Varian Associates.

I would like to acknowledge the financial support of the Atomic Energy Commission, and the National Science

Foundation. I would also like to acknowledge the Cornell group of Profs. Seidman and Balluffi for providing us with valuable information on FIM techniques.

Finally, I wish to express my deepest appreciation to my wife, Beverly, whose encouragement and support have been invaluable. I am also deeply indebted to her for her assistance in preparing this manuscript.



# TABLE OF CONTENTS

	page
LIST OF TABLES.....	vi
LIST OF FIGURES.....	vii
I. INTRODUCTION.....	1
A. Quenching in Superfluid Helium.....	1
B. Need for Further Experiments.....	2
II. A STUDY OF VACANCIES IN QUENCHED TUNGSTEN.....	6
A. Introduction.....	6
B. Determination of $E_f$ from the Quenching Data.....	6
C. Determination of $E_m$ .....	8
D. Motivation for the Present Investigation.....	11
E. Superfluid Helium Quench Data for the 2.4 mil Diameter Sample.....	13
1. Data for Fastest Quenching Speeds.....	14
2. Control of the Quenching Speeds.....	15
3. Dependence of the Quenched-in Resistance Upon the Quenching Speed.....	19
4. Extrapolation to Infinite Quench Speed Using PBL Theory.....	24
F. Annealing Data for the 2.4 mil Sample.....	29
1. Isochronal Annealing Studies.....	29
2. Isothermal Annealing with Change-of-Slope Measurements.....	32
G. Interpretation of the Data in Terms of Vacancies.....	36
H. The Effect of Contaminants on the Resistivity Data.....	40
J. Need for Further Experiments.....	43
K. Comparison of Ultra-High Vacuum and Superfluid Helium Quenches.....	46
L. Conclusions.....	50
M. Present State of our PIM Studies.....	55





	page
III. DESCRIPTION OF THE ULTRA-HIGH VACUUM SYSTEM.....	57
A. Introduction.....	57
B. The Pumping System.....	58
C. The Vacuum Chamber.....	62
IV. THE FIELD ION MICROSCOPE SYSTEM.....	64
A. Introduction.....	64
B. Motivation for Inclusion of Multiple Samples in a FIM.....	67
C. Selective Shielding.....	69
D. Sample Rotator for a Liquid Nitrogen Cooled Glass FIM.....	74
E. The All-Metal Liquid Helium Cooled FIM.....	78
F. Final Comments on the Sample Rotator.....	85
G. Image Intensification.....	86
H. Experimental Techniques.....	92
1. Preparation of a Conductive Transparent Coating on the FIM Screen.....	93
2. Deposition of Phosphor Powder on the Screen.....	94
3. Preparation of FIM Samples.....	96
J. Data Acquisition and Analysis System.....	100
1. Data Acquisition System.....	101
2. Data Analysis System.....	105
LIST OF REFERENCES.....	107
APPENDIX A Basic Principles of the Field Ion Microscope.....	111



## LIST OF TABLES

Table	Page
II-1 COMPARISON OF SELF DIFFUSION, QUENCHING, AND ANNEALING DATA FOR GOLD AND TUNGSTEN.....	38



## LIST OF FIGURES

Figure	Page
II-1 FAST QUENCH DATA FOR THE 2.4 MIL SAMPLE. FOR COMPARISON, GRIPSHOVER'S DATA FOR A 1.0 MIL AND A 1.2 MIL SAMPLE AND SCHULTZ'S DATA FOR A 1.2 MIL SAMPLE ARE ALSO SHOWN.....	15
II-2 QUENCH PICTURES FOR THE 2.4 MIL DIAMETER TUNGSTEN WIRE QUENCHED FROM 2800K. THE FAST QUENCH WAS MADE WITH NO PARALLEL CAPACITOR. THE SLOWER QUENCHES WERE MADE USING 8.5mf AND 29.7mf CAPACITORS RESPECTIVELY.....	18
II-3 DEPENDENCE OF QUENCHING RATE UPON QUENCH TEMPERATURE FOR THE 2.4 MIL DIAMETER TUNGSTEN WIRE.....	20
II-4 VARIATION OF QUENCHED-IN RESISTANCE WITH QUENCHING SPEED FOR THE 2.4 MIL. DIAM. WIRE.....	21
II-5 VARIATION OF QUENCHED-IN RESISTANCE WITH QUENCH TIME FOR QUENCHES FROM 2800K AND 3100K.....	22
II-6 PLOT OF $1/T_{9.8}$ VERSUS $1/T$ FOR 50% LOSS, USING THE VALUE FOR $E_f$ SHOWN IN FIGURE II-4. THE RECTANGLES REPRESENT OUR BEST ESTIMATE OF UNCERTAINTY FOR EACH POINT.....	27
II-7 ISOCHRONAL ANNEALS OF THE 2.4 MIL DIAMETER TUNGSTEN WIRE. THE SAMPLE WAS HELD FOR 10 MINUTES AT EACH ANNEALING TEMPERATURE.	
II-8 DETERMINATION OF ACTIVATION ENERGIES FOR MIGRATION USING THE 2.4 MIL DIAMETER TUNGSTEN WIRE. THE WIRE WAS QUENCHED FROM 3255K. THE BREAK IN THE DATA ARISES FROM A LOSS OF RESISTANCE DUE TO ACCIDENTAL HEATING OF THE SAMPLE TO A HIGHER TEMPERATURE THAN PLANNED.....	33



II-9	COLLECTED ACTIVATION ENERGIES FOR LOW TEMPERATURE MIGRATION, FOR OUR 2.4 MIL SAMPLE AND FOR GRIPSHOVER'S 1.0 MIL SAMPLES ALL QUENCHED FROM ABOVE 3200K. THE OPEN SYMBOLS REPRESENT VALUES OBTAINED UPON DECREASING THE ANNEALING TEMPERATURE. THE FILLED SYMBOLS REPRESENT VALUES OBTAINED UPON INCREASING THE ANNEALING TEMPERATURE.....	35
II-10	SAMPLE HOLDER FOR ULTRA-HIGH VACUUM AND SUPERFLUID HELIUM QUENCHES.....	47
II-11	ULTRA-HIGH VACUUM (OPEN SYMBOLS) AND SUPERFLUID (FILLED SYMBOLS) FAST QUENCH DATA FOR A NUMBER OF 1.0 AND 1.2 MIL. DIAMETER TUNGSTEN WIRES.....	49
II-12	PROPOSED SCHEME FOR PERFORMING TWO SETS OF FIM STUDIES TO ANALYZE VARIOUS INTERPRETATIONS FOR THE QUENCHED-IN RESISTIVITY DATA.....	52
III-1	SCHEMATIC DIAGRAM OF THE PUMPING SYSTEM AND THE VACUUM CHAMBER.....	59
III-2	SCHEMATIC DIAGRAM OF THE VACUUM CHAMBER AS VIEWED FROM ABOVE.....	63
IV-1	THE BASIC MULTI-SAMPLE SYSTEM; A SAMPLE WHEEL SURROUNDED BY HIGH VOLTAGE AND GROUNDED SHIELDS.....	71
IV-2	(AFTER MÜLLER AND NISHIKAWA) DEPENDENCE OF THE SHIELDING FACTOR $S$ UPON $L/d$ FOR A SHIELD AT THE SAME POTENTIAL AS THE FIM TIP.....	73
IV-3	SCHEMATIC DRAWING OF A SAMPLE ROTATOR SYSTEM FOR A LIQUID NITROGEN COOLED GLASS FIM. THE HIGH VOLTAGE AND GROUNDED SHIELDS ARE SHOWN SEPARATELY.....	75
IV-4	SCHEMATIC DRAWING OF A SAMPLE ROTATOR SYSTEM FOR A LIQUID HELIUM COOLED METAL FIM.....	80
IV-5	THE DESIGN OF HIGH VOLTAGE AND GROUNDED SHIELDS AND A HOLDER FOR THE GLASS ROD USED TO CONNECT THE MAGNETIC ROTATOR SYSTEM TO THE WORM GEAR..	81





Figure	Page
IV-6 DESIGN OF THE CHANNEL PLATE HOLDER AND BIASING CIRCUIT.....	89
IV-7 EXAMINATION OF FIM TIPS BY OBSERVATION OF FRESNEL FRINGES (SHOWN GREATLY EXAGGERATED) AROUND THE TIPS.....	99
IV-8 BLOCK DIAGRAM OF THE DATA AQUISITION SYSTEM....	102
A-1 SCHEMATIC DIAGRAM OF A GLASS FIELD ION MICROSCOPE.....	112
A-2 ONE DIMENSIONAL POTENTIAL ENERGY DIAGRAMS FOR FIELD IONIZATION.....	114
A-3 (AFTER MÜLLER); MOTION OF THE IMAGING GAS ATOMS NEAR THE TIP SURFACE.....	120



## I. INTRODUCTION

### A. Quenching in Superfluid Helium

In 1969 R. J. Gripshover completed a thesis entitled A STUDY OF VACANCIES IN TUNGSTEN QUENCHED IN SUPERFLUID HELIUM. In this thesis he described the results of experiments on several 1.0 and 1.2 mil diameter polycrystalline tungsten wires quenched from various temperatures and at various speeds into 1.2K superfluid helium. The resistivity quenched into these wires was measured and additional experiments were carried out to study the manner in which this resistivity disappeared when the samples were subsequently heated to sequentially increasing temperatures. On the basis of his measurements Gripshover concluded that single vacancies were retained during the quench, and that these vacancies became mobile in the temperature range 800-1000K, apparently annealing away without substantial clustering. He noted that he could obtain reproducible data only for samples exceeding a minimum purity, and that his purest samples were only modestly purer than the minimum.

The present thesis began when we were fortunate to obtain a 2.4 mil diameter wire of high purity single crystal tungsten kindly supplied by Dr. J. M. Galligan of Brookhaven National Laboratory. Since specimen purity had been a source of concern throughout Gripshover's work, we



decided to attempt to reproduce and extend his measurements using this higher purity sample. As we will describe in detail in Chapter II below, our experimental data basically agreed with Gripshover's, indicating that once the minimum purity specified by Gripshover was exceeded, the quenched-in resistivities were not too sensitive to further increase in purity. On the other hand, both portions of our data, as well as new experimental results obtained in other laboratories(1)(2), called into question Gripshover's conclusion that vacancy clustering was not important in quenched tungsten. Rather, the new information gave substantial reason to believe that low temperature annealing of vacancies in tungsten is a complex process, probably involving clustering.

#### B. Need for Further Experiments

The experience of fifteen years of quenching studies of metals strongly suggested that resistivity measurements alone would not provide an understanding of either the nature or properties of vacancies in a metal where substantial clustering occurs. For this reason we decided to supplement further measurements of quenched-in resistivity with direct observations of vacancies and their clusters in a field ion microscope (FIM). To carry out this program we began construction of a unique FIM, with a multi-sample capacity. The advantages of such an FIM are described in Chapter IV below.

While we were designing this FIM, a challenge was



raised to our assertion that the resistivity quenched into our tungsten wires was due to vacancies. This challenge arose from measurements made upon the metal molybdenum (3)(4), for which quenches from high vacuum into a liquid metal yielded no quenched-in resistance and no vacancy loops when quenched samples were examined in an electron microscope. Based upon the physical and chemical similarity between W and Mo, it was argued that we must be observing not vacancies, but rather some impurity retained in solution during the quench. Recently, from an argument made by Lidiard,\* the possibility that helium atoms may diffuse through metals by becoming trapped in vacancies (and thus stabilize them during the superfluid quenches) became somewhat plausible.\*\* This possibility became even more plausible when Kimura (7) more recently obtained quenched-in resistances for Mo wires quenched in superfluid helium.

These results lend themselves to at least four alternative interpretations;

- 1) The experiments using superfluid helium involve an unknown contaminant and no vacancies--this is Evan's interpretation(8). This unknown impurity can be either internal to the samples or external, i.e. it enters the

---

\*In a recent note, Lidiard (5) argued that vacancies are effective traps for helium atoms, and that trapped helium atoms tend to stabilize vacancy clusters.

\*\*Inert gases are generally believed to be insoluble in metals (6).





samples from the quenching environment. In either case, the impurity can exist in the host lattice either substitutionally or interstitially.

2) Helium gas atoms can occupy vacant sites in the W and Mo lattices and thereby stabilize vacancies during a superfluid helium quench.

3) In analogy with #2 above, it may be possible that interstitial impurities other than helium (e.g. carbon) can occupy vacancies and thereby stabilize them during the quenches.

4) The resistivity quenched into the sufficiently pure W and Mo samples quenched in superfluid helium is due to vacancies alone.

We therefore re-oriented our research program to produce a decision in favor of one of these four alternatives. A careful examination of these alternatives showed that to make a decision in favor of one of them would require other experiments (e.g. quenches in an ultra-high vacuum ( $p < 10^{-8}$  torr)) in addition to superfluid helium quenches and FIM studies (see parts J and L in Chapter II). The FIM project was then expanded to construction of a dual system, useful both as a FIM and as an ultra-high vacuum quenching chamber.

The work presented in this thesis was carried out over a period of about 3 1/2 years, and in three separate stages: first, we reproduced and expanded Gripshover's



superfluid quenching experiments using Dr. Galligan's very pure specimen; next, we designed and constructed a FIM system (two multi-sample capability microscopes, data acquisition and analysis facilities) for quantitative defect studies; and finally we carried out a series of ultra-high vacuum quenches using the ultra-high vacuum system of our metal FIM.

The thesis is organized as follows:

In Chapter II we report our superfluid helium quench data, make a comparison with Gripshover's data, and interpret the data in terms of vacancies. The results of our ultra-high vacuum quenching studies are discussed, and used to eliminate some of the above alternative possibilities. Finally, suggestions are offered for future experiments to provide information needed to make the correct choice from the remaining alternatives.

The description of the experimental apparatus is given in Chapters III and IV. The dual purpose ultra-high vacuum system is described in Chapter III, and in Chapter IV we describe our unique internal sample rotator for a FIM, show how it has been included in our glass and all-metal microscopes, and finally describe our data acquisition and analysis system for quantitative FIM studies.

In order to familiarize the reader with the operation of a FIM, the basic principles of field ion microscopy are briefly described in Appendix A.



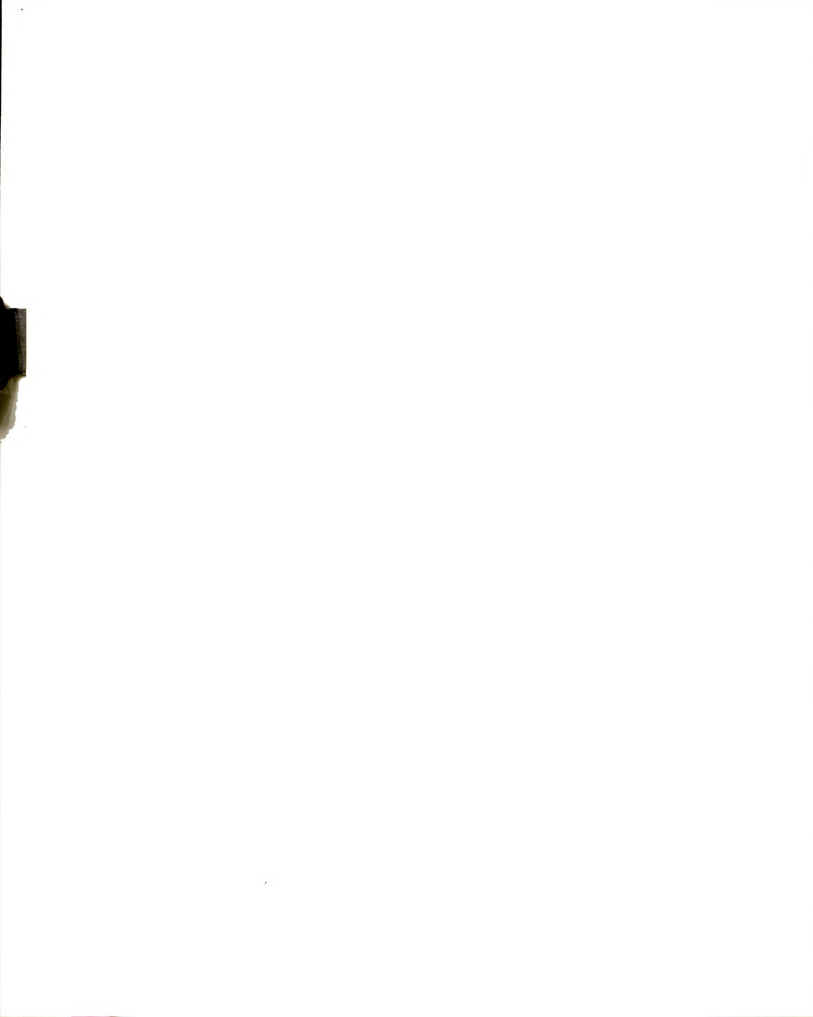
## II. A STUDY OF VACANCIES IN QUENCHED TUNGSTEN

### A. Introduction

Studies of the properties of single vacancies standardly focus upon two quantities, the vacancy formation energy  $E_f^V$  and the vacancy motion energy  $E_m^V$ . Information regarding  $E_f^V$  and  $E_m^V$  can be deduced from measurements made on any property of the material which is affected by the existence of vacancies. Resistivity is one such property which is also relatively easy to measure precisely (for other types of measurements see references (9)(10)(11)). Since performing resistivity measurements is the most common experimental method for studying vacancies and has been used throughout our investigation, we will briefly describe this method and indicate how the values for  $E_f^V$  and  $E_m^V$  are deduced from the data. Detailed descriptions of this technique, as well as the experimental equipment, have already been presented in a thesis by R. J. Grips-hover (12).

### B. Determination of $E_f^V$ from the Quenching Data

The fractional concentration of single vacancies  $C_v(T)$  in a pure material in thermal equilibrium at absolute



temperature  $T$  can be written in terms of the vacancy formation energy  $E_f^V$  as (13)

$$C_V(T) = n_0 \exp(-E_f^V/kT) \quad (1)$$

where  $n_0$  is a constant, and  $k$  is Boltzmann's constant.

When a specimen at a high temperature  $T_Q$  is quenched sufficiently rapidly to a lower temperature where vacancies are not mobile, most of the vacancies present before the quench can be trapped. The increase in the resistivity of the material due to the quenched-in vacancies can then be measured at lower temperatures (usually in a liquid helium bath where the lattice resistance is small and does not mask the vacancy contribution to the resistance).

This increase in the resistivity,  $\Delta\rho$ , is measured with respect to the base (vacancy-free) resistivity, which is obtained by annealing the wire at high temperatures (i.e. heat the sample to high temperatures and cool slowly) to allow all of the vacancies to migrate to the sinks.\* If it is assumed that the quenched-in resistivity is due to single vacancies alone, and that each vacancy contributes the same amount to the resistivity, then Equation 1 can

---

\*The base resistivity of new samples is initially achieved by annealing the samples several times at high temperatures. It is considered to be a stable base when its value remains constant within 1% upon any further annealing.





be written in the form:

$$\Delta \rho = \rho_0 \exp(-E_f^V/kT_q) \quad (2)$$

where  $\rho_0$  is a constant. From Equation 2 a plot of  $\ln(\Delta \rho)$  versus  $1/T_q$  will be linear with a slope of  $-E_f^V/k$ , provided that all of the vacancies present at  $T_q$  are quenched-in. Since quenching with a finite speed is not expected to retain all of the vacancies present at  $T_q$  (particularly for high temperature quenches), we will refer to the value of  $E_f^V$  obtained from such a plot as the "effective formation energy" to distinguish it from the "correct" value which would be obtained with quenches at infinite speed. As will be described later, by observing the dependence of the quenched-in resistance on the quench speed one can extrapolate to infinite quench speed and get a better estimate of the "correct" value of  $E_f^V$ .

### C. Determination of $E_m^V$

Experimental values for  $E_m^V$  using resistivity measurements can be obtained in the following ways:

- 1) If self diffusion in the material occurs via the diffusing atoms changing places with single vacancies (which appears to be the case for many metals), the activation energy for self diffusion,  $Q$ , can be shown to be



related to  $E_f^V$  and  $E_m^V$  by (14)

$$Q = E_f^V + E_m^V \quad (3)$$

Values for  $Q$  can be obtained from radioactive tracer measurements of self diffusion. If  $E_f^V$  is known (e.g. from the procedure described above),  $E_m^V$  can be deduced from Equation 3.

2) A second method for estimating  $E_m^V$  involves observation of how the quenched-in resistivity due to excess vacancies disappears as the sample is annealed. There are two annealing procedures generally used to determine motion energies: isochronal annealing and isothermal annealing. An isochronal anneal consists of heating the specimen for a fixed time at each of a series of increasing temperatures until most of the quenched-in resistivity anneals out. This gives recovery as a function of the annealing temperature. An isothermal anneal consists of heating the specimen to a fixed temperature to monitor the recovery as a function of the annealing time. The data from either process can be used to estimate  $E_m^V$  from the assumed relation:

$$\frac{d(\Delta\rho)}{dt} = -F(\Delta\rho) \exp(-E_m^V/kT) \quad (4)$$



where  $t$  is the time,  $\Delta\rho$  is the quenched-in resistivity, and  $F(\Delta\rho)$  is some function whose form is determined by the details of the annealing process. In this equation it is assumed that the annealing proceeds solely by motion of single vacancies.

In the absence of detailed knowledge about the form of  $F(\Delta\rho)$ , estimates for  $E_m^V$  can be deduced from the annealing data in the following ways:

1) If one assumes a simple form for  $F(\Delta\rho)$ , Equation 4 can be integrated and the resulting equation used to analyze either isochronal or isothermal annealing data. For example, in radiation damage studies it is frequently assumed that  $F(\Delta\rho)$  has the form  $(\Delta\rho)^\gamma$ . The exponent  $\gamma$  is then the "order" of the reaction.

11) From Equation 4 we see that if we could measure  $d(\Delta\rho)/dt$  at two different temperatures  $T_1$  and  $T_2$ , under conditions where  $F(\Delta\rho)$  is the same, we could obtain the motion energy from the relation

$$E_m^V = \frac{\ln \left[ \left( \frac{d(\Delta\rho)}{dt} \right)_1 \bigg|_{(\Delta\rho_0, t_0)} \bigg/ \left( \frac{d(\Delta\rho)}{dt} \right)_2 \bigg|_{(\Delta\rho_0, t_0)} \right]}{\frac{1}{k} \left( \frac{1}{T_2} - \frac{1}{T_1} \right)} \quad (5)$$

where  $\left( \frac{d(\Delta\rho)}{dt} \right)_1 \bigg|_{(\Delta\rho_0, t_0)}$  and  $\left( \frac{d(\Delta\rho)}{dt} \right)_2 \bigg|_{(\Delta\rho_0, t_0)}$  are the



slopes of the  $T_1$  and  $T_2$  isothermal curves, both measured at the same point ( $\Delta\rho_0, t_0$ ). In practice an isothermal anneal at  $T_1$  is followed by an anneal at  $T_2$ , and the slopes of the two isothermal curves are measured at the point common to both curves (see Figure II-8). This method is known as the "change-of-slope" technique.

To analyze our data, we have used only the latter (change-of-slope) method, because it involves fewer assumptions about  $F(\Delta\rho)$ .

Since the annealing away of the quenched-in resistivity could be affected by attractive interactions (clustering) among the single vacancies, as well as the motion of defects other than single vacancies, e.g. vacancy clusters and impurities, the quantity obtained from the resistivity annealing data should be viewed as an activation energy which might, or might not, be equal to the single vacancy motion energy  $E_m^V$ .

#### D. Motivation for the Present Investigation

The measurement of quenched-in resistance is, by now, a well-established means for studying the properties of vacancies in metals. By combining such studies with measurements of vacancy concentrations at thermal equilibrium, and with studies of self-diffusion, cold work and radiation damage, a wealth of information has been obtained about the properties of vacancies and vacancy





complexes in f.c.c. metals. However, our understanding of the properties of vacancies in b.c.c. metals is much more rudimentary--in part because of the difficulty of producing high purity samples, and in part due to the difficulty of heating and quenching without contamination of the samples. Recently, quantitative quenching studies of b.c.c. transition metals have become feasible due to the commercial production of high purity samples and due to two developments in the area of producing cleaner quenching environments: 1) the development by Schultz and co-workers (15)(16) of the technique of heating and quenching fine wires while they are in the ultra-pure environment present inside of a superfluid helium bath; and 2) the commercial production of ultra-high vacuum components.

The superfluid quenching technique was recently used by R. J. Gripshover at Michigan State University (12) to do a systematic study of vacancies in quenched tungsten. Throughout these studies the purity of the samples was a point of major concern, and the possibility that Gripshover's results (e.g. see Figures II-1 and II-11) might have been due to (or affected by) impurities could not be entirely ruled out. For example, the purity of Gripshover's samples, as determined by their residual



resistance ratio ( $RRR = \text{resistance at } 273K^* / \text{vacancy-free base resistance at } 0K$ ) only modestly exceeded the minimum  $RRR$  of about 600 which he found was necessary to obtain "reproducible" data (e.g.  $RRR$  values of 650 and 750 for 1.0 mil and 1.2 mil diameter wires respectively are typical). Therefore, when we obtained a very pure 2.4 mil diameter single crystal tungsten sample from Dr. J. M. Galligan of Brookhaven National Laboratory, we decided to attempt to reproduce and extend Gripshover's results using this sample. We anticipated that with this sample we should be able to obtain better and more reproducible data than those obtained by Gripshover.

We now describe the results of our superfluid helium quenches and the subsequent annealing studies. As will be discussed later, the results of our experiments, as well as experiments carried out in other laboratories, led us to expand the scope of our investigation to include quenches in an ultra-high vacuum and field ion microscopy.

#### E. Superfluid Helium Quench Data for the 2.4 mil Diameter Sample

This sample was electropolished by Dr. Galligan down to its final size from a zone-refined single crystal

---

\*The formula  $R(273) = R^* / (1 + \alpha T)$  was used to calculate  $R(273)$  from the room temperature resistance ( $R^*$ ). Here  $\alpha$  is the temperature coefficient of resistivity ( $\alpha = 4.5 \times 10^{-3} K^{-1}$  for tungsten) and  $T$  is the difference between the room temperature and 273K.

tungsten wire. After a few initial anneals over superfluid helium its RRR was better than 5000. After performing many quenches and anneals using this sample, it became clear that it had two important advantages over Gripshover's samples: 1) The base resistivity had much less variation, thereby reducing the scatter in the data, and 2) It was not very brittle (contrary to Gripshover's samples which broke very easily in handling), thus allowing a large amount of data to be obtained on the same sample.

#### E.1) Data for Fastest Quenching Speeds

Figure II-1 shows the fast quench data for the 2.4 mil sample obtained by abruptly switching off the heating current while the sample was at the quench temperature\* and submerged in the superfluid helium. The logarithm of the quenched-in resistance  $\Delta R_q$  divided by the resistance at 273K (to remove the effect of the geometry of the wire) is plotted versus  $1/T_q$  and, as expected from Equation 1, shows a linear behavior. For comparison, Gripshover's data for a 1.0 mil and a 1.2 mil sample along with the data obtained by Schultz (19)(20) for a 1.2 mil wire (RRR  $\approx$  800) are also shown (Schultz's data had to be

---

\*The temperature of the sample was determined from the National Bureau of Standards (NBS) data for  $R(T)/R(273K)$ , where  $R$  is the resistance, versus temperature for tungsten. The NBS (17) data is somewhat in disagreement with that of Langmuir and Jones (18) used by Schultz.

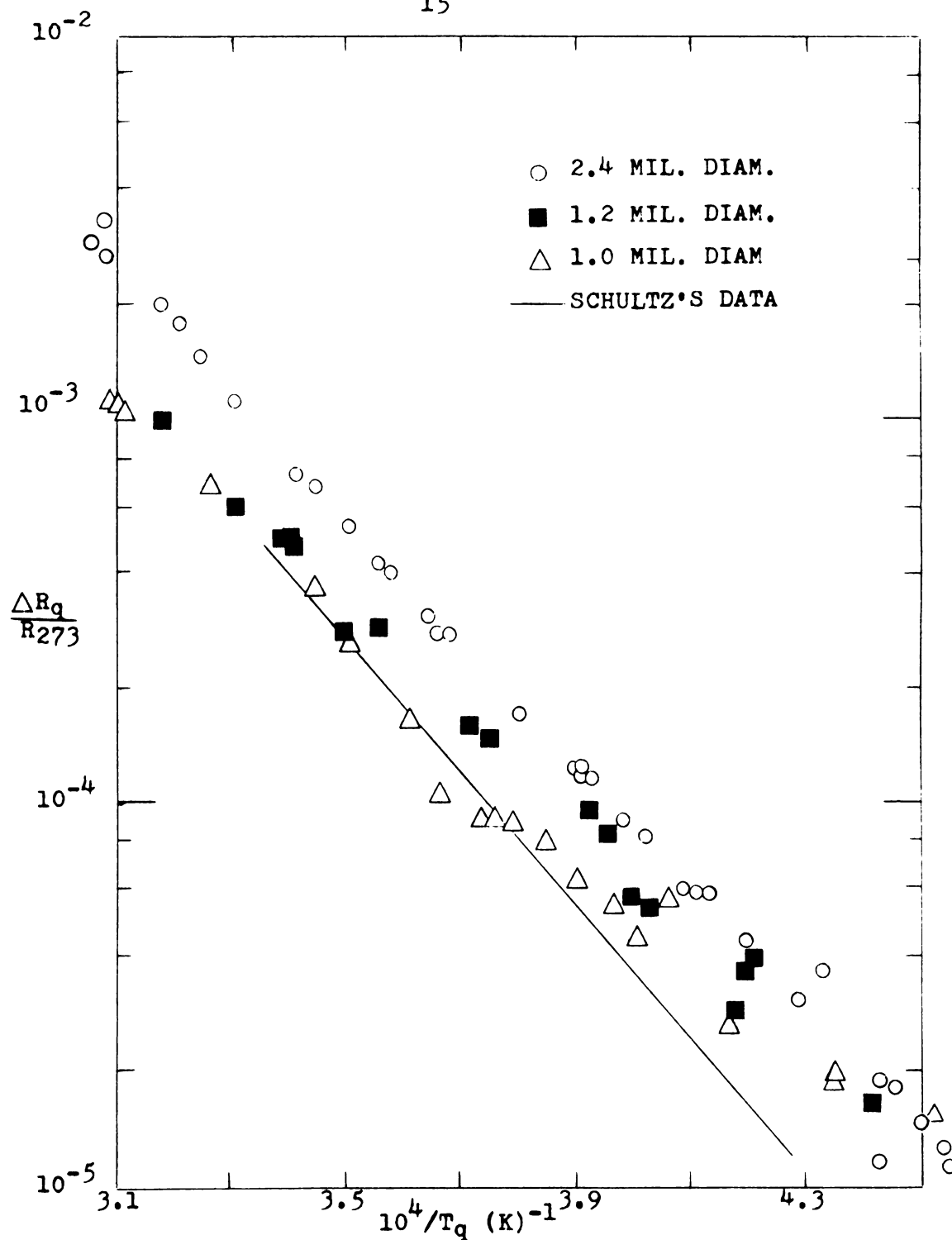


FIGURE II-1: FAST QUENCH DATA FOR THE 2.4 MIL SAMPLE. FOR COMPARISON, GRIPSHOVER'S DATA FOR A 1.0 MIL AND A 1.2 MIL SAMPLE AND SCHULTZ'S DATA FOR A 1.2 MIL SAMPLE ARE ALSO SHOWN.

converted to NBS scale of resistance versus temperature, to allow direct comparison). As can be seen, the slopes of the various sets of data are very nearly the same. However, the magnitudes of the quenched-in resistances are different for different samples. Additional experiments showed that, sometimes, there were also differences in the magnitudes of the quenched-in resistances for the same sample quenched on different days. The systematic shifts in magnitude of the quenched-in resistance were also observed by Gripshover, but they are difficult to account for. It is not clear whether they arise from deviations in the high temperature resistance of the wires from the N.B.S. values for a given temperature, or from an interaction between vacancies and impurities, leading to different quenched-in resistances from the same temperature. The variations are too large to be explained in terms of temperature nonuniformities along the sample. Further tests will be necessary to determine the source of these temperature shifts.

#### E.2) Control of the Quenching Speed

The speed of the superfluid helium quenches was controlled by connecting a capacitor in parallel with the sample, and allowing it to discharge through the sample after the power supply was disconnected. The quench speed could be conveniently varied by varying the capacitance. The quenching speed was determined from measurements of the dependence of sample resistance upon time as the sample

cooled. During the quench a small constant A.C. current (less than 1ma at 5kHz) was passed through the sample to monitor its resistance. The resulting A.C. voltage across the gauge length (the center portion of the sample between two 0.3 mil potential leads spot welded to the sample) was amplified, rectified, and displayed on an oscilloscope (see Figure II-2). The NBS values (17) for  $R(T)/R(273K)$  versus  $T$  were used to convert the oscilloscope pictures into representations of the sample temperature as a function of time during the quench.

Quenches made with large capacitors in parallel with the samples were nearly linear. For these quenches the quench speed was determined directly from the slope of the converted oscilloscope trace. Quenches made with no capacitor, or only a small capacitor, were fitted to an equation of the form:

$$T(t) = \frac{T_q}{1 + t/\tau} \quad (8)$$

This allowed the determination of  $\tau$  using all of the data on the oscilloscope picture for a given quench (see Figure II-2). The value of  $\tau$  so obtained was increased by 25% to obtain the equivalent linear quench time  $\tau_q$ . This procedure assumes the validity of the Flynn, Bass, and Lazarus (FBL) theory (21), and should be at least as reliable as, and more internally consistent than, merely estimating an equivalent linear quench time by eye. As



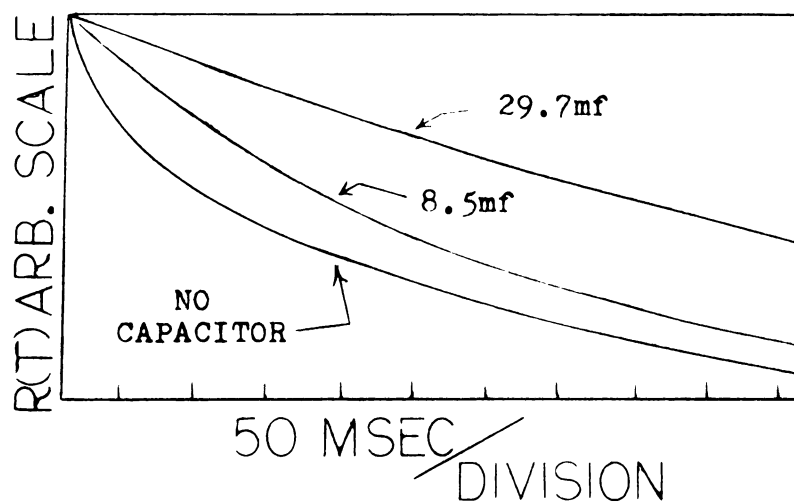


Figure II-2: QUENCH PICTURES FOR THE 2.4 MIL DIAMETER TUNGSTEN WIRE QUENCHED FROM 2800K. THE FAST QUENCH WAS MADE WITH NO PARALLEL CAPACITOR. THE SLOWER QUENCHES WERE MADE USING 8.5mf AND 29.7mf CAPACITORS RESPECTIVELY.



we will show below (see parts E.3 and E.4), the  $\tau_q$ 's obtained in this manner are used to extrapolate to infinite quench speed ( $\tau_q = 0$ ) both graphically, and by using a method prescribed by FBL.

Figure II-3 shows the dependence of the quenching rate,  $dT/dt$ , upon the quench temperature for the 2.4 mil sample. As shown, the quenching rate varied nearly linearly with the quench temperature. For very slow quenches (large capacitors) the quenching rate is independent of the quench temperature, in agreement with Gripshover's results.

#### E.3) Dependence of the Quenched-in Resistance Upon the Quenching Speed

Figure II-4 shows how the quenched-in resistance varied with quenching speed for the 2.4 mil sample, corresponding to the quenching speeds shown in Figure II-3. In order to facilitate extrapolation to infinite quench speed, we plot in Figure II-5 the logarithm of the quenched-in resistances against quench time  $\tau_q$  for two different temperatures. From Figure II-5 we can see that the equilibrium ( $\tau_q = 0$ ) concentration of vacancies at high temperatures is probably not being fully retained even with the fastest quenches. The task of extrapolating to  $\tau_q = 0$  then involves determining the curve through each set of data which correctly describes the vacancy loss. Mori, et al (22) suggested a linear extrapolation through the points obtained with the fastest quench speeds



FIGURE II-3: DEPENDENCE OF QUENCHING RATE UPON QUENCH  
TEMPERATURE FOR THE 2.4 MIL DIAMETER  
TUNGSTEN WIRE.

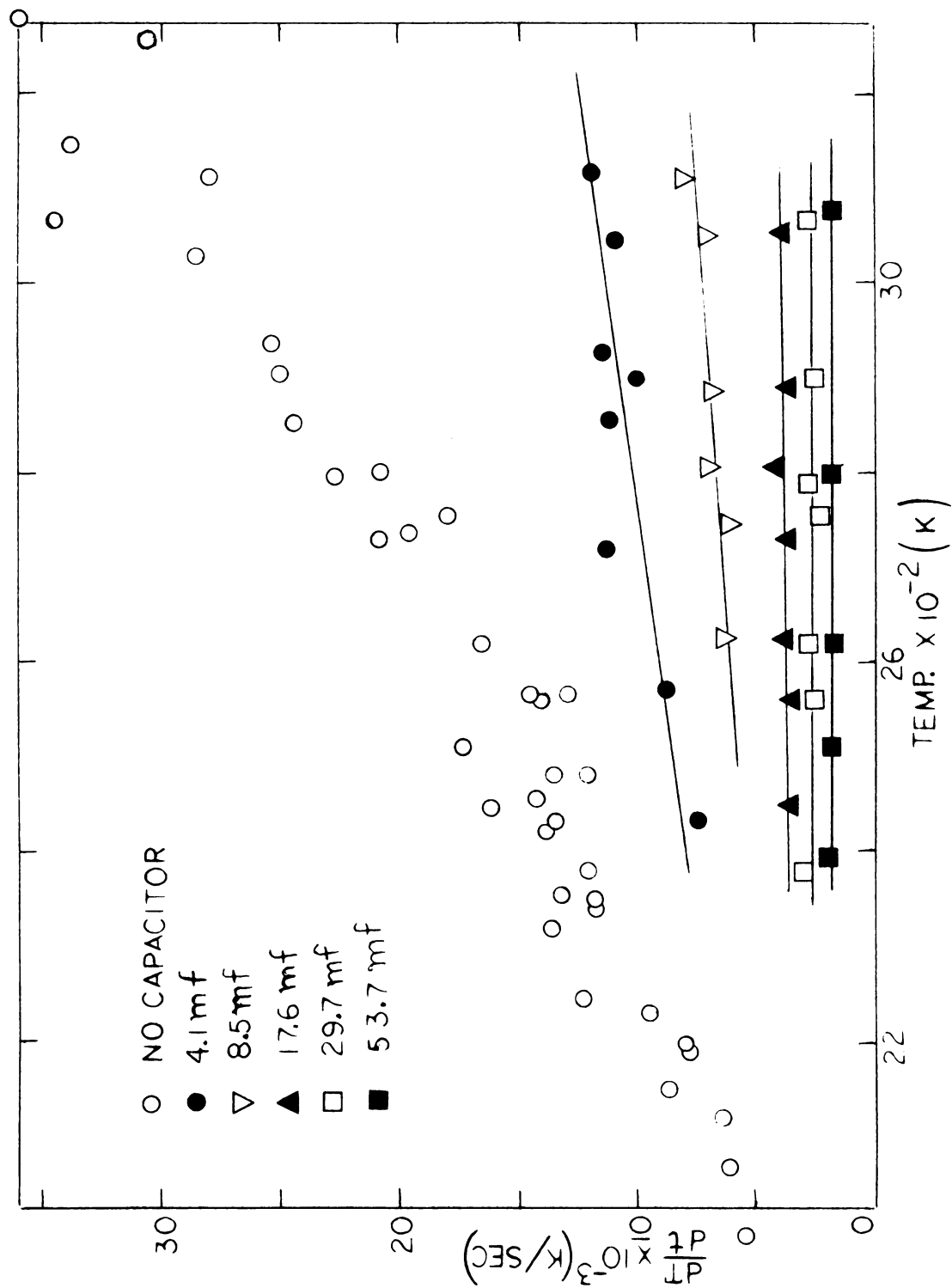


FIGURE II-3

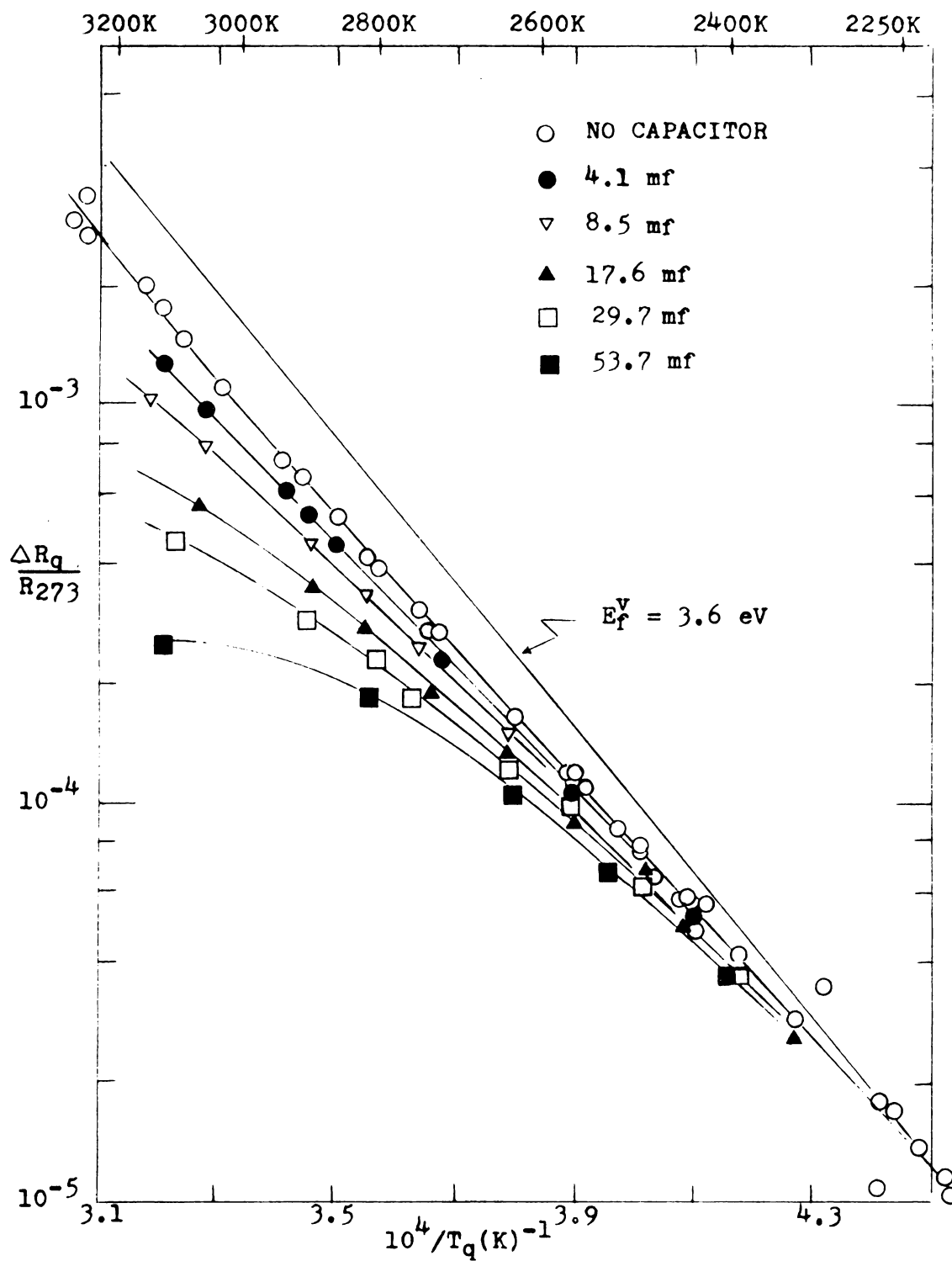


FIGURE II-4; VARIATION OF QUENCHED-IN RESISTANCE WITH QUENCHING SPEED FOR THE 2.4 MIL. DIAM. WIRE.

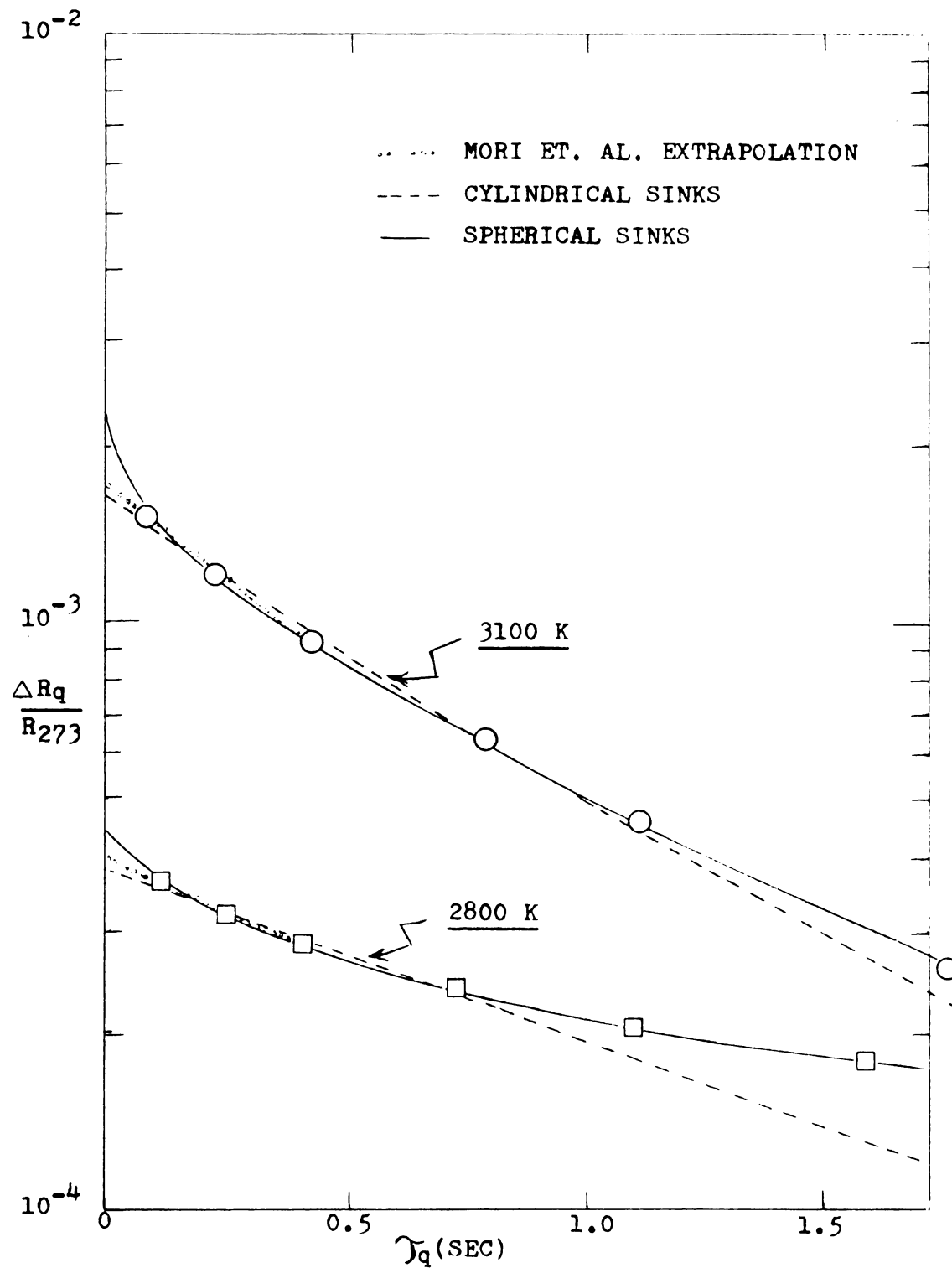


FIGURE II-5: VARIATION OF QUENCHED-IN RESISTANCE WITH QUENCH TIME FOR QUENCHES FROM 2800K AND 3100K.



(dotted lines in Figure II-5). However, FBL (21) showed that this procedure was not rigorously correct even for the simple case of single vacancies migrating to fixed sinks. They showed that the data will generally follow a curve, the nature of which depends upon the geometrical character of the dominant sinks. If the dominant sinks are dislocations, approximated as the core of a cylinder, few vacancies will initially be near the sink, and the predicted curve will be relatively flat (dashed curves in Figure II-5). However, if the sinks are grain boundaries, approximated as the surfaces of spheres, a substantial fraction of the vacancies will initially be near the surface. The predicted curve will then vary rapidly near  $T_q = 0$  (solid curves in Figure II-5). Unfortunately, we do not yet know the nature of the dominant vacancy sinks in quenched tungsten. Analysis of various possible combinations of curves similar to those shown in Figure II-5 suggests that it is unlikely that the vacancy formation energy in tungsten lies outside the range 3.4 to 4.0 eV. Since this analysis makes no a priori assumption of values for either  $E_m^v$  or  $Q$ , this conclusion does not depend upon their values.

As an alternative means of extrapolation we have also analyzed the quench data presented in Figures II-3 and II-4 according to the FBL theory as will be described below.

#### E.4) Extrapolation to Infinite Quench Speed Using FBL Theory

A theory used by Flynn, Bass, and Lazarus to determine  $E_f^V$  and  $E_m^V$  for gold (21) can also be used for other metals. This is presently the most general theory available of vacancy annealing during a quench. Analyzing the high temperature (e.g.  $1500K \leq T_q \leq 3300K$  for tungsten) quench data in terms of the FBL theory can yield information regarding the high temperature properties of vacancies. Such information can not be obtained from the annealing studies discussed in part C above, since the major annealing stage is usually at relatively low temperatures (e.g. 800-1000K for tungsten).

The two major assumptions in the FBL theory are; 1) at temperatures near the quench temperature, where this theory applies, only single vacancies are present; and 2) the sinks (e.g. grain boundaries and dislocations) for annihilation of single vacancies are fixed and temperature independent. For a linear drop in temperature during the quench, FBL proceed to show that the fraction of vacancies lost during a quench from temperature  $T_q$  depends, to a good approximation, only on the product  $D_q T_q \tau_q$ . Here  $\tau_q$  is the quench time and  $D_q$  is the vacancy diffusion coefficient at  $T_q$  given by

$$D_q = D_o^V \exp(-E_m^V/kT_q) \quad (6)$$

where  $D_0^V$  is a constant. For a given fractional vacancy loss, e.g. 50 per cent, the theory leads to the equation

$$D_q T_q \gamma_q = Z \quad (7)$$

where  $Z$  is a constant. Equations 6 and 7 suggest that a plot of  $\ln(1/T_q \gamma_q)$  versus  $1/T_q$  should be linear with slope  $-E_m^V/k$ . Determination of the point during the quench where 50% of the vacancies are lost requires a knowledge of the equilibrium vacancy concentration at the quench temperature, i.e. the "correct" value of  $E_f^V$  must be known. If such is not the case, one can choose a series of values for  $E_f^V$ , find 50% loss points corresponding to each value, and find values for  $E_m^V$  corresponding to each  $E_f^V$ . The pair  $(E_f^V, E_m^V)$  whose sum equals the value of  $Q$  (see Equation 3) is then chosen as "best" values. The details of this procedure are given below.

The analysis begins with the experimentally verifiable assertion that the smallest vacancy loss should occur for rapid quenches from low temperatures. Figure II-4 shows that, indeed, the most rapid quenches yield indistinguishable data for quenches from below 2400K. Evidently at these temperatures we can trap in essentially all of the equilibrium concentration of vacancies. Therefore, we can assume that the quenched-in resistance values for fast quenches from  $T_q \approx 2400K$  represent the resistance of the thermal equilibrium of vacancies at the quench

temperature  $T_q$ . An assumed value of  $E_f^V$  then specifies a straight line on Figure II-4 which passes through the fast quench data at low temperatures. Because of the large number of data points in the vicinity of 2250K, we have chosen this point to be on the straight lines drawn for various  $E_f^V$  values (e.g.  $E_f^V = 3.6\text{eV}$  shown in Figure II-4). For each line the data determine a series of quench temperatures  $T_q$  at which 50% of the vacancies are lost during the quench, one for each quench time  $\tau_q$ . From equations 6 and 7 above, a plot of  $\ln(1/T_q \tau_q)$  versus  $1/T_q$  using these quench temperatures should yield a straight line whose slope is  $-E_m^V/k$ . Such a plot is shown in Figure II-6 using the assumed value  $E_f^V = 3.6\text{eV}$  shown in Figure II-4. As can be seen, the data are just consistent with a straight line to within the specified uncertainties. However, the uncertainty in the data is too large to allow a definitive conclusion concerning the adequacy of the theory. For our present purposes we assume the theory to be adequate.

In this manner a value of  $E_m^V$  can be associated with each assumed value for  $E_f^V$ . The best values for  $E_m^V$  and  $E_f^V$  are chosen such that their sum is equal to  $Q$ .

Until recently, the value of  $Q$  for tungsten was in dispute. However, the latest studies of Pawel and Lundy (1) and Robinson and Sherby (2) appear to establish the value  $6.1 \pm 0.3\text{eV}$ . Using this value of  $Q = 6.1\text{eV}$  in the above analysis we determine the values  $E_f^V = 3.6 \pm 0.1\text{eV}$  and

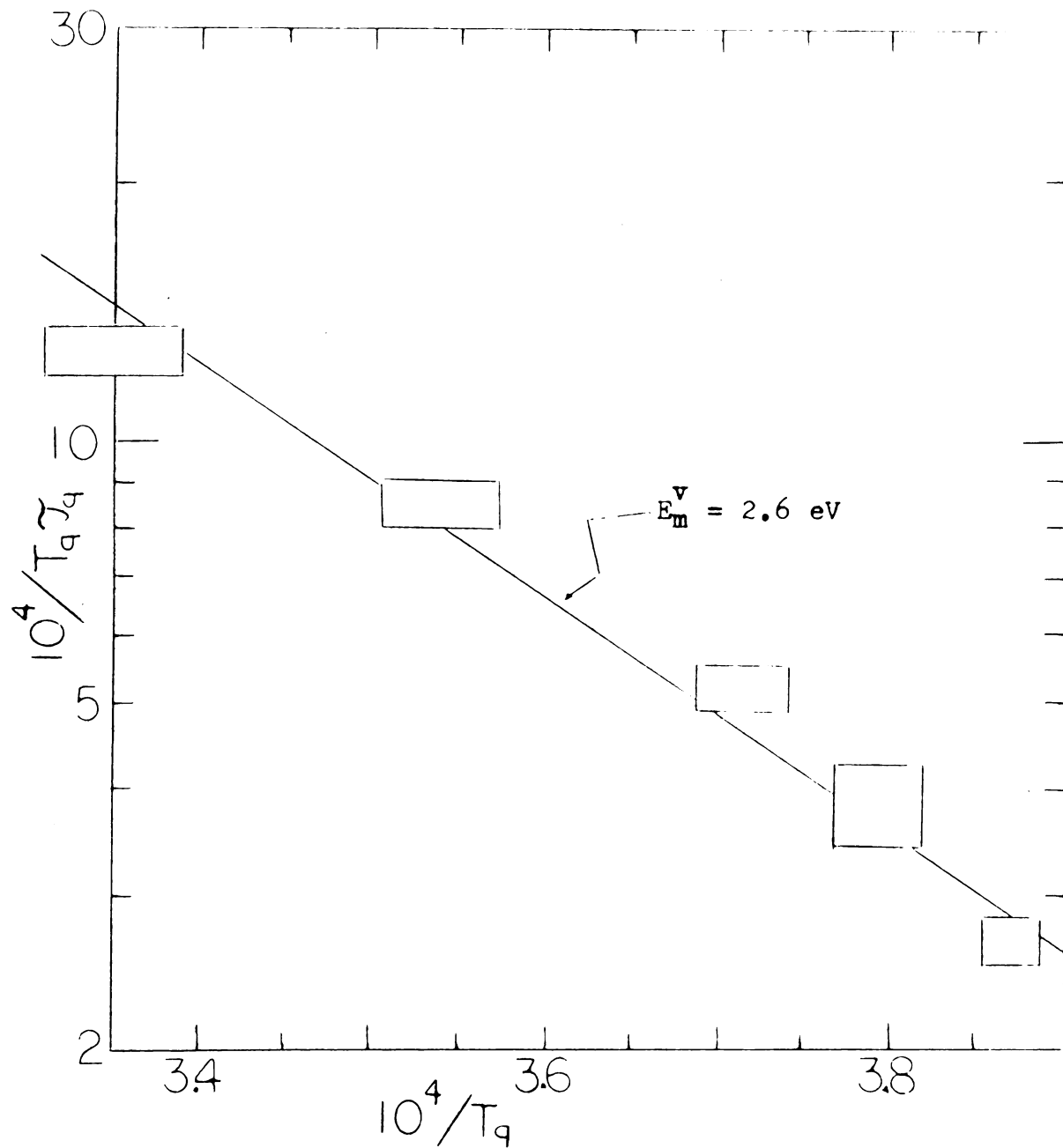


FIGURE II-6: PLOT OF  $1/T_q \tau_q$  VERSUS  $1/T_q$  FOR 50% LOSS, USING THE VALUE FOR  $E_f^v$  SHOWN IN FIGURE II-4. THE RECTANGLES REPRESENT OUR BEST ESTIMATE OF UNCERTAINTY FOR EACH POINT.

$E_m^v = 2.5 \pm 0.2\text{eV}$ , where the uncertainties shown are experimental uncertainties in determination of the various parameters. Additional uncertainty is introduced from the uncertainty in the value of  $Q$ . Taking account of this uncertainty, we arrive at  $E_f^v = 3.6 \pm 0.2\text{eV}$  and  $E_m^v = 2.5 \pm 0.5\text{eV}$  for  $Q = 6.1 \pm 0.3\text{eV}$ . These values for  $E_f^v$  fall within the range obtained with the previous graphical extrapolation procedure.

The values found by Gripshover for  $E_f^v$  and  $E_m^v$  using the above methods were  $E_f^v = 3.5 \pm 0.2\text{eV}$  and  $E_m^v = 1.4 \pm 0.2\text{eV}$ . As we will discuss later (see section G below), his interpretation of single vacancies being present during the low temperature anneals, as well as the high temperature quenches, was a direct result of his small value for  $E_m^v$ , which is considerably lower than our value. However, the source of this disagreement can be traced to the value of  $Q = 5.2\text{eV}$  used by Gripshover. Analysis of Gripshover's data for his 1.0 and 1.2 mil samples using the new value of  $Q = 6.1 \pm 0.3\text{eV}$  yields  $E_f^v = 3.8 \pm 0.4\text{eV}$  and  $E_m^v = 2.3 \pm 0.7\text{eV}$ , which are fully consistent with our results for the 2.4 mil sample. The larger ranges of uncertainties for these values, as compared to ours, are due to the larger scatter in Gripshover's data.

We conclude that the measured quenched-in resistances are consistent with the postulate that we are quenching in vacancies with a formation energy of about 3.6eV and a motion energy in the vicinity of 2.5eV. This motion

energy is smaller than the value of 3.3eV proposed by Jeannotte and Galligan (23), but reasonably close to the theoretical value of 2.8eV calculated by Flynn (24).

#### F. Annealing Data for the 2.4 mil Sample

We began our annealing studies with isochronal anneals to determine the temperature range, or ranges, in which annealing occurred. We then used the change-of-slope method to measure the activation energy for the only major annealing stage observed.

##### F.1) Isochronal Annealing Studies

After the sample was quenched from a high temperature into superfluid helium and the quenched-in resistance was measured, it was placed in a vacuum system for 10 minute annealing periods at a series of increasing temperatures. After each 10 minute anneal, a measurement of the fraction of the quenched-in resistance remaining was made at 4.2K. We have made five isochronal annealing studies on the 2.4 mil sample after it had been quenched from five different temperatures between 2946 and 3282K. In every case only a single major annealing stage was observed, centered at a temperature between 850 and 1150K. The stage was approximately 200K wide. In the absence of contamination, it contained over 80% of the quenched-in resistance. The data mentioned above is shown in Figure II-7. This figure shows a movement of the major annealing stage to higher temperatures as the magnitude

FIGURE II-7: ISOCHRONAL ANNEALS OF THE 2.4 MIL DIAMETER  
TUNGSTEN WIRE. THE SAMPLE WAS HELD FOR  
10 MINUTES AT EACH ANNEALING TEMPERATURE.



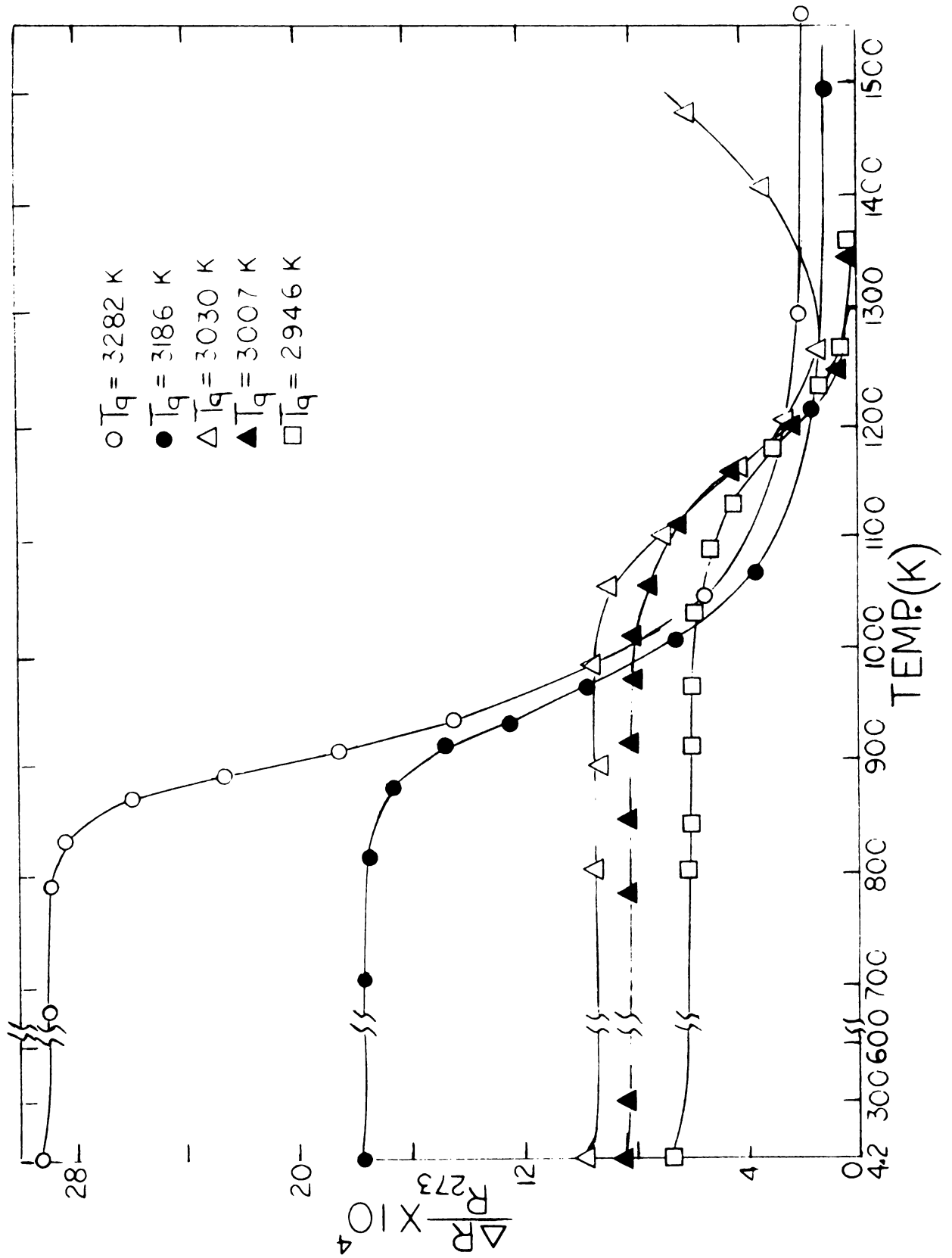


FIGURE II-7

of the initial quenched-in resistance decreases. It also shows that after quenches from below 3100K, essentially all of the quenched-in resistance anneals away in one stage. It can also be seen that for one anneal, the resistance rises at high annealing temperatures. A similar effect was observed in one other anneal of this sample and for two of Gripshover's samples. We ascribe this rise in resistance to contamination of the sample in the vacuum system ( $p \sim 10^{-6}$  torr), because any quenching of the sample subsequent to this rise produced quenched-in resistances as much as 100 times higher than had been previously obtained. Moreover, the pre-anneal base (vacancy-free) resistance and quenched-in resistances could not be restored unless the sample was annealed over the superfluid at a temperature above 3000K.

In comparing the results of our isochronal studies with those of Gripshover's, we find complete agreement of the temperature range for the recovery stage and the movement of this stage as a function of the initial quenched-in resistance. Moreover, there is agreement on the fraction ( $\approx 10\%$ ) of the initial quenched-in resistance which persists to temperatures much higher than the major recovery stage if  $T_q > 3100\text{K}$ . However, contrary to our results, Gripshover observed some quenched-in resistance remaining after the major stage even for  $T_q < 3100\text{K}$ . As we will discuss later, this information can be important in evaluating models for the formation

of vacancy complexes during the quench and the subsequent anneals.

One systematic difference between the two sets of data is the slight drop in the initial quenched-in resistance of our 2.4 mil wire (see Figure II-7), whereas Gripshover's 1.0 and 1.2 mil wires always showed an increase (of a larger magnitude). Tests showed that these effects occurred whether or not the samples were quenched, and happened even when the samples were merely taken out of the liquid helium into the room and back. This is suggestive of a surface impurity effect, but the exact reasons are not yet clear.

#### F.2) Isothermal Annealing with Change-of-Slope Measurements

Figure II-8 shows the results of the isothermal annealing studies performed on our 2.4 mil sample after it was quenched from 3255K. The annealing temperatures varied from 846 to 1040K. In order to obtain estimates for  $E_m^V$ , change-of-slope measurements were carried out with temperature changes in the range of 30 to 50K. The energy values shown at the junctions of various isothermal curves are  $E_m^V$  values calculated from the data using Equation 5. The scatter in these values is due mostly to the difficulty of measuring the correct slopes for short sections of these isothermal curves. In the example shown we follow the annealing away of the initial quenched-in resistance by nearly a factor of five (the

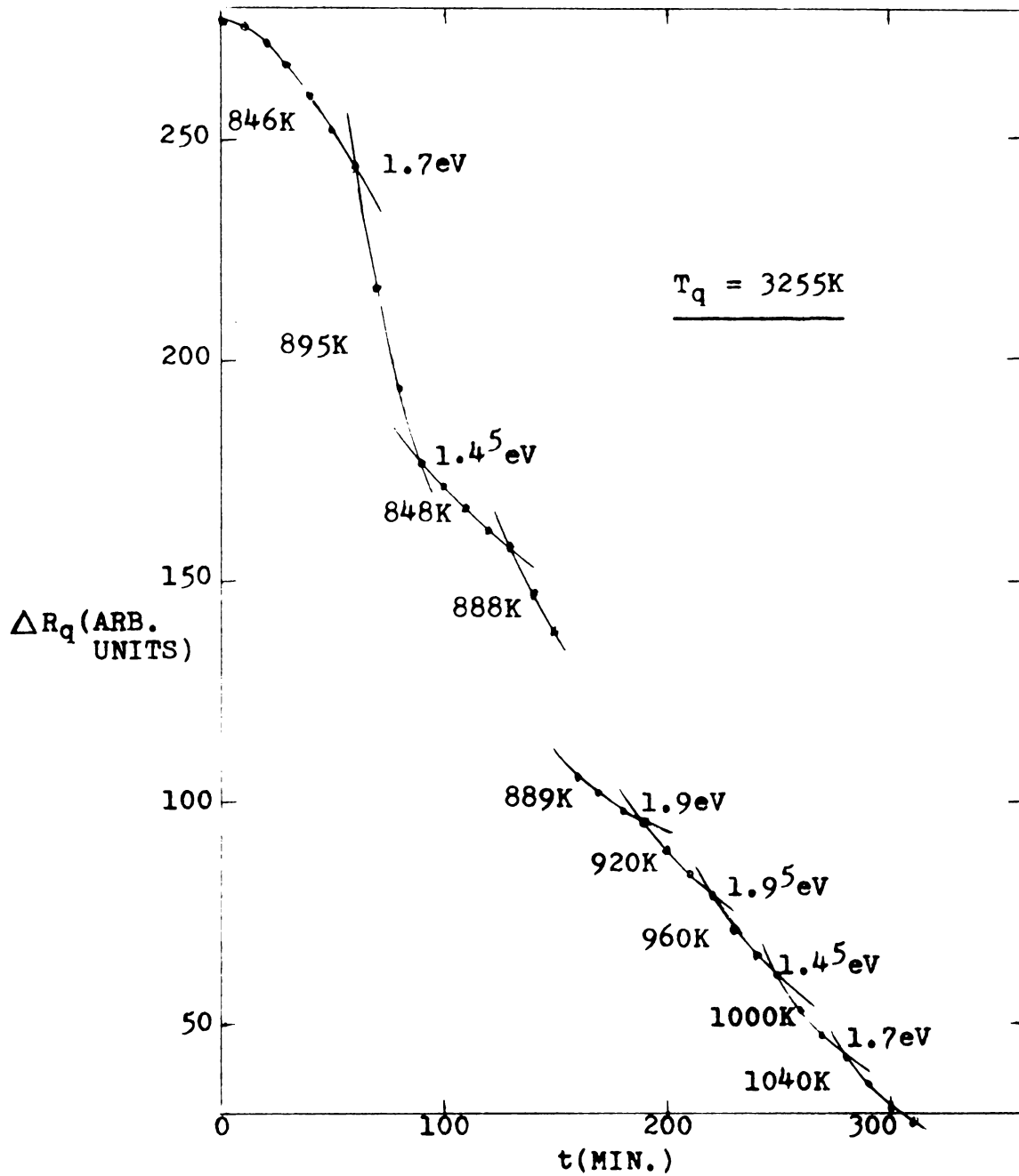


FIGURE II-8: DETERMINATION OF ACTIVATION ENERGIES FOR MIGRATION USING THE 2.4 MIL DIAMETER TUNGSTEN WIRE. THE WIRE WAS QUENCHED FROM 3255K. THE BREAK IN THE DATA ARISES FROM A LOSS OF RESISTANCE DUE TO ACCIDENTAL HEATING OF THE SAMPLE TO A HIGHER TEMPERATURE THAN PLANNED.

break in the data arises from a loss of resistance due to accidental heating of the sample to a higher temperature than planned). The changes in the annealing temperatures were made in both increasing and decreasing directions. The initial increase of annealing rate with annealing time (the "S" shape curve), as the  $E_m^V$  values, are in good agreement with Gripshover's change-of-slope studies. However, our measurements are more extensive in terms of the number of data points (see Figure II-9) as well as the range of the quenched-in resistivity remaining at the time of measurement.

Figure II-9 shows the activation energies obtained for two different quenches of our 2.4 mil sample and for two of Gripshover's 1.0 mil samples plotted against the quenched-in resistivity remaining at the time of measurement. The open symbols represent values obtained upon decreasing the annealing temperature. The filled symbols represent those obtained upon increasing the annealing temperature. These activation energies appear to cluster about the value 1.5eV, but they show no systematic dependence upon the annealing temperature, upon the magnitude of the resistance remaining, or upon whether the annealing temperature is increased or decreased. These results all suggest that we are measuring a single experimental quantity whose magnitude we deduce to be  $1.5 \pm 0.2\text{eV}$ . In view of possible temperature variation along the gauge length of the sample,

FIGURE II-9: COLLECTED ACTIVATION ENERGIES FOR LOW TEMPERATURE MIGRATION, FOR OUR 2.4 MIL SAMPLE AND FOR GRIPSHOVER'S 1.0 MIL SAMPLES ALL QUENCHED FROM ABOVE 3200K. THE OPEN SYMBOLS REPRESENT VALUES OBTAINED UPON DECREASING THE ANNEALING TEMPERATURE. THE FILLED SYMBOLS REPRESENT VALUES OBTAINED UPON INCREASING THE ANNEALING TEMPERATURE.

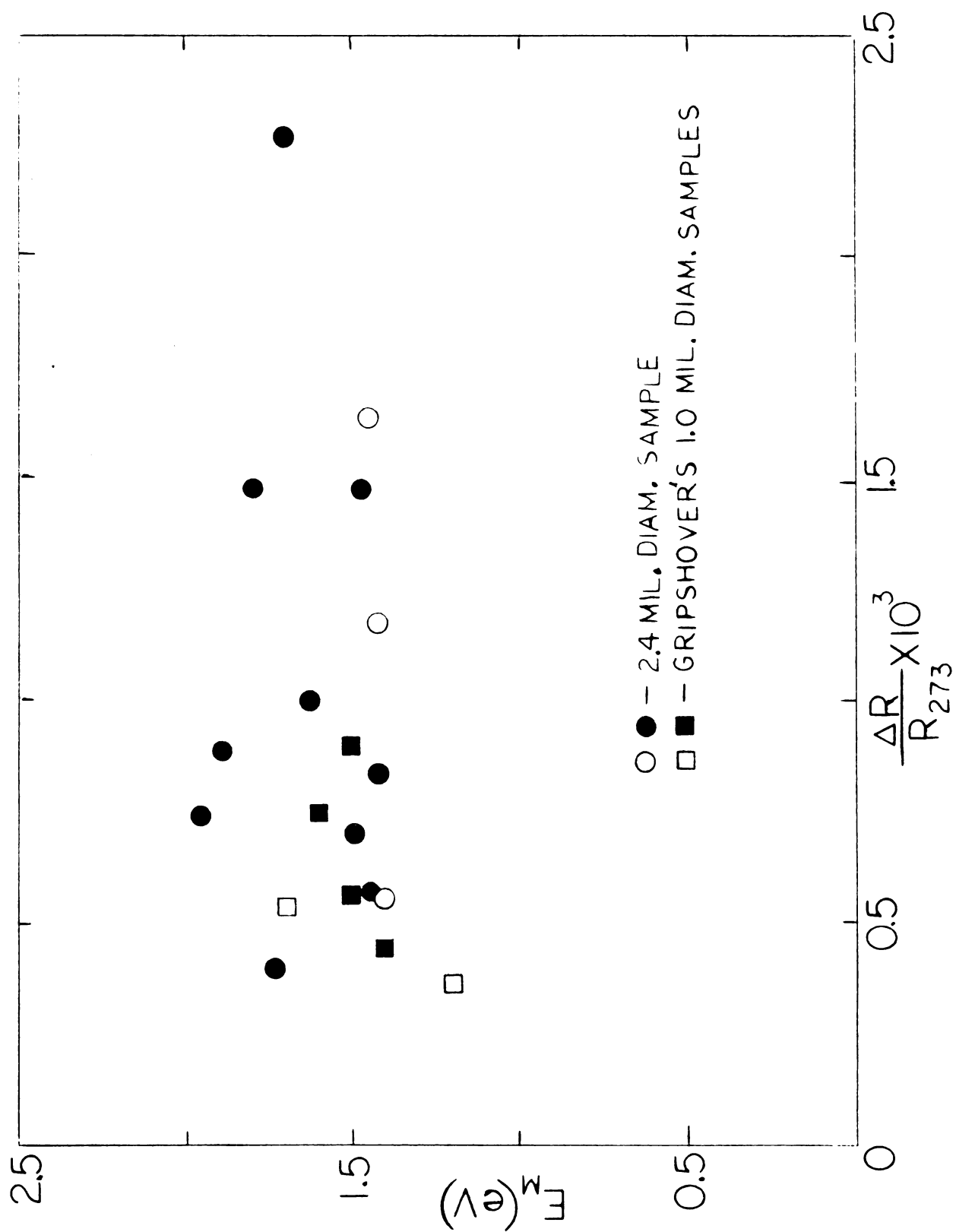


FIGURE II-9

we do not wish to over-emphasize this exact value of  $1.5 \pm 0.2\text{eV}$ . However, any bias produced by this temperature variation should be small compared to the  $1\text{eV}$  difference between this value and the  $2.5\text{eV}$  obtained from the high temperature quench data (by using FBL theory).

#### G. Interpretation of the Data in Terms of Vacancies

In Sections E and F above, we presented the data for our very pure single crystal tungsten sample, and made comparisons with Gripshover's data for his moderately pure polycrystalline samples. The agreement that we found between the two sets of experimental data indicated that a) in both cases the same experimental quantities were being measured; b) the data were relatively insensitive to differences in purity among the samples (if the minimum purity specified by Gripshover was exceeded); and c) our analysis of the data in terms of vacancies applies equally well to Gripshover's samples.

Since FBL theory assumes only single vacancies (i.e. no vacancy-vacancy interactions) at temperatures near the quench temperature, the values  $E_f^V = 3.6 \pm 0.2\text{eV}$  and  $E_m^V = 2.5 \pm 0.5\text{eV}$  found from the high temperature quench data using this theory can be treated as representing single vacancies (assuming that the theory is valid). However, the activation energy of about  $1.5\text{eV}$ , which we found from the low temperature annealing studies, suggests that the single vacancy assumption can not be extended



to temperatures much below the quench temperature.\* As we will see below, it is possible to interpret our data in terms of interacting vacancies.

If an f.c.c. metal such as gold is quenched from near its melting point, the activation energy determined from low temperature annealing studies is also smaller than  $E_m^V$  (25)(26)(27) (further similarities between the results obtained from resistivity measurements on gold and tungsten are shown in Table II-1). The standard explanation for this fact is that the low temperature annealing proceeds via the motion of small, highly mobile vacancy clusters (e.g. di- and tri-vacancies) which are formed during the quench. This interpretation presupposes an attractive interaction between vacancies.

It is also possible to interpret our data in terms of interacting vacancies. An attractive interaction is assumed to produce small, highly mobile vacancy clusters during the quench. The migration energy of 1.5eV is associated with these small clusters. The attractive interaction between vacancies also leads to the formation of large, stable clusters during subsequent annealing. These clusters provide the quenched-in resistance remaining at the end of isochronal anneals performed after

---

\*Gripshover's single vacancy interpretation was prompted by the agreement between the low temperature activation energy of  $\approx 1.5\text{eV}$  (see Figure II-9) and his high temperature value of  $E_m^V \approx 1.5\text{eV}$  (see page 28).

TABLE II-1  
COMPARISON OF SELF DIFFUSION, QUENCHING, AND ANNEALING  
DATA FOR GOLD AND TUNGSTEN

	GOLD	TUNGSTEN
$T_m$ = melting temperature	1336K	3683K
$Q/kT_m$	16	19
$E_f^V/Q$	0.5	0.6
$E_m^V/Q$	0.5	0.4
Major isochronal annealing stage(s) (after a quench from near $T_m$ )	A single stage at $\sim T_m/4$	A single stage at $\sim T_m/4$
Resistance remaining after the major isochronal annealing stage (see Figure II-7)	About 10% of the initial quenched-in resistance	About 10% of the initial quenched-in resistance
Initial shape of the isothermal annealing curves (see Figure II-8)	"S" shape	"S" shape
Activation energy obtained from isothermal anneals with change-of-slope (after a quench from near $T_m$ ) (see Figures II-8 and II-9)	About 70% of $E_m^V$	About 70% of $E_m^V$

high temperature quenches (see Figure II-7). The formation of these clusters is also the source of the initial increase in the rate of resistance loss with increasing time which occurs during isothermal anneals (see Figure II-8). As new clusters form, the number of sinks for vacancies increases, leading to a more rapid loss of vacancies. When the limiting number of clusters is reached, the remaining vacancies anneal to a set of fixed sinks, and the annealing rate decreases with increasing time.

This interpretation is, of course, tentative. Further quenching studies involving both measurements of electrical resistance and observations using electron and field-ion microscopes will be necessary to establish whether it is correct.

We conclude by noting that this interpretation is not inconsistent with the field-ion microscope study of vacancies made by Jeannotte and Galligan (23) after radiation damage; they observed mostly single vacancies, for which they estimated  $E_m^V \approx 3.3\text{eV}$ . They estimated that the vacancies in their sample made  $10^4$  jumps before being annihilated. This is only about the number of jumps necessary to bring two vacancies together. Thus, during the anneal an average vacancy will not meet another vacancy prior to annihilation. The radiation damage experiment does not provide any means by which a substantial fraction of the vacancies may cluster prior to the

anneal. Therefore, to make the two sets of results mutually consistent, we need only require that the two estimates for  $E_m^V$  (3.3eV and 2.5eV) have enough uncertainty to allow for overlap. This is, in fact, true.

#### H. The Effect of Contaminants on the Resistivity Data

After the experiments described in Sections E and F were completed and the data analyzed in terms of vacancies, we turned our attention to the possibility that the quenched-in resistivities may have been due to interstitial atoms of carbon or gas retained in solution during the quench. We decided to examine various impurities which were likely to be present during the superfluid quenches, and as a long-range project, do a study of vacancies by direct observation in a FIM.

Taking the largest quenched-in resistance as a measure of the equilibrium fractional carbon concentration  $c$ , we find  $c \approx 10^{-4}$  carbon atoms/tungsten atom. Such a small carbon concentration should be soluble in tungsten at temperatures above about 1800K (28). We assume that during a quench this equilibrium concentration is maintained until about 1800K, after which precipitation begins. The amount of precipitation should then depend primarily upon the rate of cooling of the sample at temperatures in the vicinity of 1800K. From Figure II-2 we see that the cooling rates obtained using large capacitors are very nearly constant during the quench (i.e., the quenches are

nearly linear with time). From Figure II-3 we see that these cooling rates are also nearly independent of quench temperature. Thus, when a large capacitor is used, the above model requires the quenched-in resistance to be nearly independent of the quench temperature. Figure II-4 shows that, on the contrary, the quenched-in resistances obtained with the two largest capacitors decrease by factors of 6 and 10 respectively as the quench temperature drops from 3100 to 2400K. A slightly stronger version of the same argument can be made using the resistance quenched in from 2400K with no capacitor. This resistance is 5 times smaller than that quenched in from 3100K using the largest capacitor. But the cooling rate at 1800K is greater for the low temperature quench with no capacitor than for the high temperature quench with the largest capacitor. Clearly the data of Figure II-4 are not consistent with this simple model of carbon precipitation during the quench.

We next consider whether the data could represent gas atoms trapped in interstitial solution during the quench.

The prime candidate, helium, will be considered in Sections J and L below. The vapor pressures of gases which are soluble in tungsten (e.g. O, N, CO, H) are all negligibly small at 1.3K. Thus the only sources of gaseous impurities would appear to be: a) solid contaminants in the liquid helium and b) the sample surface.

(a) It is known that some nitrogen and oxygen can be retained in colloidal solution in liquid helium (29). We therefore tested to see whether contamination of the superfluid with air would produce changes in the quenched-in resistance. Admission of a quantity of air sufficient to produce a large amount of snow on the Dewar bottom failed to produce any change in the quenched-in resistances from those obtained with clean helium. (b) In our thin wires each monolayer of surface atoms corresponds to approximately  $10^{-5}$  volume atoms. Thus a few monolayers could account for the observed quenched-in resistances. However, it seems difficult to believe that a substantial fraction of these surface atoms would be present at thermal equilibrium in a hot tungsten wire. There is, after all, no means for replacing gas atoms which come to the sample surface and boil off. Rather, one would expect extended high temperature annealing to purify the sample. Indeed, this is presumably one reason for the decrease, upon extended annealing, of the residual resistivity of a freshly prepared wire. We conclude that it is unlikely that our data are produced by a contaminant gas. Rather, on the basis of our data, and the arguments presented in Sections E, F, and G above, we are led to ascribe the quenched-in resistances in our sample (and Gripshover's samples) to vacancies trapped in the wire by the rapid quench.

## J. Need for Further Experiments

Our assertion\* that the resistance quenched into our tungsten sample (and Gripshover's samples) was due to vacancies was later challenged on the basis of measurements made on the metal molybdenum (3)(4), for which quenches in ultra-high vacuum, and from high vacuum into a liquid metal did not yield any quenched-in resistance, and no vacancy loops were observed under an electron microscope. Since Mo is also a b.c.c. refractory metal, and its physical and chemical properties are very similar to those for W, it was argued that we must be observing not vacancies, but rather some impurity retained in solution during the quench. Recently, Lidiard (5) argued that helium atoms can become trapped inside of vacancies and stabilize vacancy clusters. This could imply that helium atoms, which are believed to be insoluble in metals (6), may enter the lattice through the vacancies, and stabilize the vacancies during a superfluid helium quench, resulting in a larger quenched-in resistance than would be obtained for a quench in vacuum. This argument became more plausible when Kimura (7) quenched Mo in superfluid helium and was able to obtain quenched-in resistances for samples which exceeded a

---

\*This assertion was first made by Schultz (20), and more recently reiterated by Kunz and Schultz (30).

minimum level of purity.

These results lend themselves to at least four alternative interpretations:

1) The experiments using superfluid helium involve no vacancies, but rather an unknown contaminant which produces the quenched-in resistance--this is Evan's interpretation (8). Since the impurity is not identified, we consider two most general cases:

- (a) The impurity is external to the sample, i.e. enters the sample from the superfluid helium.
- (b) The impurity is internal to the samples, i.e. the superfluid bath is unimportant.

In each case we shall also consider the two possibilities that the impurity may enter the lattice substitutionally or interstitially (this will be of importance in FIM observation of the samples).

2) Helium atoms diffuse into the metal by becoming trapped in the vacancies, thereby stabilizing the vacancies during a superfluid helium quench.

3) An interstitial impurity other than helium (e.g. carbon) enters the vacancies and stabilizes them during a quench. This is an analogous case to alternative #2 which we are considering.

4) The resistivity quenched into the sufficiently pure W and Mo samples quenched in superfluid helium is due to vacancies alone. In this case the experiments with Mo quenched in vacuum and a liquid metal (3)(4) must have



involved either insufficiently pure samples, or contamination of the samples while they were in the vacuum system.

We therefore reoriented our research program to produce a decision in favor of one of these four alternatives.\*

As we discussed earlier (see Section H), our data were not consistent with a simple picture of carbon being retained in solution during the quench. Moreover, admitting large amounts of snow in the superfluid helium did not produce a change in our data. This information is qualitatively useful, but it does not conclusively rule out alternative #1.

After a preliminary examination of the above four alternatives, we concluded that in addition to superfluid quenching and FIM studies, other types of measurements (e.g. vacuum quenching studies) would be required to clearly determine the correct alternative by a process of elimination (see Section L below). Our FIM project was then expanded to construction of a dual system, useful both as a FIM and as an ultra-high vacuum quenching unit.

We will defer the detailed discussion of the

---

\*Since our future plans are for quantitative FIM studies of vacancies in quenched tungsten, it is very important to know beforehand which of the above alternatives is correct.



alternatives mentioned above until the results of our ultra-high vacuum quenches have been presented.

#### K. Comparison of Ultra-high Vacuum and Superfluid Helium Quenches

The sample holders used for our previous measurements in superfluid helium contained materials which could not be baked out in a vacuum system. Therefore, upon the completion of our ultra-high vacuum system, we designed new sample holders for ultra-high vacuum quenches which were adaptable to our old holders for performing superfluid helium quenches.

The schematic diagram of one of the sample holders is shown in Figure II-10. Three aluminum blocks mounted on two 1/16 inch diameter alumina tubes form the frame of the sample holder. The center block has an aluminum plate bolted on it which presses two 10 mil diameter platinum wires between two sheets of mica. One end of these wires is spotwelded to 0.3 mil tungsten potential leads which are then spotwelded to the specimen. The other end is tied around the alumina tubes and is then spotwelded to 1/16 inch diameter tungsten rods used to plug into female ultra-high vacuum connectors. The side aluminum blocks have a 10 mil platinum wire bolted to one face which passes through a small hole in the block, is bent around, and is spotwelded to the specimen. The 16 mil gold wires attached to the blocks connect the blocks to a current source. The two alumina tubes



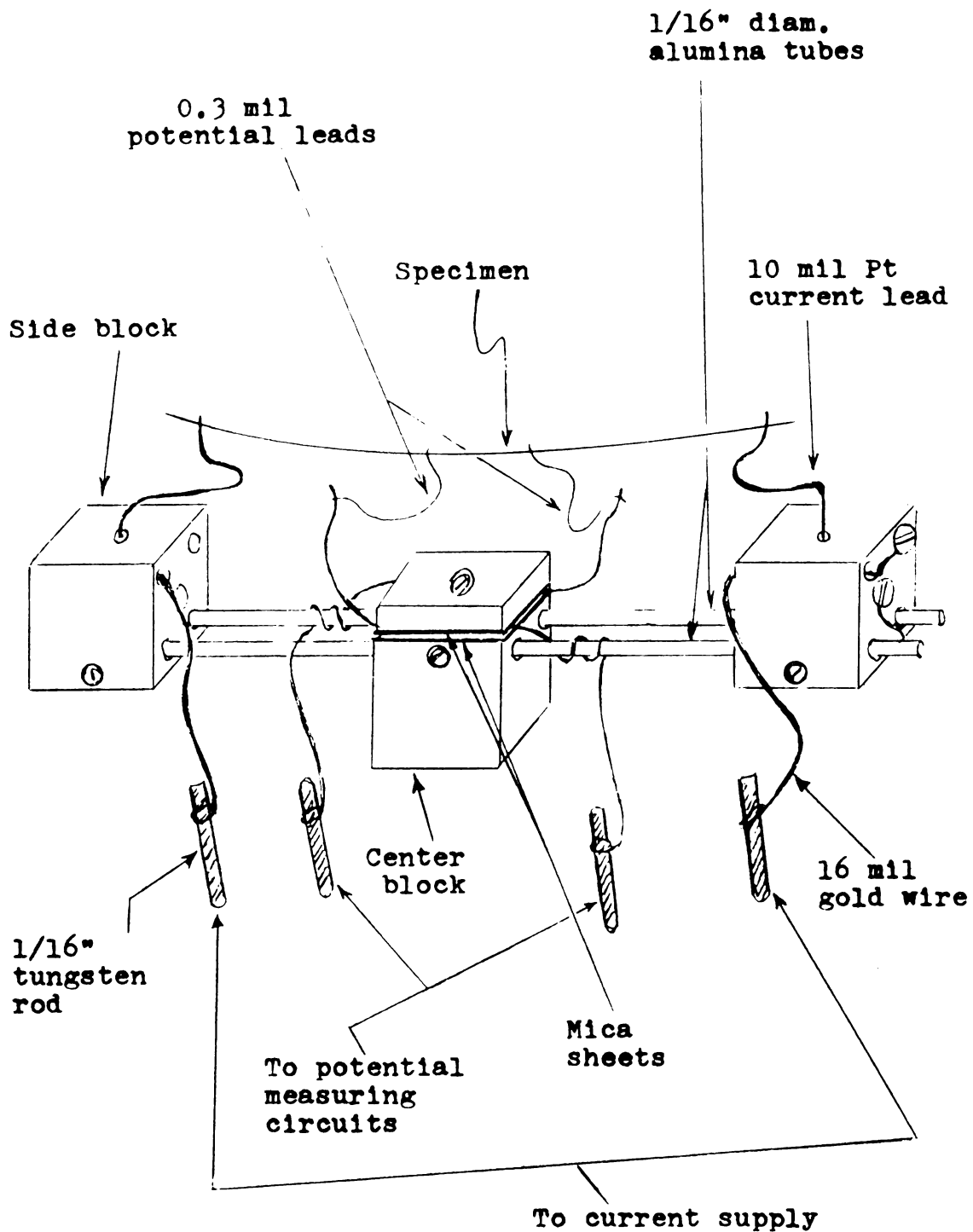


FIGURE II-10: SAMPLE HOLDER FOR ULTRA-HIGH VACUUM AND SUPERFLUID HELIUM QUENCHES.

support the holder and provide electrical insulation between the side blocks and the potential leads. The blocks are held on these tubes with set screws.

When a current is passed through the sample, the voltage across the potential leads is measured and is divided by the current (which is measured by the voltage drop across a standard resistor in series with the sample) to yield the resistance across the gauge length.

To date, we have quenched 5 different tungsten wires (three 1.0 mil and two 1.2 mil diameter)\* in pressures of about  $1.2 \times 10^{-9}$  torr in the vacuum system. The data are shown in Figure II-11 (vacuum quenches are open symbols). For comparison, we have also shown the fast quench data for our 2.4 mil sample\*\* and a typical line through Gripshover's data (also see Figure II-1). The data for the vacuum quenches are clearly consistent with the superfluid quench data.

To make the argument stronger, we quenched two samples (diameters 1.0 and 1.2 mil) in superfluid helium after they had been quenched at least twice in vacuum (the superfluid quenches are shown as solid symbols in

---

\*These samples came from the same rolls used by Gripshover.

\*\*During the last part of our superfluid helium quenching studies, the 2.4 mil sample unfortunately burned out when we were trying to see the effect of allowing air in the Dewar when the sample was hot and above the surface of superfluid. Since then, we have not been able to reproduce either its base (vacancy-free) resistance or its quenched-in resistances.

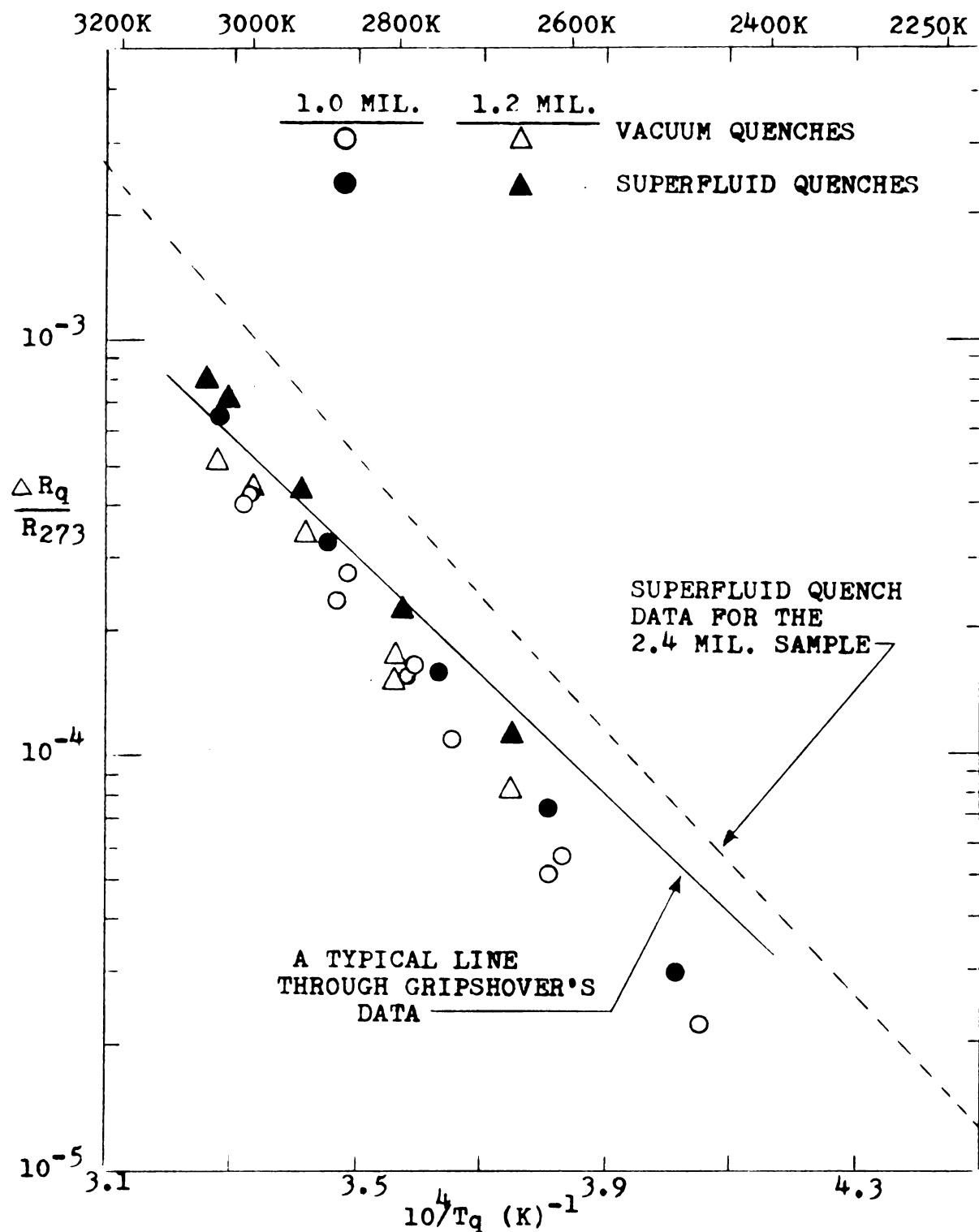


FIGURE II-11: ULTRA-HIGH VACUUM (OPEN SYMBOLS) AND SUPERFLUID (FILLED SYMBOLS) FAST QUENCH DATA FOR A NUMBER OF 1.0 AND 1.2 MIL. DIAMETER TUNGSTEN WIRES.





Figure II-11). We then quenched the same samples in vacuum at least two more times. As can be seen, these data points are indistinguishable from those obtained for samples that were only quenched in vacuum. The slightly lower quenched-in resistances in vacuum are presumably due to the slower quenching speeds at lower temperatures in the vacuum system.

From the above results we conclude that first, the quenched-in resistances in superfluid helium quenches are not due to external impurities entering the sample during the quench, and second, helium atoms do not enter the lattice through vacancies, i.e. alternatives #1(a) and #2 in part J above are invalidated.

#### L. Conclusions

We now return to the alternative interpretations presented in Section J. With the simplification introduced by the vacuum quenching results, we have the following:

- 1) The quenched-in resistances measured in tungsten are produced by internal impurities which can be either interstitial (i), or substitutional (s).
- 3) An interstitial impurity (e.g. carbon) enters the vacancies and stabilizes them during the quench.
- 4) The resistivity quenched into the sufficiently pure W and Mo samples quenched in superfluid helium is due to vacancies alone.



These alternatives can now be further analyzed by FIM studies such as those shown in Figure II-12 where the final conclusions of two FIM studies, depending on the outcome of these studies, are shown inside of circles. As can be seen, a FIM study of a sample fabricated from a thoroughly annealed (i.e. zero quenched-in resistivity) wire can test the validity of alternative #1(s). Similarly, the study of a second sample which is fabricated from the same wire (after it has been quenched in vacuum or superfluid helium from near its melting temperature) can test the validity of #1(1). If it should turn out that #1(s) and #1(1) are invalid (which, from our results given in Sections G and H above, we suspect will be the case), the remaining two alternatives (#3 and #4) will have to be examined by means other than field ion microscopy. The reason is that any interstitial impurity trapped inside of a vacancy will be ionized away instantly as the crystal plane containing the vacancy becomes exposed during field evaporation, i.e. in a FIM an empty vacancy can not be distinguished from one occupied by an interstitial impurity. However, it is important to note that alternatives #3 and #4 both require the existence of vacancies. Below, we will discuss how the correct choice from these two alternatives may be experimentally identified.

As we mentioned above, we find that the analysis of our resistivity data suggests that alternatives #3 and #4



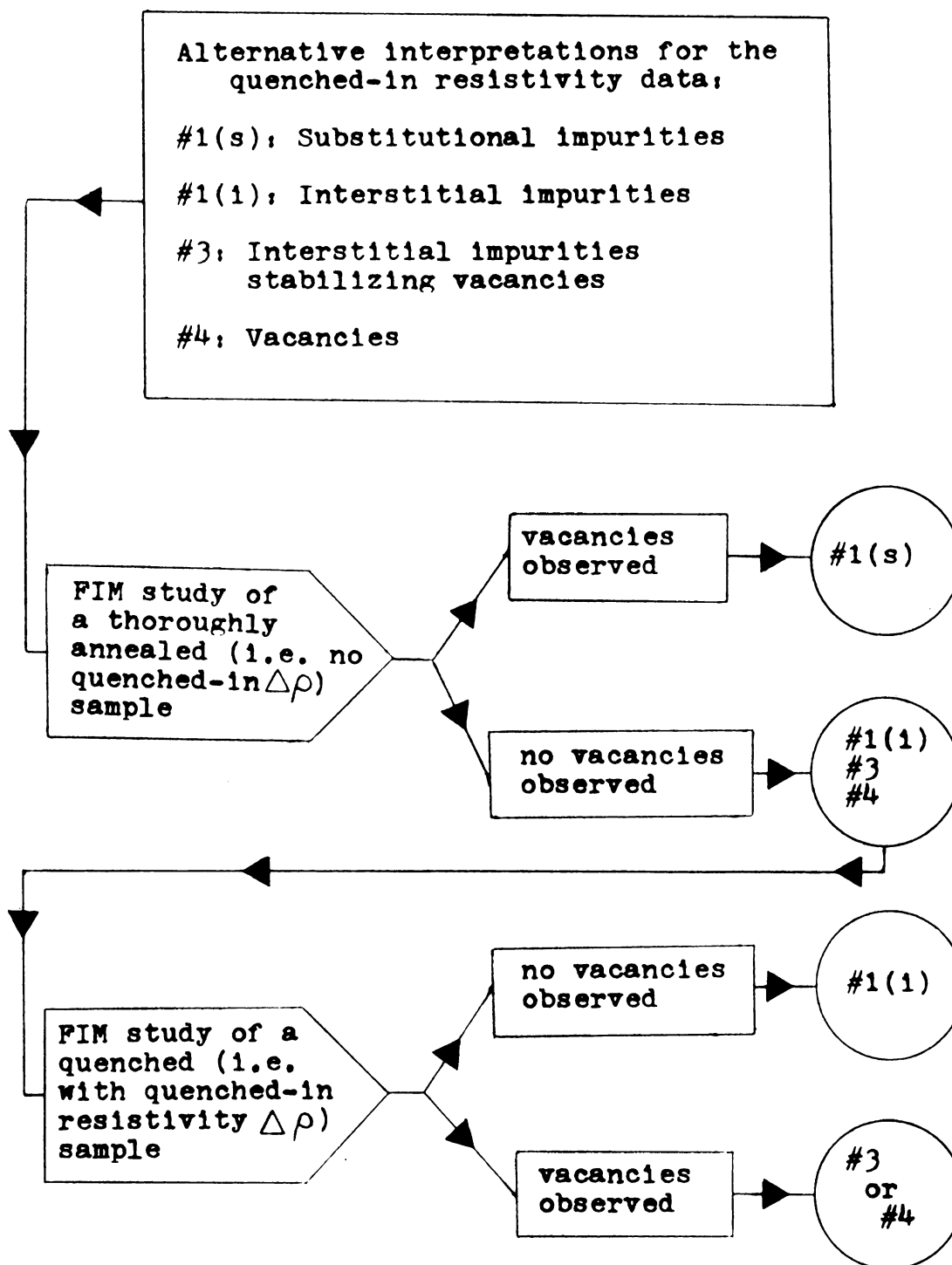
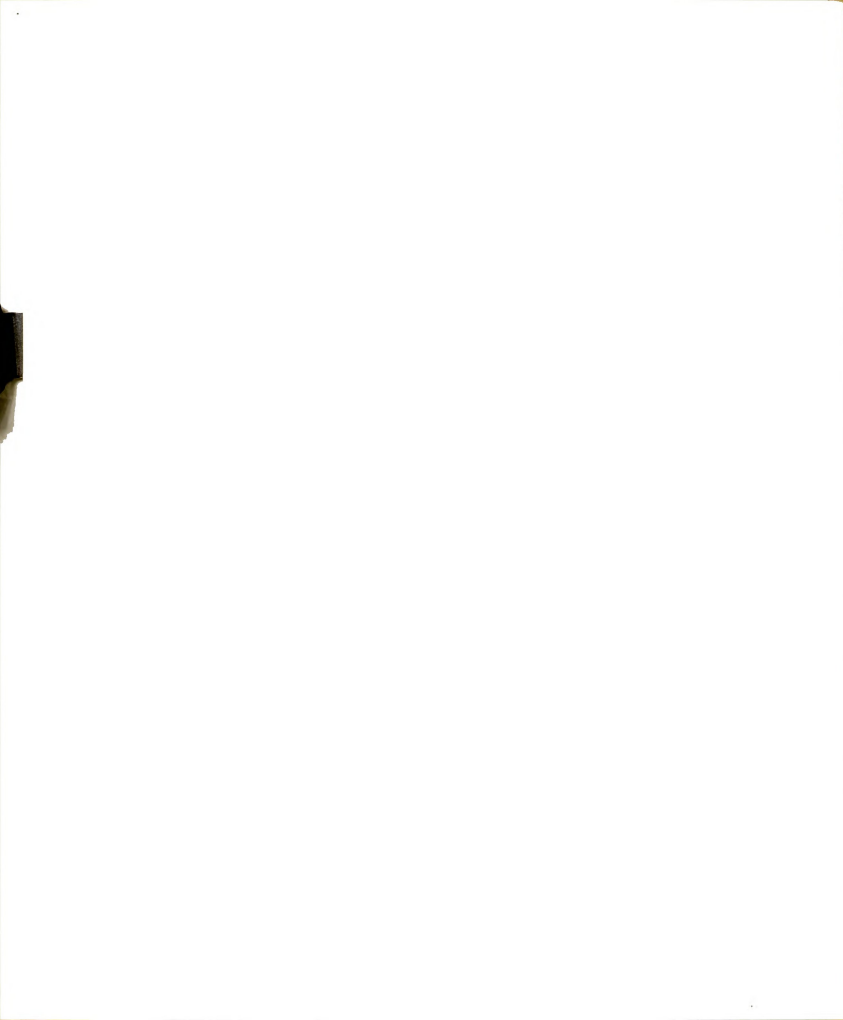


FIGURE II-12: PROPOSED SCHEME FOR PERFORMING TWO SETS OF FIM STUDIES TO ANALYZE VARIOUS INTERPRETATIONS FOR THE QUENCHED-IN RESISTIVITY DATA.



which are both associated with vacancies are more likely to explain our data than alternatives #1(s) and #1(1). However, if alternative #3 is correct, the values that we found for formation and motion energies of vacancies will represent the interstitial impurities that are trapped in the vacancies as well as the vacancies themselves. At this point we find it necessary to investigate the nature of the interstitial impurities which might be responsible for stabilizing the vacancies during the quench.

With the purity of our samples ( $RRR \approx 10^3 \Rightarrow$  approximate concentration of impurities  $\sim 10^{-5}$ ) and the extent of high temperature anneals ( $T \gg 3000K$ ) to which they are subjected, carbon is the most likely candidate to be the dominant interstitial impurity remaining.\* However, we have the following reasons to believe that carbon (or any other interstitial impurity) is not responsible for the observed quenched-in resistances:

- a) If interstitial impurities stabilize vacancies, samples of higher purity should show smaller quenched-in resistances. Figure II-1 shows the opposite

---

\*Carbon is the only material which has a higher melting temperature than tungsten. Other interstitial solutes (e.g. O, N) form compounds with tungsten which are more volatile than tungsten, therefore, they are expected to boil off during high temperature anneals performed in a pure atmosphere.





effect where the pure 2.4 mil diameter sample showed higher quenched-in resistances than Gripshover's less pure samples.

- b) Gripshover annealed many of his 1.0 and 1.2 mil Westinghouse samples in a hydrogen atmosphere, which is believed to purify and decarburize metals. He noted some increase in purity (higher RRR's), but no difference in the quenched-in resistance values.
- c) As we noted in Section H above, from what is known about properties of carbon in tungsten, our data is not consistent with a simple model of carbon producing the quenched-in resistivities. These reasons are, of course, not conclusive enough to warrant rejection of alternative #3 in favor of #4. Further experiments must be carried out to observe the effects on the quenched-in resistance values due to addition of small amounts of various impurities (e.g. carbon) to extremely pure samples. As will be described below, we are presently involved in the preparation of such pure samples.

In the absence of any results for the experiments suggested above, we shall reiterate our previous assertion that our data appear to be most consistent with an interpretation involving vacancies alone (i.e. alternative #4).



### M. Present State of our FIM Studies

As we will describe in Chapters III and IV, the FIM system is presently operational. However, the fractional concentration of vacancies in tungsten is estimated to be only about  $10^{-4}$  (19) at melting point. Therefore, for any meaningful quantitative studies, it is imperative that the concentration of substitutional impurities be considerably lower than  $10^{-4}$ . At present the major obstacle in performing our FIM studies is lack of sufficiently pure samples of the proper diameter. However, we have made reasonable progress in producing our own zone-refined single crystal tungsten rods, as we will discuss below:

We have recently renovated a Materials Research Corporation ultra-high vacuum electron beam zone-refiner for growing high purity single crystal tungsten samples. The vacuum system of this zone refiner was initially highly contaminated (initial ultimate vacuum  $\sim 10^{-6}$  torr) but now can reach a vacuum of  $\approx 2 \times 10^{-8}$  torr, and remains below  $10^{-7}$  torr during the zone refining. Unfortunately, after repeated failures, it became clear that the design of the zone-refining mechanism of this machine also left much to be desired (this model MRC zone refiner is presently obsolete). Within a period of over a year we gradually discovered the various sources of difficulty with this mechanism, and replaced many of its parts with those of our own design. These renovations allowed a



smooth motion and a constant power output for the zone heating unit, but the width of the melted zone was too large to allow zone refining rods of diameters smaller than 1/8 inch. Recently we have added a focusing unit so that the electron beam is focused over a smaller zone, which allows zone refining of rods which are 1/16 inch or less in diameter. To date, several single crystal tungsten rods of  $RRR \geq 40000$  have been produced, but their diameters (1/8 inch and 1/16 inch) are unfortunately too large for use as either quenching or FIM samples. We are presently developing etching and electropolishing techniques to reduce the size of these rods to fine wires of only a few mils diameter, and yet maintain a uniform cross section along the wires.



### III. DESCRIPTION OF THE ULTRA-HIGH VACUUM SYSTEM

#### A. Introduction

This vacuum system is an all-metal bakeable unit designed to lower the pressure in the main vacuum chamber to  $10^{-9}$  -  $10^{-10}$  torr in less than a day of pumping after a few hours of bakeout. Careful measures have been taken to ensure that the vacuum chamber remains free from contaminants and that every source of oil in the pumping line is properly trapped.

For economic reasons it was decided to combine the integral parts of a vacuum quenching unit and a FIM into one system. The FIM body was constructed on a 10" diameter ultra-high vacuum flange, and the vacuum chamber was designed to be large enough to accomodate this FIM (see section IV-C) through its top port. When the FIM is removed and replaced by a 10 inch blank-off flange, the entire volume (about 15 liters) of the chamber is free for vacuum quenching or other purposes.

We have fully verified the satisfactory operation of this vacuum system operating both as a FIM and as a vacuum quenching unit for fine wires. A solenoid operated unit for quenching larger wires in liquid metals is in the planning stage.





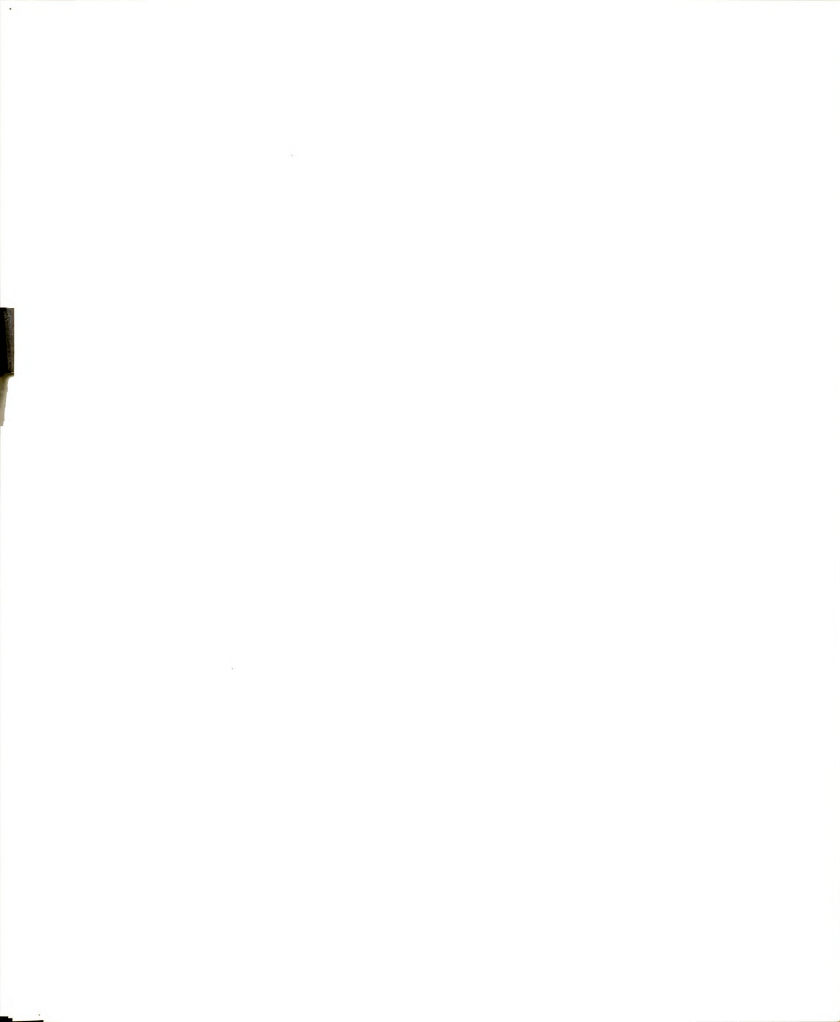
## B. The Pumping System

Figure III-1 shows a schematic drawing of the pumping system and the vacuum chamber. The entire system has been built on a movable cart topped by a 2 inch thick box made of 1/2 inch thick transite filled with glass wool. This box provides mechanical support for the vacuum chamber resting on its top while providing heat insulation between the bakeable and non-bakeable sections of the system. All connections made above the transite table use OFHC copper gaskets so that this entire section of the vacuum system is bakeable to higher than 450°C.

The ultimate vacuum in the chamber is attained in two stages. In the first stage, the two valves between the sample chamber and the sorption pump\* are opened to allow the gases in the chamber to be adsorbed by the pre-chilled adsorbant in the pump. Once the pressure in the chamber has been lowered to less than one torr, the 2 1/2 inch bakeable valve is opened and the system is pumped out all the way back to the 1 1/2 inch Veeco valve at the outlet of the diffusion pump. (When not in use, the diffusion pump is usually kept under vacuum and sealed between these two valves.) When the pressure has dropped to lower than ten millitorrs, the roughing stage of the pump-down is finished, and the sorption pump is valved off

---

\*Sorption pumps are completely oil-free pumps which lower the pressure in the system to below 1 millitorr by adsorbing gases on the activated surface of an adsorbant. The 40 liter sorption pump used in our system is manufactured by Varian Associates.



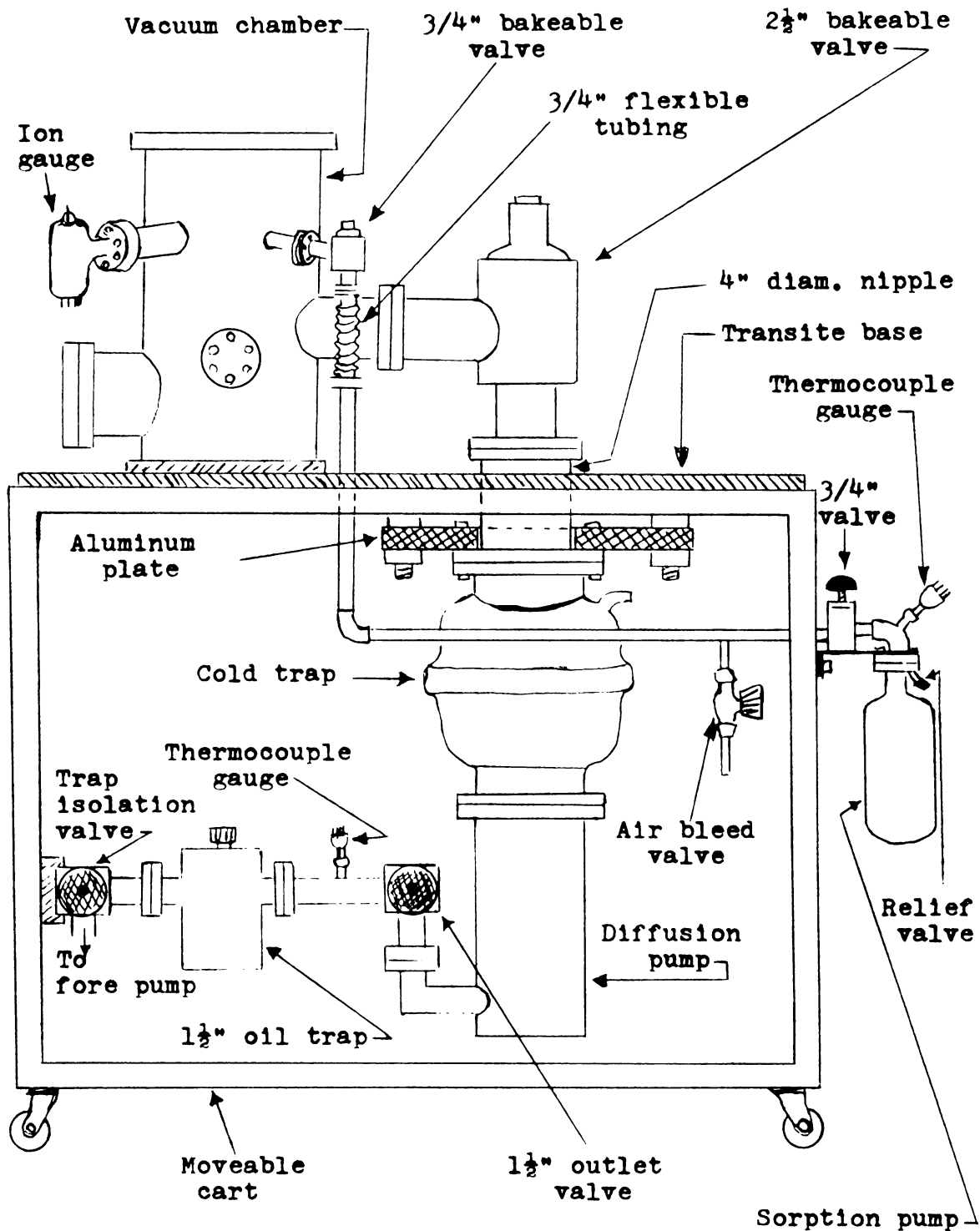


FIGURE III-1: SCHEMATIC DIAGRAM OF THE PUMPING SYSTEM AND THE VACUUM CHAMBER.



from the system. As the sorption pump warms up, the adsorbed gases begin to evaporate and are released to the air through a relief valve.

The second pumping stage is carried out by a diffusion pump,\* which is backed by a mechanical forepump.\*\* A 4 inch liquid nitrogen cold trap\*\*\* prevents diffusion of any oil molecules into the vacuum chamber. The cold trap is separated from the 2 1/2 inch valve by a 4 inch diameter, 8 inch long stainless steel nipple so that the trap will remain cool during bakeouts. The flanges at the nipple and the top of the cold trap are bolted together and to a 1/2 inch thick aluminum plate. This plate, which mechanically supports the weight of the diffusion pump, trap, nipple and the 2 1/2 inch valve, is suspended on four large bolts attached to the cart.

At the start of the second pumping stage, the 2 1/2 inch valve is closed, the diffusion pump is turned on and

---

\*The diffusion pump is a 4 inch diameter pump manufactured by T-M Engineering Co. It is designed to produce exceptionally low backstreaming. Moreover, it is a very fast pump with rather short start-up and shut-down times which allows full speed pumping in less than five minutes from a cold start.

\*\*A Welch Duoseal model no. 1204 mechanical pump is used to properly back the diffusion pump of the size given above. It is separated from the diffusion pump by a 1 1/2 inch Ultek foreline trap which keeps the forepump oil from contaminating the diffusion pump oil.

\*\*\*This 4 inch Granville-Phillips cold trap has a very efficient design for trapping oil molecules. It provides no path through the trap which does not come in contact with a surface at liquid nitrogen temperature. Moreover, it does not need frequent refilling since it holds liquid Nitrogen for over 12 hours.



liquid nitrogen is introduced into the cold trap. The outlet valve of the diffusion pump and the 1 1/2 inch trap isolation valve are opened to allow the forepump to back the diffusion pump. In a few minutes, when the diffusion pump is at full speed, the 2 1/2 inch valve is opened to allow the vacuum chamber to be pumped out by the diffusion pump. In about two hours the pressure in the chamber will be lowered to about  $1 \times 10^{-7}$  torr. Any further drop in the pressure without extensive pumping will require a mild bakeout to at least  $100^{\circ}\text{C}$  to drive moisture out of the system. A bakeout is also helpful in outgassing the vacuum system, that is, driving adsorbed gases out of the walls of the vacuum system. After experimenting with bakeouts as high as  $400^{\circ}\text{C}$ , we concluded that a few hours bakeout of  $175^{\circ}\text{C}$  is quite sufficient for outgassing the vacuum system.

After the diffusion pump has been pumping on the system for about a half hour, we bake out the entire portion above the transite base. A bakeout oven which is suspended on a hoist mechanism is lowered on the system until it rests on the transite base and is then set to the desired temperature.

Starting from a clean system we have repeatedly been able to attain pressures below  $1.2 \times 10^{-9}$  torr with twelve hours pumping, and below  $9 \times 10^{-10}$  torr with 36 hours pumping after 4 hours of bakeout at  $175^{\circ}\text{C}$ .





### C. The Vacuum Chamber

The vacuum chamber consists of an 8 inch diameter, 17 inch high stainless steel cylinder closed at the bottom, which has nine access ports of various sizes. Except for one 3/4 inch diameter spare port, each of the ports is currently being used to accommodate one or more of the connections needed to make the chamber functional in its designed multiple-purpose capacity.

Figure III-2 shows a schematic diagram of the chamber, including a description of the function(s) of each of the nine ports. For simplicity, the various attachments to these ports are not shown.

At the present time plans are being made to switch the function of some of the ports to free two 1 1/2 inch ports for addition of a titanium sublimation pump\* and an ion pump\*\* to the vacuum chamber. The addition of these pumps will increase the pumping speed of the system and should allow ultimate pressures in the  $10^{-10}$  to  $10^{-11}$  torr range. However, the implementation of these plans is contingent upon funds becoming available.

---

\*This pump operates by flashing a fresh film of titanium over the walls of the pump. This titanium removes gas molecules from the system by chemically reacting with them. It does not pump inert gases.

\*\*Ion pumps operate by emitting electrons from a hot filament and making them spiral in a magnetic field (to create a long effective path). Collision of these electrons with the gas molecules in the system ionizes them, after which they are accelerated toward a titanium cathode in which they will be buried.

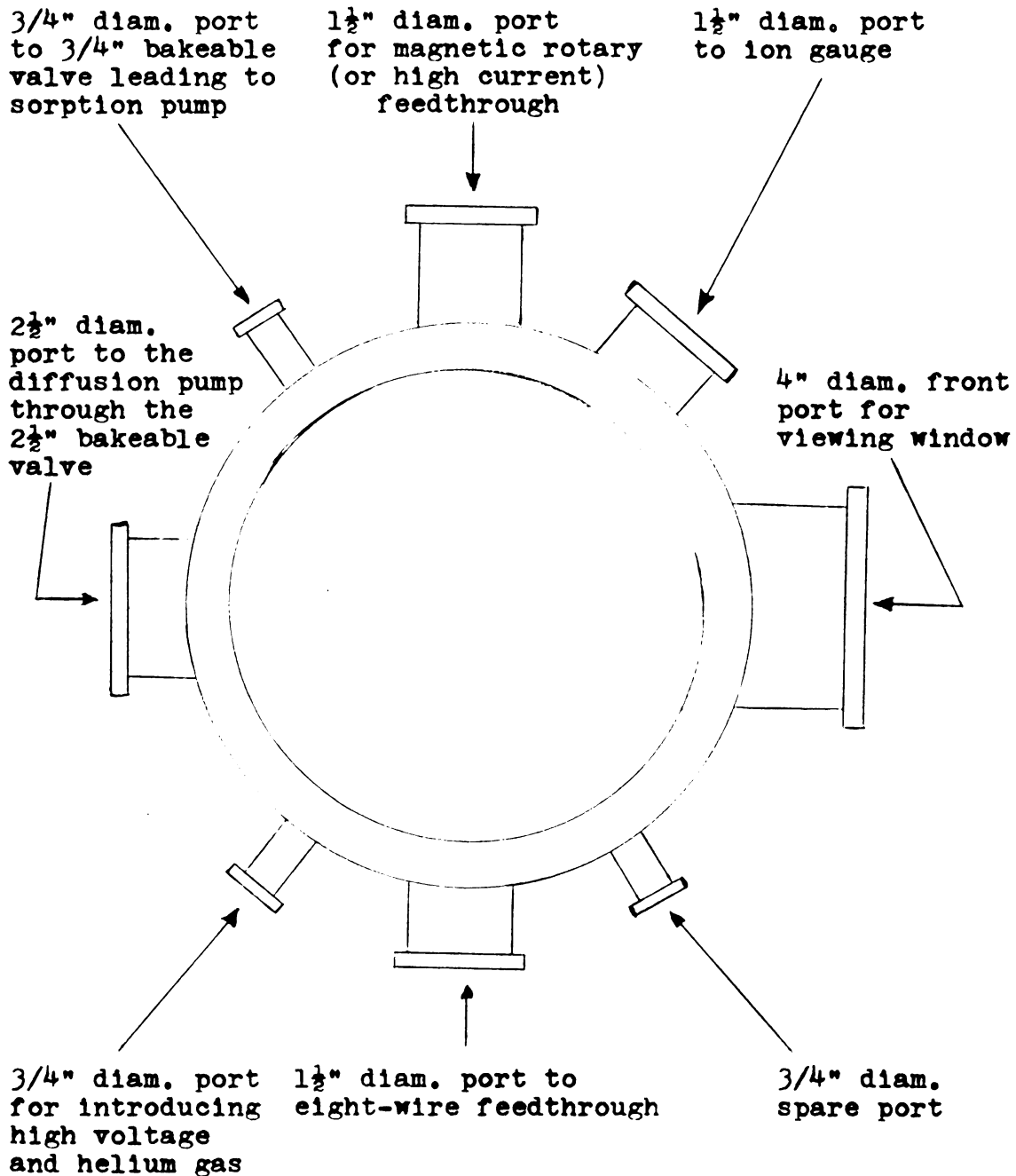


FIGURE III-2: SCHEMATIC DIAGRAM OF THE VACUUM CHAMBER AS VIEWED FROM ABOVE.



#### IV. THE FIELD ION MICROSCOPE SYSTEM

##### A. Introduction

Until recently, the study of point defects in metals was hampered by lack of the atomic resolution needed to see individual defects and small defect clusters. Analyses of experimental data obtained from macroscopic measurements always involved assumptions concerning the behavior of the microscopic defects; assumptions which could rarely be independently verified.

The potential solution to this problem was provided by Müller (31) in the early 1950's, when he showed that atomic resolution could be obtained using a FIM operated at cryogenic temperatures (for details of the operation of a FIM see Appendix A). However, it was only recently that quantitative investigations of point defects became feasible. The intervening years have seen great strides in the production of ultra-high vacuum and image intensification devices at reasonable cost, production of purer imaging gases, development of more refined techniques for sample preparation and imaging, and finally, in the understanding of the behavior of samples in a FIM. The last few years have seen a number of ever more quantitative studies of point defects, culminating in the recent

development by the Cornell group of Profs. Seidman and Balluffi of a data analysis system for accurate measurements of defect concentrations. It was these developments which just over two years ago led us to begin design and construction of a FIM, coupled to a data analysis system patterned on that developed by the Cornell group.

Our decision to branch into field ion microscopy required learning many experimental techniques unfamiliar to us at the time. Before proceeding to design our final all-metal microscope, we first experimented with a simple prototype glass microscope which we built to familiarize ourselves with the various aspects of field ion microscopy. After a few months, preparation of the FIM samples remained as the only major source of difficulty with the operation of our microscope; our initial rate of sample failure approached 80 per cent.\* Since each experimental run with the FIM requires about a full day of preparation time, improving our sample fabrication techniques by a trial and error procedure proved to be an extremely time-consuming and frustrating task. To solve this problem we developed a novel method of selective shielding which allowed incorporation of several sample tips at time into the microscope.

---

\*A sample tip will not produce a useful image when a) it is too blunt or irregular, or b) it fails (or "pops") due to internal defects when subjected to the immense electric fields present in a FIM (see Appendix A).

Although the idea of selective shielding is in principle a simple one, the experimental problems encountered in its implementation were not trivial. These experimental problems were gradually overcome as we designed and constructed our second microscope, a liquid nitrogen cooled glass FIM equipped with a four-sample capacity sample rotator and an internal image intensifier. Because of its insufficiently high vacuum ( $\sim 10^{-7}$  torr) and its insufficiently low temperature ( $\sim 78\text{K}$ ) capabilities, this microscope is not suitable for quantitative FIM work. However, it is an excellent microscope for qualitative studies, and its construction enabled us to overcome our experimental problems, prior to proceeding with the design of our all-metal microscope.

The final step in the development of our FIM system was the construction of our all-metal liquid helium cooled microscope and the data analysis system necessary for quantitative FIM studies. This all-metal FIM was designed in conjunction with the ultra-high vacuum system and has been equipped with accessories which make it a unique instrument. Some of its important features are:

- 1) A magnetically operated five-sample capacity internal sample rotator.
- 2) An internal image intensifier.
- 3) Ability to tolerate high temperature bake-outs and operate with an ultra-high vacuum as background for the imaging gas.

- 4) A double-dewar system including an outer jacket for liquid nitrogen and an inner 3-liter dewar for either liquid nitrogen or liquid helium.
- 5) A temperature control unit operating with cold helium gas which can be used in place of a cryogenic liquid in the center dewar and which controls the temperature of the copper plug leading to the FIM samples between 4.2K and 78K.

The first of these features introduces great convenience in operating the FIM by reducing turnover time per sample, and by providing reserve samples which can quickly replace defective sample tips.

The combination of the last four features allows us to obtain clear, stable, and intensified images for the FIM samples, and record these images on film within reasonably short photographic times. The data recorded on the film can be quantitatively analyzed at a later time.

In the following sections of this chapter, we will describe the principle of operation of our new sample rotator system and show how it has been included in both of our FIMs. The data analysis system that we have developed for quantitative FIM studies will be described subsequently.

#### B. Motivation for Inclusion of Multiple Samples in a FIM

Observation of the image of a sample in a field ion microscope is usually preceded by the relatively long

pump-down and bake-out times necessary to achieve ultra-high vacuum. Additional time is required for cooling the sample to cryogenic temperatures and introducing the imaging gas. In cases of sample failure, which are not uncommon in field ion microscopy (32)(33), both this preparation time, as well as any cryogenic liquid in the system (which must be boiled off before the FIM can be opened to air) are totally wasted. Even when the samples do not fail, it is very time consuming to investigate many samples, since the times involved in the above-mentioned processes can occupy as much as a full day. In order to avoid this wasted time, systems have been devised which allow the introduction of new samples into the vacuum chamber through a series of intermediate vacuum locks (34). However, such systems are inherently complicated and expensive.

Here we will describe an alternative method for sample changing which is more convenient, less time consuming, and considerably less expensive. The method consists of building into the FIM a sample wheel, accommodating a number of samples, which can be rotated externally so as to bring these samples sequentially into the imaging position. By introducing a multiple sample capability, the inconvenience of a long preparation time is reduced, and failure of a single sample is no longer catastrophic.

Rotating sample holders have been used in a variety



of low temperature systems, but no one has previously suggested how to solve the problems unique to the FIM. Foremost among these is the problem of protecting the samples which are not being imaged from the high voltage used to image the sample of interest. In the next section we describe a general method of selective shielding which solves this fundamental problem. Also of importance are secondary problems associated with maintaining simultaneously ultra-high vacuum, proper sample alignment, electrical insulation for the high voltage parts of the system, and good thermal contact between the sample wheel and the low temperature bath, while keeping the sample wheel easily rotatable from the outside. The solutions to these problems are described in subsequent sections in terms of designs for sample rotator systems which we have built into a glass and an all-metal FIM. These solutions are not necessarily unique, and are to some extent dependent upon the designs of the specific FIMs. However, they should be adaptable to most conventional FIMs, and they have two advantages; 1) they are inexpensive and can be constructed in any research laboratory with shop facilities, and 2) they have been demonstrated to operate reliably and well over long periods of time.

### C. Selective Shielding

A normal, single sample FIM is operated with the sample tip either unshielded or surrounded by a single grounded shield (35). In either case a sample wheel can

not be introduced, because the samples which are not being imaged will be destroyed by the high voltage used to image the sample of interest. We have solved this problem by using two shields; an inner shield, held at the same electrical potential as both the wheel and the tips, which electrically shields all of the tips except the one facing the fluorescent screen, and an outer grounded shield which serves to minimize an undesirable side effect produced by the inner shield.

The basic system is shown in Figure IV-1. The sample wheel is enclosed within a cylindrical high voltage shield which has an opening facing the grounded fluorescent screen. A major effect of such a shield is to raise the "Best Image Voltage" (BIV), the voltage required to produce the sharpest image, by a factor  $S > 1$  (called the "shielding factor") (36). This increase in the BIV was purposely introduced by Müller, et al (36) and by Weizer (37) as a means of increasing the image brightness, which was a point of extreme concern during the early years of field ion microscopy. Today, with the ready availability of inexpensive image intensification systems, brighter images are no longer a requirement. In fact, for our purposes an increase in the BIV was a distinct disadvantage, since it would have necessitated greater care to keep the system from suffering electrical breakdown.

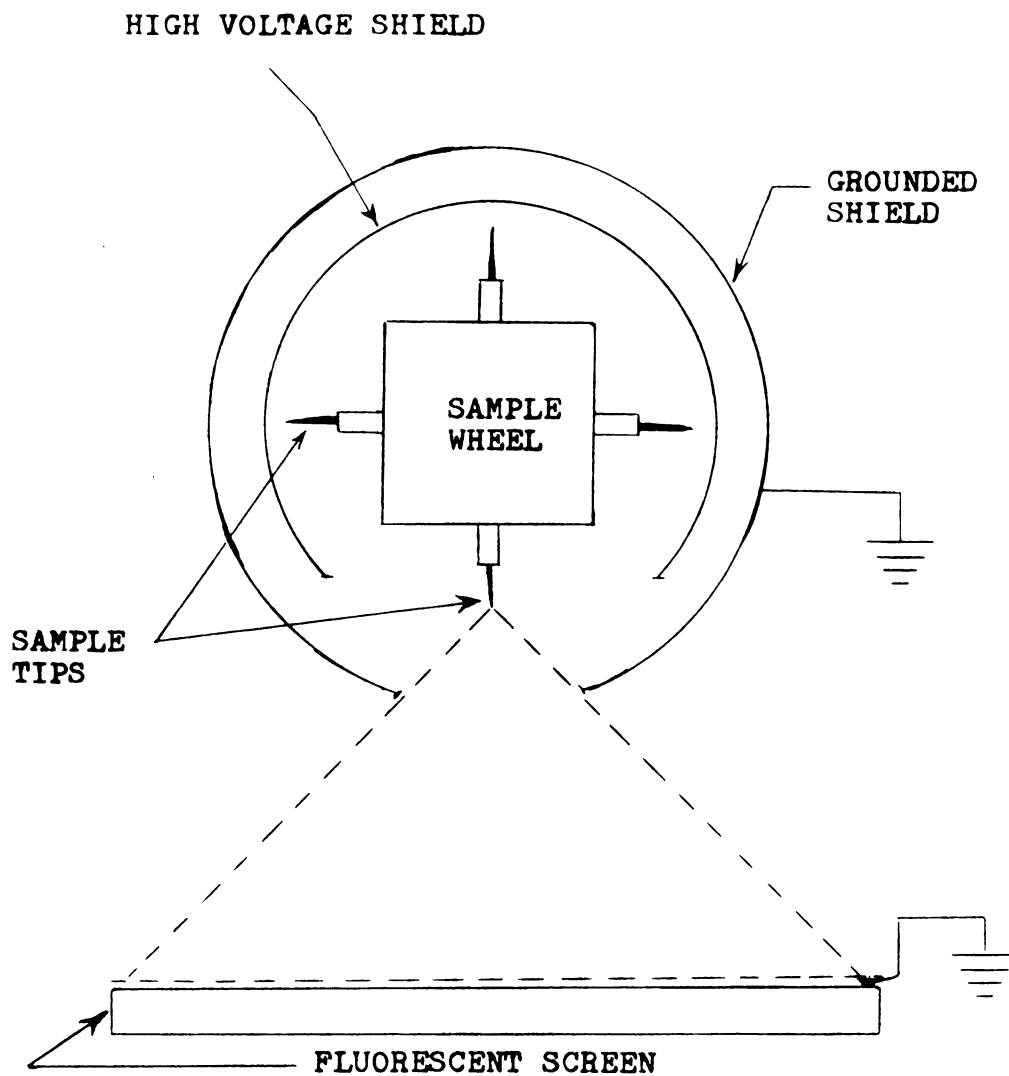


FIGURE IV-1: THE BASIC MULTI-SAMPLE SYSTEM; A SAMPLE WHEEL SURROUNDED BY HIGH VOLTAGE AND GROUNDED SHIELDS.

Figure IV-2 (after Müller and Nishikawa (36)) shows how the shielding factor  $S$  varies as a function of  $L/d$ , where  $L$  is the distance from the tip of the FIM sample to the high voltage shield with an opening of diameter  $d$ . Considering the values of  $L$  and  $d$  consistent with the free rotation of the sample wheel and the available space in a FIM, from the data on Figure IV-2, it appeared that we could not reduce  $S$  lower than about 2.

At this point we conducted a careful study of the equipotential lines in a saltwater simulation of the FIM situation and discovered how  $S$  could be lowered further. By surrounding the high voltage shield with a grounded shield with a smaller opening, we were able to produce equipotential lines similar to those obtained in the absence of both shields, i.e.  $S \approx 1$ . This is the reason for the grounded shield shown in Figure IV-1.

In designing our sample rotators we followed the above guidelines for reducing the shielding factor. We made the hole in the inner shield as large as possible consistent with shielding the samples not facing the fluorescent screen, and situated the samples on the wheel so that when being imaged they protruded through this hole. We also surrounded the inner shield with a second grounded shield, having a smaller hole (in the glass system, the ratio of the two solid angles subtended at the sample was 1:2, and in the metal system 1:4), thereby further lessening the effect of the inner shield on the sample

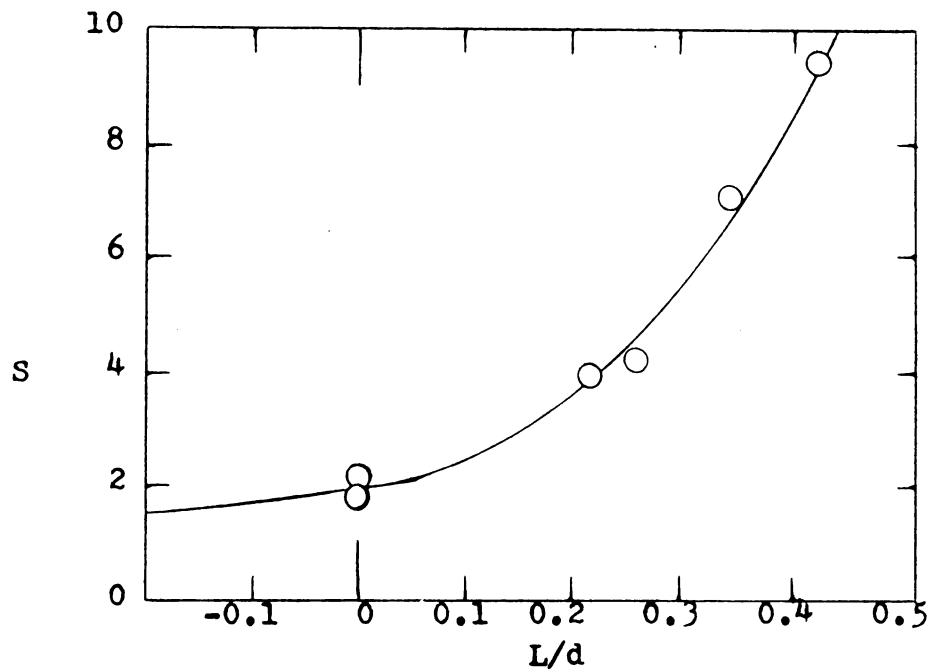
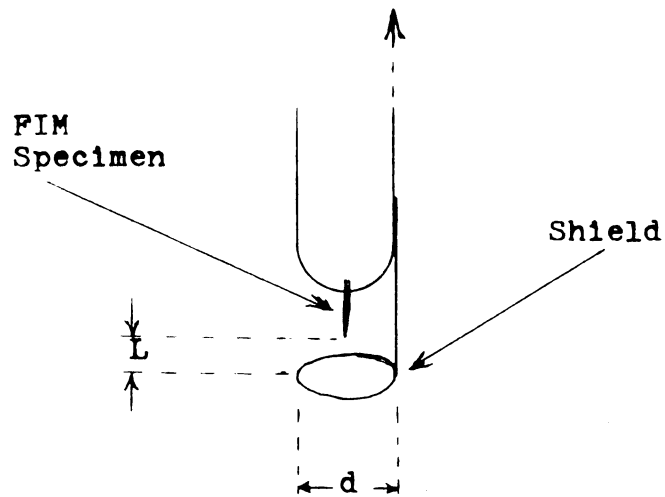


FIGURE IV-2; (AFTER MÜLLER AND NISHIKAWA) DEPENDENCE OF THE SHIELDING FACTOR  $S$  UPON  $L/d$  FOR A SHIELD AT THE SAME POTENTIAL AS THE FIM TIP.

being imaged. With these procedures we obtained Best Image Voltages similar to those obtained in the absence of the high voltage shield, that is, similar to those for a normal single tip FIM. (It should be noted that when the grounded shield opening is smaller than that of the high voltage shield, the high voltage must be turned off before the sample wheel is rotated. Failure to do this will result in the destruction of the tip as it moves into close proximity with the grounded shield.)

#### D. Sample Rotator for a Liquid Nitrogen Cooled Glass FIM

Figure IV-3 shows the inexpensive sample rotator we have added to our liquid nitrogen cooled glass FIM as it would be seen looking from the fluorescent screen. For simplicity the FIM body and the vacuum system are not shown, and the high voltage and grounded shields are shown separately. The sample wheel is machined from OFHC copper to have a 3mm diameter shaft, which passes upward through a clearance hole in an aluminum support plate. The sample wheel is positioned vertically with respect to the support plate by means of a retainer ring. The support plate is held in place by four set screws which extend inward from the aluminum support walls. These set screws go into clearance holes in the support plate, thereby providing the loose support necessary to avoid strain of the glass-to-metal seals due to thermal contraction as the system cools. Each support wall is

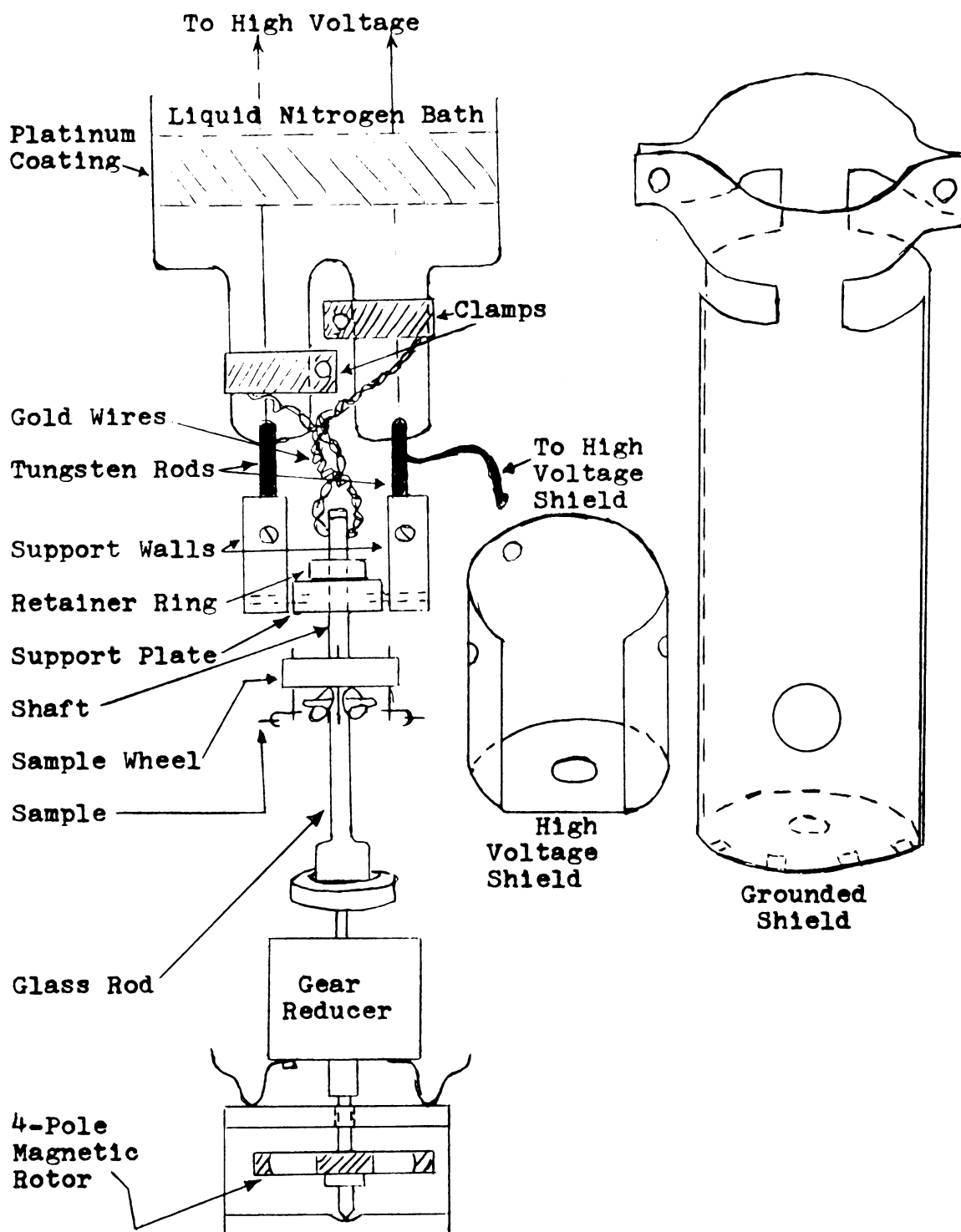


FIGURE IV-3: SCHEMATIC DRAWING OF A SAMPLE ROTATOR SYSTEM FOR A LIQUID NITROGEN COOLED GLASS FIM. THE HIGH VOLTAGE AND GROUNDED SHIELDS ARE SHOWN SEPARATELY.

connected to the liquid nitrogen bath via a tungsten rod, which passes through a glass-to-metal seal from the vacuum chamber into the liquid nitrogen chamber. To increase the thermal linkage between the sample wheel and the liquid nitrogen bath, a number of flexible gold wires connect the shaft of the sample wheel to the two fingers at the bottom of the liquid nitrogen chamber. Twenty of these wires, 18cm long and 0.15mm in diameter, are passed through a hole at the end of the sample wheel shaft and pressed against the shaft by means of a lock washer and screw. This produces two bundles of 20 wires, each 9cm long. The wires in each bundle are twisted together, wrapped around one of the two glass fingers at the end of the liquid nitrogen chamber, and clamped tightly to it by a cylindrical clamp.

External control of the sample rotation is achieved by means of a magnetically coupled rotary feedthrough consisting of four bar magnets located outside the FIM and a four-pole magnetic rotor located inside it. This rotor is attached to a vertical shaft, the upper end of which goes to a 17 to 1 gear reducer,\* which in turn is loosely coupled to the paddle-shaped end of a glass rod. The other end of this rod is T-shaped and hangs from two

---

\*The gear reducer was necessary to multiply the torque of our bar magnets, since the size of the system kept these magnets rather far from the rotator inside the FIM. Since it contains bronze gears, the reducer is unsuitable for high temperature bakeouts.



loops of stainless steel wire bolted to the bottom of the sample wheel. By rotating the outside magnets, the sample wheel can be turned so as to position any one of the four samples toward the screen (or, as in our case, toward a micro-channel plate image intensifier). Since the system is made of glass, the sample wheel can be observed through the hole in the grounded shield, and the sample positioned by eye. The time for switching samples is about one minute. All through the process the samples remain cold and the vacuum is maintained.

The high voltage shield is a split cylinder (see Figure IV-3) made of thin OFHC copper, which slips around the outside of the support walls and is held in place with one screw through one support wall and a small piece of 1.5mm thick alumina rod inserted through a hole into the other support wall. This procedure is used to reduce strain on the glass-to-metal seals upon cooling. Thermal contact between the bath and the high voltage shield is achieved by bolting the free ends of 6 gold wires to the shield. The other ends of these wires are spotwelded to one of the tungsten rods, using platinum as an intermediary.

The opening in the high voltage shield is rectangular, with the plane of the rectangle located behind the sample which is being imaged. We initially tried a circular opening in this shield, but found this produced elliptical images. We attribute this effect to the fact that the sides of the circular hole were behind the

sample tip, resulting in a lower shielding factor than that due to the top and bottom edges, which extended in front of the sample tip.

The grounded shield consists of two half cylinders which have their ends pulled together around the main body (30mm diameter) of the liquid nitrogen chamber. To improve thermal contact, the surface of the glass is coated with liquid bright platinum where these contacts are made.

Although the distance between the outer wall of the high voltage shield and the inner wall of the grounded shield is only about 4mm, we have not experienced discharges with voltages as large as 40kV.

Each FIM tip is spotwelded to a 0.25mm diameter platinum wire which is itself spotwelded to a 1mm diameter tungsten rod. The tungsten rods fit very snugly into four holes in the sample wheel, and are held in place by set screws. Differential thermal contraction between the tungsten and the copper of the sample wheel leads to very good thermal contact at low temperatures. The temperature of the platinum wire has been measured to be less than a degree above that of the wheel which in turn is about 4K above that of the liquid nitrogen bath (78K).

#### E. The All-metal Liquid Helium Cooled FIM

Our second FIM is an all-metal double dewar system. With the exception of the high voltage leads, the helium

gas leak, and the viewing window, all parts associated with the FIM are constructed on a single 10 inch diameter standard flange which mounts on top of the cylindrical vacuum chamber (see Chapter III). Replacing this FIM top with a blank-off flange frees the vacuum system for other purposes.

Figure IV-4 shows the general design of the double dewar system and the sample rotator assembly. The grounded shield and the high voltage shield are shown here with dashed lines (for details of these shields see Figure IV-5). The sample wheel, made of gold plated OFHC copper, is in the form of a central ring with five equally spaced spokes radiating outward. The top and bottom faces of the central ring are grooved to contain 1mm diameter stainless steel balls. This wheel fits around a gold-plated copper plug (copper plug #2), and rotates between two thrust bearings, one formed by the stainless steel balls held between the top face of the ring and a lip on copper plug #2, and the other formed by the balls held between the bottom face of the ring and a retainer ring. A 10mm diameter, 30mm long sapphire rod connects copper plug #2 to a second plug, copper plug #1, which protrudes through and is welded to the bottom of the liquid helium dewar. The sapphire provides a thermal link to the helium bath while simultaneously providing the electrical isolation necessary to operate the sample wheel at up to 30kV above ground. In order

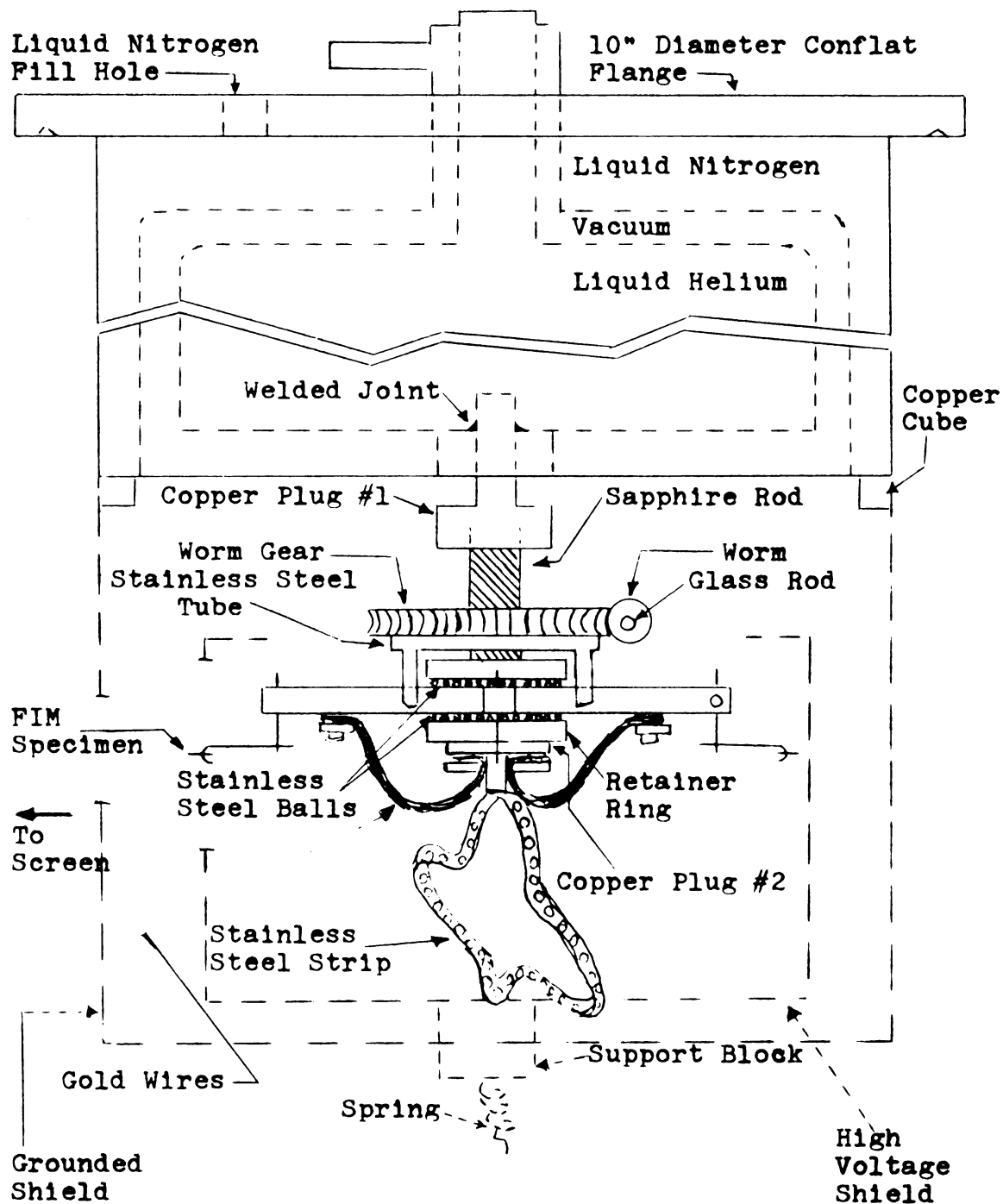


FIGURE IV-4: SCHEMATIC DRAWING OF A SAMPLE ROTATOR SYSTEM FOR A LIQUID HELIUM COOLED METAL FIM.

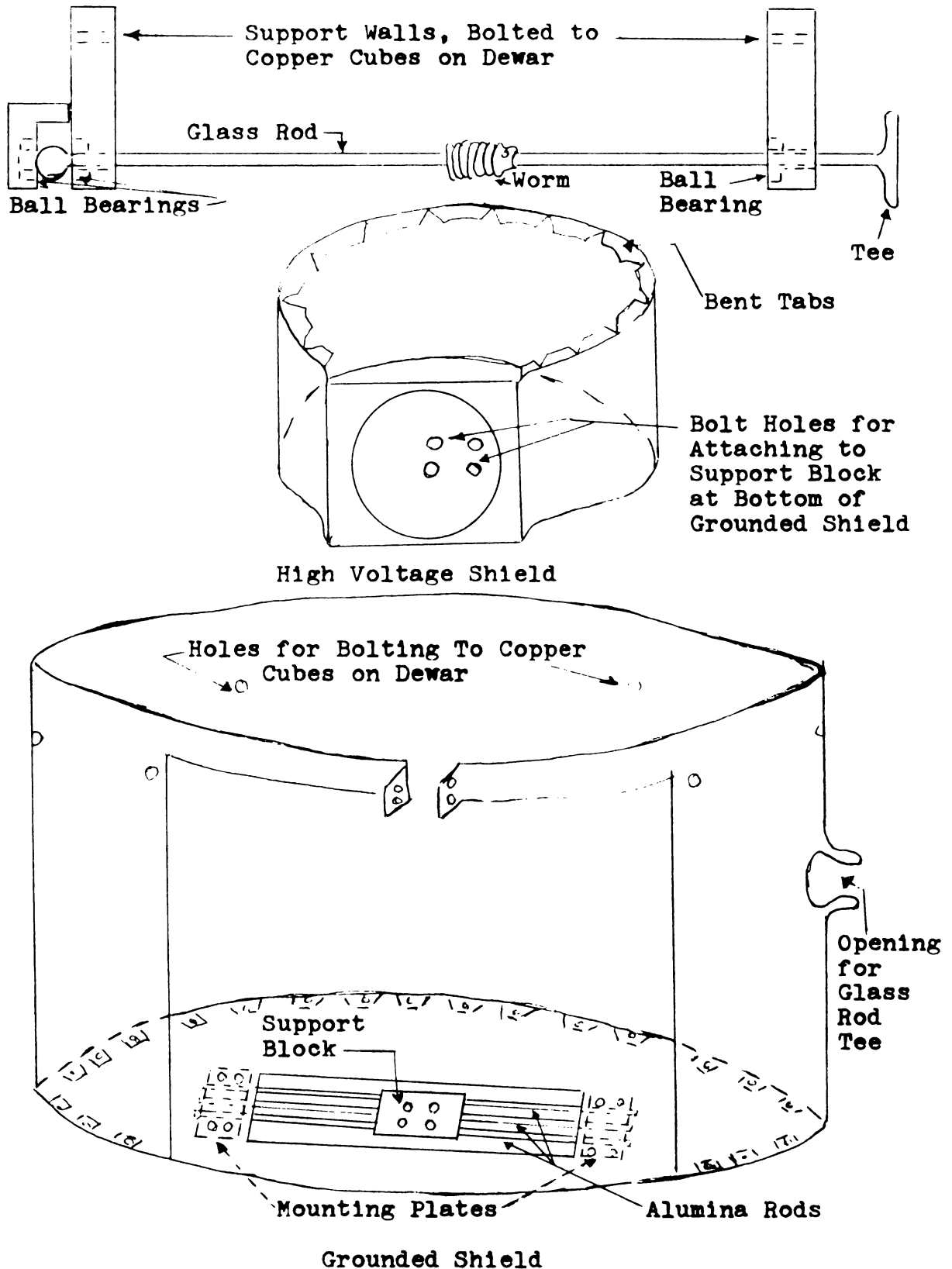


FIGURE IV-5: THE DESIGN OF HIGH VOLTAGE AND GROUNDING SHIELDS AND A HOLDER FOR THE GLASS ROD USED TO CONNECT THE MAGNETIC ROTATOR SYSTEM TO THE WORM GEAR.



to ensure good thermal contact between the sapphire and the two plugs, a gold coating was evaporated onto each end of the sapphire rod, and its ends were forcibly inserted into the plugs while the plugs were heated. This yields a rigid mechanical connection at room temperature, which is improved by differential thermal contraction upon cooling.

Thermal contact between the sample wheel and copper plug #2 is provided by five cables, each made of twenty 6cm long pieces of 0.15mm diameter gold wire, extending from the bottom of copper plug #2 and bolted to each spoke of the wheel. The wires are bolted against the lower face of the copper plug #2. Where the wires are bolted, the gold to gold contacts not only had a low initial thermal resistance, but after one bake-out formed welded junctions.

The five FIM samples are mounted on the ends of the spokes in the same way as described for the glass system. Their temperature can be maintained at values ranging from about 78K to below 10K. To operate the FIM at liquid nitrogen temperature ( $T \approx 78K$ ), liquid nitrogen is put into both the inner and outer dewars. To go below 78K, liquid nitrogen is put into the outer dewar, and a vacuum pump is used to bring cold helium gas from a liquid helium storage dewar, through a transfer tube, and into contact with copper plug #1, which projects from the central helium dewar into the vacuum chamber. By controlling the rate

of gas flow it is possible to maintain constant temperatures between 78K and 4.2K at the copper rod. If liquid helium is allowed to collect in the central dewar, the samples out at the end of the spokes reach a temperature below 10K. The central dewar has a liquid helium capacity of 3 liters, which allows the samples to be maintained below 10K for about 2 1/2 hours without refilling. At higher temperatures the liquid helium consumption is smaller.

The rotation mechanism is coupled to the sample wheel through a thin walled stainless steel tube having tabs which are bolted to the central ring of the sample wheel. The other end of the tube passes through the center of a stainless steel worm gear, to which it is bolted. The worm which drives the worm gear fits closely around a glass rod, which is used as a drive shaft providing both thermal and electrical insulation of the sample wheel from the drive mechanism. This drive shaft is held by three stainless steel ball bearings which are mounted in stainless steel support walls bolted to the liquid nitrogen chamber. A ball formed at one end of the glass rod prevents the rod from moving longitudinally (see Figure IV-5) while the other T-shaped end of the rod mates with a grooved coupling. This coupling is attached to the shaft of a 6 pole magnetic rotor which, in conjunction with a 6 pole magnet system outside the dewar, forms the magnetic rotation assembly.





The sample wheel is electrically connected to the high voltage shield through a short rod, extending downward from copper plug #2, which is bolted to a long strip of 1/2cm wide, 1/2mm thick stainless steel, punched with holes to reduce thermal conductivity. This strip is bent into the shape shown in Figure IV-4, and serves both to connect the high voltage to the sample wheel and to press copper plug #2 against the sapphire rod to prevent loosening of the joint during bakeout.

The high voltage shield is made of 1mm thick OFHC copper in the shape of a cylinder with one section of its wall pushed out and flattened (see Figures IV-4 and IV-5). A 5cm diameter hole forms the opening in this shield. The high voltage shield sits on a rectangular gold-plated OFHC copper block, which is pierced by three 4mm diameter alumina rods, metallized in the regions of contact so as to provide low thermal resistance. These rods are held tightly against the bottom of the grounded shield by plates. The rods serve to isolate the high voltage shield electrically from ground, while connecting it thermally to the grounded shield which is at liquid nitrogen temperature. The copper block is connected to the high voltage lead at the bottom of the vacuum system by means of a spring which makes contact as the FIM body is lowered into the vacuum chamber.

The grounded shield is made of 0.5mm thick OFHC copper in the form of a cylinder with a front section of

its wall removed. It is loosely bolted to a number of copper cubes which are welded to the bottom of the liquid nitrogen chamber. Good thermal contact is made by pulling the two strips above the removed section together so as to clamp the shield around the liquid nitrogen jacket. The front section of the grounded shield (not shown in Figure IV-5), which contains the 2.5cm diameter opening through which the sample faces the screen, is separately bolted to the liquid nitrogen chamber and to the bottom of the grounded shield. This arrangement allows a set of samples to be changed by removing only this front plate, leaving the rest of the FIM assembly intact.

In this all-metal system, the position of the sample wheel can be observed only through the front viewing window, which is mostly covered by the micro-channel plate assembly. Although it is possible to follow the motion of the wheel by monitoring the rotation of the outside magnets of the magnetic rotor, we found it more convenient to truncate the circular micro-channel plate holder so as to leave openings through which to view the sample wheel directly.

#### F. Final Comments on the Sample Rotator

A useful byproduct of the sample changers described above is the capability for movement of the sample tip in the horizontal plane. We have found this capability particularly useful for determining whether an irregularity

in a FIM image is associated with the FIM specimen, and for centering a desired plane of the crystal on the screen. This latter feature would be especially useful to experimenters using a small micro-channel plate, which permits viewing only a small portion of the potential image.

It should be noted that a sample rotator for a metal FIM not containing an internal image intensifier can be made even more simply than the one described above. In this case the sample wheel can be grounded and the fluorescent screen held at a large negative potential. Under these conditions it should be possible to do away with the sapphire rod and to use only one grounded shield. Biasing difficulties make this scheme less attractive when an internal image intensifier is present.

#### G. Image Intensification

In the absence of image intensification the brightness of a FIM image is extremely low. It is visible to the human eye only after several minutes of dark adapting in total darkness. Depending on various parameters, the times for obtaining photographs of FIM images vary between a few minutes to an hour or more. The efforts of a large number of the early field ion microscopists was directed toward increasing the image intensity (36)(37)(38)(39), or decreasing the photographic times (40)(41), all with modest results. The relative success of an external image

intensifier system using a magnetically focused photo-multiplier unit (42)(43) was unfortunately offset by its prohibitive cost.

The problem of the FIM image intensification was very recently alleviated by the declassification of a new breed of electron multipliers developed by Electro-Optics division of Bendix Corp. under military contracts. The operation of these electron multipliers is based on a large number of small diameter cylindrical holes (channels) which are produced in a thin glass plate (called channel plate or channeltron), and whose inside walls have a resistive secondary emission coating deposited on them. By properly biasing a channel plate on which particles (such as ions in a FIM) are incident, the secondary electrons released due to the impact of these particles are accelerated down the channels creating more secondary electrons which form a cascade shower. For each incident particle, thousands of secondary electrons emerge from the respective channel, thereby creating a large gain. The diameter of channels  $d$  and the center-to-center separation between the channels  $S$  on the channeltron determine its resolution which, in most cases, is quite sufficient for use in a FIM (typical values  $d \approx 40 \mu$ ;  $S \approx 50 \mu$ ).

The channel plate has several important advantages over all other methods of image intensification used to date in field ion microscopy:

- 1) It is relatively inexpensive.

- 2) In a FIM it substitutes large numbers of electrons for the helium ions. The immediate benefit of this is twofold: 1) the efficiency of the phosphor of the fluorescent screen is much higher for electrons than for helium ions, and 11) the heavy helium ions have a destructive effect on the phosphor, thus requiring frequent screen preparations. Electrons, on the other hand, allow a single screen to last indefinitely.
- 3) The dark noise of the channel plate is very low ( $\sim 10^{-10}$  amp)--not enough to create an appreciable amount of light on the FIM fluorescent screen.
- 4) It has a gain of better than  $10^3$ . By accelerating these electrons toward the screen, a still larger effective gain can be obtained.
- 5) In contrast to most other methods previously used, image intensification using a channel plate does not require changes in any of the normal FIM parameters such as imaging gas pressure (39), tip-to-screen distance (41), etc.

Figure IV-6 shows the design of our channel plate holder and the way that the channel plate and the fluorescent screen are electrically biased while in normal operation. For simplicity, the various parts which are normally held closely together are shown separated. The array consists of a 3 inch diameter channel plate followed by a thin ring (#1) of aluminum (outer edge 0.5mm thick, inner edge 0.25mm thick), a 1.5mm thick ring of

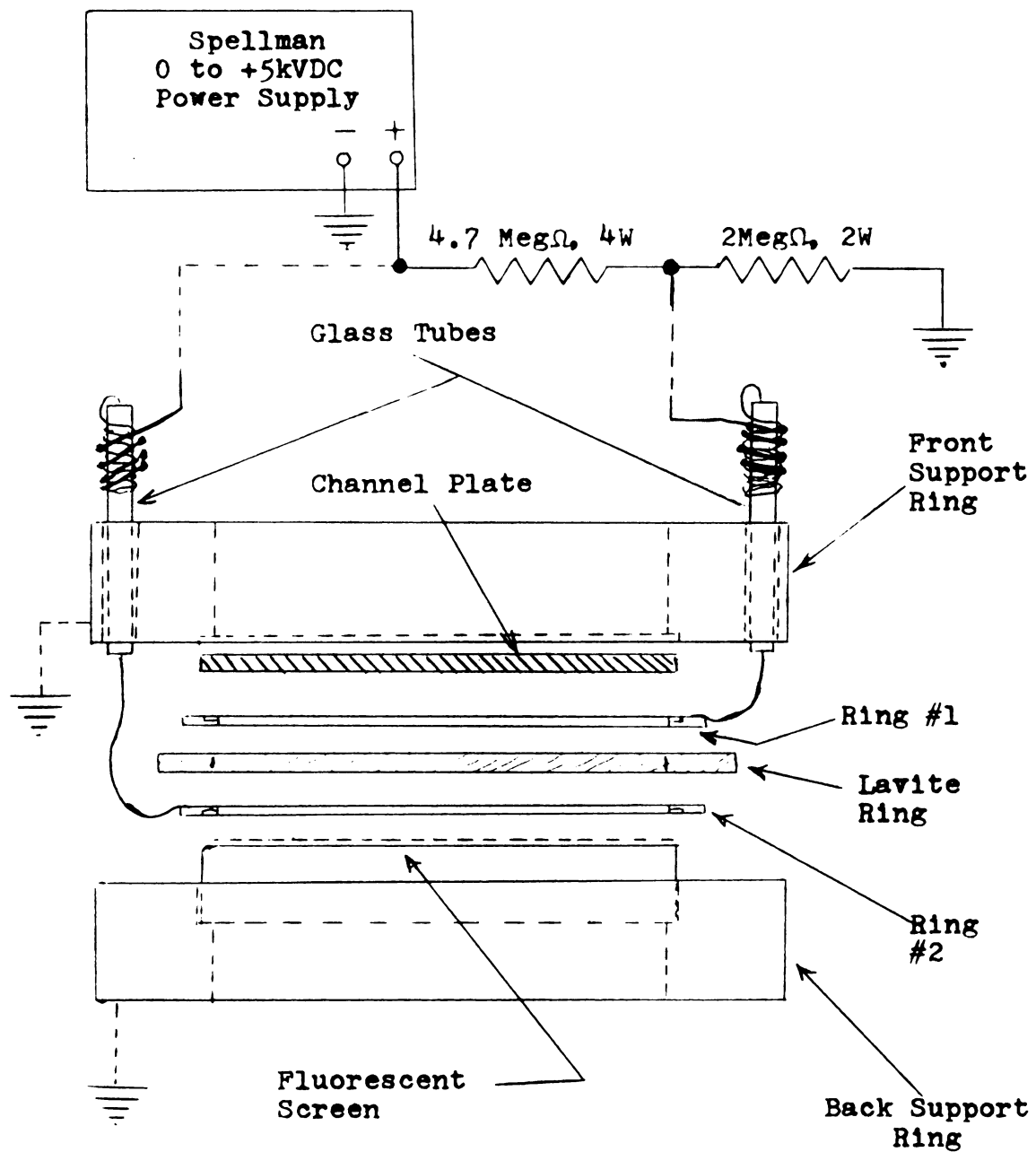


FIGURE IV-6: DESIGN OF THE CHANNEL PLATE HOLDER AND BIASING CIRCUIT.

lavite insulator, a second ring of aluminum (#2), and a 3 inch diameter fluorescent screen. The entire array is held together by two 1/4 inch thick aluminum support rings (inner diameter =  $2 \frac{15}{16}$  inch) which are lightly bolted to each other with a spring placed under each bolt. The compression of the springs is adjusted to yield a small, uniform compression around the rings, thus providing the unit with mechanical rigidity without subjecting the very fragile channel plate to undue strain. Both support rings are electrically connected to the ground.

The channel plate is confined in a 3 inch diameter, 0.25mm deep cavity in the center of the front support ring, and its front face (the face opposite the FIM tip) becomes electrically grounded by contacting the front support ring. The back face of the channel plate contacts aluminum ring #1 which is connected to the voltage divider circuit and is usually biased at about +900vDC. This properly biases the channel plate for a gain of  $\sim 3 \times 10^3$ .\* The electrons emerging from the channel plate are accelerated through a 2100 volt potential difference which exists between the back face of the channel plate and the front face of the fluorescent screen. Since the

---

\*By biasing at higher voltages, it is possible to obtain a higher gain (up to  $\sim 10^5$ ) from the channel plate at the risk of shortening its life. The specifications for our channel plates recommend 750 to 950 volts as the optimum range for obtaining a high gain and a long life.



energy of the incident electrons, as well as their number, determines the intensity of the image produced by the phosphor on the screen, an effective gain much higher than that of the channel plate alone is obtained.

The fluorescent screen is a 3 inch diameter, 1/4 inch thick glass plate polished flat to within 40 light rings. It is confined in a 3 inch diameter, 1mm deep cavity in the center of the back support ring. The front face of this screen has been coated with a transparent conductive coating of tin oxide on top of which a layer of phosphor powder has been deposited (see Section H below).

Aluminum ring #2 supplies a positive potential of about 3kV to the outer edge of the screen. The light produced by the screen is observed through its back face.

The voltages supplied to the back face of the channel plate and the front face of the screen are brought in through two 3mm diameter glass tubes which are held in place in the front support ring by set screws. The fine gold wires leading to aluminum rings #1 and #2 are passed through these glass tubes and are tightly wrapped around the outside of these tubes. When the channel plate unit is placed in the FIM, the wires coming from the high vacuum electrical feedthroughs are simply wrapped over the gold wires.

The electron beams emerging from various channels on the channel plate are not perfectly focused. If the screen is placed far away from the channel plate, the divergence

of these beams causes great loss of resolution. In the design of our holder, the thickness of the lavite ring (which was pre-baked at  $800^{\circ}\text{C}$  to increase its resistivity) has been chosen such that it properly insulates the screen from the back face of the channel plate, and yet it is thin enough to preserve the resolution of the channel plate (proximity focusing).

#### H. Experimental Techniques

There are, in general, four separate experimental domains associated with field ion microscopy: fabrication of basic FIM components, vacuum technology, still and motion picture photography, and high voltage technology. We have already described our vacuum techniques in Chapter III, and the photographic and high voltage techniques will be discussed in the section on data acquisition system (see Section J below). In this part we will describe the techniques for fabricating various components basic to the FIM.

The techniques described below were copied after descriptions given in the literature. We will, therefore, cite the references from which the instructions were taken, and mention only the points which we found were either not specified or not sufficiently emphasized in the literature.

### H.1) Preparation of a Conductive Transparent Coating on the FIM Screen

A conductive transparent coating of tin oxide can be deposited on the surface of glass by a method described by Gomer (44). Crystals of tin chloride ( $\text{SnCl}_2 \cdot 2\text{H}_2\text{O}$ ) are heated until they are melted and the fumes produced are forced by puffs of air to blow over the surface of the glass which must be heated to  $400-450^\circ\text{C}$ . It is believed that the tin in tin chloride somehow reacts with the oxides in the glass to form a tin oxide coating on the glass. This coating can not be removed without severely damaging the glass substrate. Following is a list of points which we experimentally found to be important:

- 1) The areas of the glass which are not to be coated with tin oxide must be covered with aquadag prior to heating the glass.
- 2) The initial part of heating the tin chloride crystals will provide mostly moisture. Violent bubbling at this stage can cause undesirable "spit" marks on the glass. When the molten material begins to turn yellow, the white fumes which are produced are mostly tin chloride.
- 3) As puffs of air are passed over the molten tin chloride and spread over the glass, they cool the surface. Intermittent pauses to allow the glass to return to the proper temperature were found to be beneficial.

- 4) The tin oxide coating on the glass produces colored fringes of light by which it can be detected. If no fringes are observed, the glass was probably underheated. It can be reheated for a second try. If light fringes are observed, but the surface is non-conductive, the coating was probably overheated to above  $500^{\circ}\text{C}$ . The process must then be repeated on a new piece of glass, since the loss of conductivity of overheated tin oxide is irreversible.

#### H.2) Deposition of Phosphor Powder on the Screen

We have followed the procedure described by Müller (45) for deposition of phosphor powder on fluorescent screens. In this procedure the phosphor is very loosely bound to the glass, and it can be easily wiped off. A solution of glycerine and alcohol is used to wet the surface of the screen over which puffs of air mixed with phosphor dust are passed. After enough phosphor has been deposited, the screen is baked in an oven so that the binder evaporates off. Some of our findings in using this procedure are listed below.

- 1) In order for the wetting agent to spread uniformly and not form droplets over the glass, the surface of the glass must be cleaned very thoroughly. We have found that three hours in a warm solution of Micro<sup>T.M.</sup> laboratory cleaner cleans the glass surfaces rather well.

- 2) Five or six drops of a solution of 200 proof ethanol mixed with glycerine (2 to 1) proved to be sufficient to wet a 3 inch diameter screen. Excessive amounts of this wetting agent cause the particles of the phosphor to float together and form large grains. In order to avoid grain size differences on the screen, it is also essential to lay the screen on a very flat surface during the phosphor deposition and the subsequent bakeout.
- 3) The recommended amount of phosphor to be deposited is given as 1 to 2 mg/cm<sup>2</sup> (45). However, with our method of mixing phosphor dust with air, it is not possible to measure the weight of the deposited phosphor. Therefore, we place a white sheet of paper covered with black crossmarks under the screen, and when the crossmarks are just not visible through the phosphor, deposition is considered to be completed.
- 4) The final step is to bake the screen in air. We have found that about six hours at 75°C evaporates the wetting agent gently enough so that no bubbles are formed. It is important to remember that while the wetting agent is on the screen, it is very prone to picking up dirt from the surroundings. Proper precautions against this are, therefore, essential.
- 5) We have used two kinds of common screen phosphor materials, both of which were obtained from

Sylvania Corp.: Manganese activated zinc orthosilicate ( $\text{Zn}_2\text{SiO}_4\text{:Mn}$ --also commercially known as the mineral willemite--Sylvania phosphor type 160), and silver activated zinc sulfide ( $\text{ZnS:Ag}$ --Sylvania phosphor type 1310). When the incident particles are ions (e.g. in a FIM without the channel plate) willemite is preferred over zinc sulfide, since it deteriorates much slower under the impact of heavy incident particles, but has a high light emitting efficiency, and most photographic films are more sensitive to its blue emission. Therefore, we have used zinc sulfide on the screens which are used with a channel plate, since here the particles incident on the screen are electrons.

### H.3) Preparation of FIM Samples

In this part we will describe the method that we presently use to prepare tungsten FIM samples. This method is called the "floating layer" technique, and has been described by Muller (46). Unfortunately, unless certain precautions are taken, it often produces plastically deformed tips which yield "streaky" FIM images. However, we received very useful suggestions from the Cornell group of Profs. Seidman and Balluffi on how such plastic deformations can be largely avoided.

Following is an outline of our present procedure for electropolishing tungsten FIM specimens:

- 1) If the wire from which the sample is to be made has

been mechanically cut (e.g. with scissors), a few millimeters of the wire near the ends which have been strained must be etched off. One way is to electropolish the ends off in a 5 wt% of NaOH.

A much quicker way that we have found is to etch the ends in an acid solution of 67% HF and 33% HNO<sub>3</sub>.

The speed of this etchant is largely determined by the concentration of the HF used in the solution.

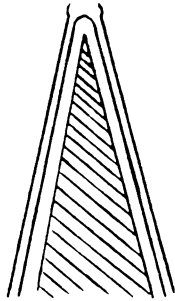
For example, a 2 mil diameter tungsten wire can be etched away in either 2 or 12 seconds depending on whether the concentration of the HF is 60% or 48%.

- 2) A beaker is partially filled with CCl<sub>4</sub>, and a 2-4mm thick layer of 10 wt% NaOH and glycerine (2 to 1) electrolyte is allowed to float over the surface of the CCl<sub>4</sub>.
- 3) The sample wire is inserted into the beaker in such a way that it hangs perfectly vertical, and its end protrudes about 1/2mm into the CCl<sub>4</sub> beneath the electrolyte. A voltage of 6vDC is then applied with the sample as the anode, and a stainless steel cathode. The sample is slowly moved up and down to smooth out the faster polishing at the electrolyte-air interface.
- 4) After a few minutes (e.g. two minutes for a 2-4 mil diameter wire), the voltage is turned off, and the sample is raised so that its end is well inside the electrolyte. The thickness of the electrolyte is

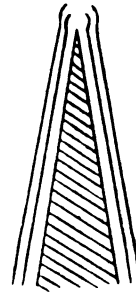
then increased (e.g. to 4-6mm) to allow deeper immersion of the sample.

- 5) While the sample is being carefully watched with a 15 to 100X microscope, the voltage is turned back on, and the sample is moved slowly up and down. After a few minutes differences in the thickness of the wire will indicate where it is most likely to break off. If this point is more than 1/2mm away from the end of the wire, the portion that will drop off is too large. The sample must then be raised until only the excess portion is in the electrolyte. After the excess portion has been polished off, the sample is lowered back into the electrolyte.
- 6) When the portion of the sample most likely to break off looks very thin, the voltage is cut off. Using a hand switch, it is turned back on and off quickly to produce a pulse of current ( $\approx 100\text{msec}$ ). The pulse is repeated until the 1/2mm end portion of the sample breaks off. At this point no more pulses should be applied, or serious blunting of the tip will result.
- 7) If the sample tip is inspected under a 400-600X microscope, the Fresnel fringes around the contour of the sample can help determine its adequacy as a FIM sample. Four possibilities are examined below (see Figure IV-7).
  - a) The fringes clearly go around the tip cap

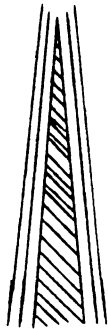




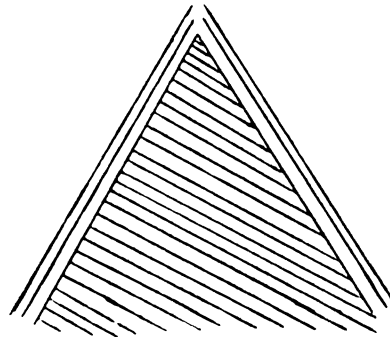
(a) Blunt



(b) Probably blunt



(c) Probably sharp



(d) (?)

FIGURE IV-7: EXAMINATION OF FIM TIPS BY OBSERVATION OF FRESNEL FRINGES (SHOWN GREATLY EXAGGERATED) AROUND THE TIPS.



(Figure IV-7(a)); the tip is blunt.

b) The fringes do not completely go around the tip cap, but they show a curvature in that direction

(Figure IV-7(b)); the tip is probably blunt.

c) The fringes end at the same point that the tip of the sample fades out (due to the resolution limit of the microscope) while they are still parallel with the sample (Figure IV-7(c)); the tip is probably sharp, i.e. it is adequate as a FIM sample.

d) If the sample has a large cone angle (as would be obtained with a shallow immersion in step 4 above), the fringes at the tip will usually be seen to converge to a point (Figure IV-7(d)) regardless of the tip geometry; the usefulness of the sample tip remains uncertain.

#### J. Data Acquisition and Analysis System

The data acquisition and analysis system which is coupled to our FIM consists of a high voltage pulsing network for controlled field evaporation of the FIM sample, still and motion picture cameras for recording the FIM images, and a motion picture analyzer for quantitative analysis of the data. The combination of these allows us to dissect the FIM tip at an average rate of less than one atom per pulse (the small rate of evaporation is necessary to ensure that few, if any, spurious defects are generated by the evaporation process), obtain a



picture for each pulse, and after observing thousands of such pictures, arrive at statistically reliable information regarding defect concentrations in the tip material.

#### J.1) Data Acquisition System

Figure IV-8 shows a block diagram of our data acquisition system. The movie camera which is focused on the FIM screen is an Automax model G-4SD 35mm camera which operates on +28vDC command pulses for opening and closing the shutter and advancing the film; it has 400ft film capacity magazines. One of its special features is a data box which can record, along the edge of each frame of film, the image of a frame counter, a data sheet (on which information such as the data, type of specimen, etc. can be written), and an object (e.g. a small clock) which can be placed on the frame counter. This feature is particularly valuable for data analysis purposes. The camera control circuit generates pulses which control the exposure time (0-12 sec. continuous) and the time interval between two successive frames (.05-1 sec. stepwise), when it is in the automatic mode. In the manual mode the operator controls the operation of the camera.

The open pulse command going to the camera opens the shutter, and advances the frame counter inside the camera. The close pulse command closes the shutter, and is also fed to the pulse shaper circuits where it is shaped to a square wave of variable duration (0-0.1 sec.),

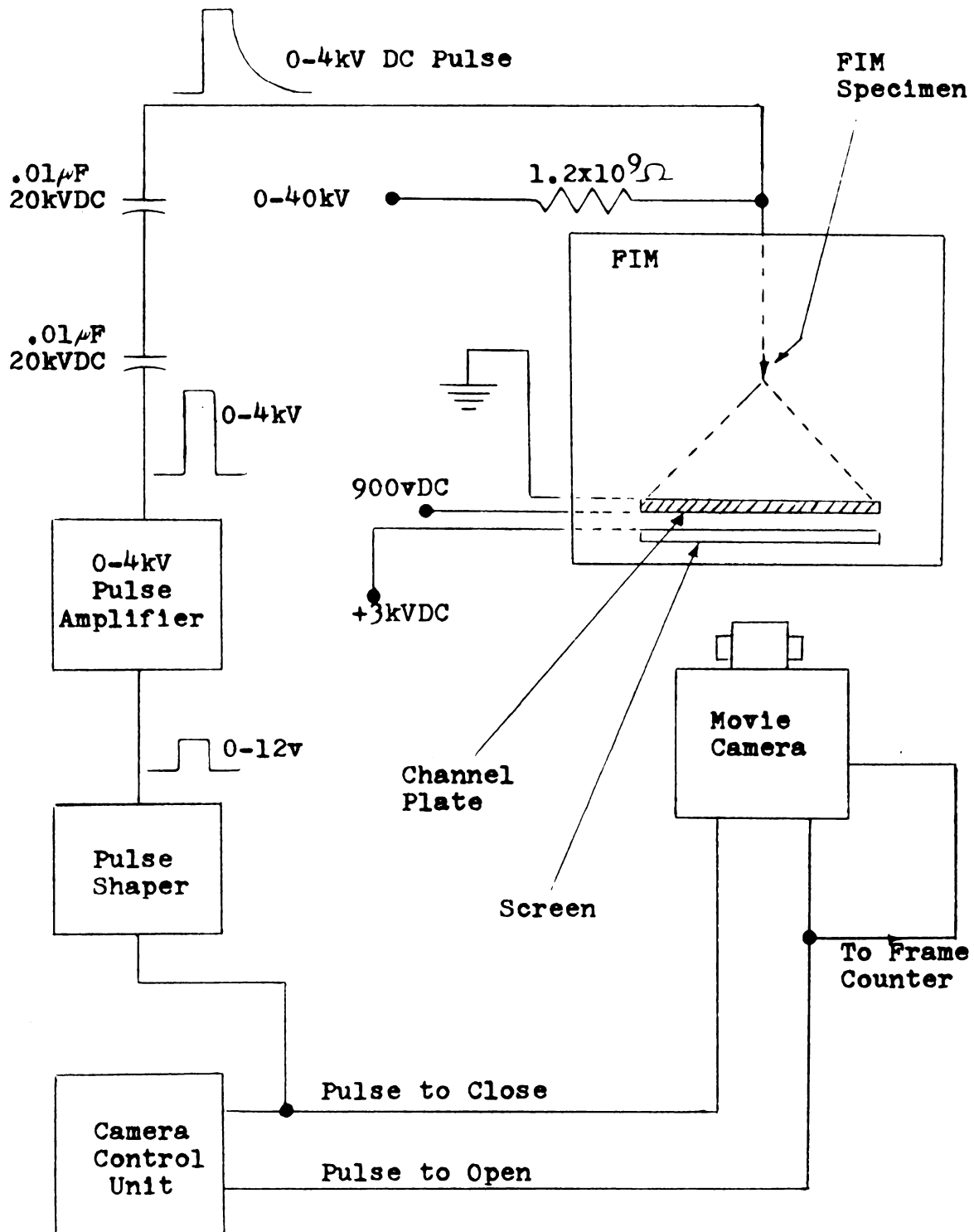


FIGURE IV-8: BLOCK DIAGRAM OF THE DATA AQUISITION SYSTEM.

delayed by a pre-set amount (0-0.2 sec.), attenuated, and finally coupled to the high voltage pulse amplifier. This amplifier is a slightly modified version of one designed by Robertson, et al (47). The pulse from this amplifier is capacitively coupled to the FIM sample, which is also connected to a Spellman 0-  $\pm$  40kV power supply through a current limiting resistor. The voltage from this power supply is used to image the FIM tip, and to modify the initial configuration of the tip to a final hemispherical end-form by slowly field evaporating the surface atoms\* (see Appendix A--Field Evaporation). At this point the voltage is reduced to the best image voltage, the camera is positioned in front of the screen, and further field evaporation will be by application of the high voltage pulses from the pulse amplifier.

The procedure used for setting up the experimental equipment, for controlled field evaporation of the tip atoms, and for recording of the data on film is outlined below:

- 1) Before loading the film, the camera is opened and a

---

\*Field evaporation of the FIM tip must be carried out very slowly to reduce the possibility of mechanical breakdown of the sample. To allow a finer control over the applied voltage, we have added a remote control unit to our 40kV power supply which allows setting of the voltage from 0 to 16kV to within  $\pm$  8v and from 16 to 32kV to within  $\pm$  16v, (internal control of the power supply is from 0 to 40kV to within  $\pm$  40v). The remote control unit is conveniently located on a mobile cart next to the platform on which the camera is mounted. This platform is built on the remnants of an old milling machine and can be positioned to within 0.001 inch in three dimensions.





piece of lucite is placed in the position usually occupied by the film. By observing the lucite through a short range ( $\approx 50\text{cm}$ ) telescope, and shining a flashlight on the FIM screen, the camera is focused such that a sharp image of the phosphor grains on the screen is obtained on the lucite.

2) Since during a typical experimental run, 1000 feet or more of film may be used, the exposure time and the focusing of the camera and even the best image voltage applied to the tip must be optimized to ensure that the recording of the image is under the best possible conditions. Therefore, after the film is loaded in the camera, a number of pictures of the FIM image are taken at various exposure times centered about a "best guess" value known from experience. Similarly, with the exposure time set at the "best guess" value, a number of pictures are taken at various focus settings centered about the setting found in step 1 above, and with various best image voltages centered about the value which produces the sharpest image as seen by eye.\* The exposed portion of the film is then cut off and developed in a darkroom. After the negative is dry, the pictures are observed in

---

\*There appears to be a small difference between the value of the applied voltage which produces the sharpest image as recorded by the film, and that as seen by eye.



the data analyzer (see Section J.2 below), and the best values for the above parameters are chosen.

3) The camera control is set for the proper exposure time and the desired number of frames per second (e.g. 0.5 sec. exposure at 1 frame/sec.), and the amplitude and the duration of the high voltage pulse are varied until the atoms on any given plane of interest are evaporating at a rate of one per every two to three frames (or pulses) (a typical pulse  $\sim 1\text{kV}$ ,  $\sim 20\text{msec}$ ). The process of field evaporation and the simultaneous recording of the data can be continued at this rate until the tip becomes blunted and the resolution of the FIM becomes unsatisfactory.

Besides the movie camera described above, a Polaroid scope camera and a Honeywell Pentax H-1A 35mm camera are also used for recording the FIM images for other than quantitative analysis purposes. There are two Super-Takumar lenses ( $f = 1.2$  and  $f = 2.0$ ) which are used interchangeably on the Honeywell Pentax and the Automax movie camera.

## J.2) Data Analysis System

This system consists of a Vanguard Model M-35CF/S-1 35mm flickerless\* projector. The 35mm film containing

---

\*The flicker which occurs in a normal projector for film speeds lower than 16 frames per second can cause eyestrain on the operator, thereby increasing the chances for human error in the analysis. The resulting fatigue also makes viewing of the films for more than a few minutes at a time rather difficult.



the data is developed in negative form, and displayed on this projector. The projector has provisions for both cine projection (with speeds continuously variable from 1 to 24 frames/sec) and frame by frame stepping, in both forward and reverse directions. The camera can be stopped at any frame for detailed examination of the image.

Slow cine projection is crucial for detection of individual defects, since the defect can be followed through a series of frames, from appearance to disappearance, thereby greatly increasing the signal to noise ratio relative to that for observation from a single frame. It is particularly difficult with single pictures to be sure of the existence of vacancies in the interior of low index planes, since only the atoms on the plane boundaries stand out clearly. However, since these boundary atoms are least tightly bound, they will be removed first during slow field evaporation, thereby converting the interior atoms into boundary atoms for a smaller portion of the plane, and making them--or any defects--visible. Slow cine projection allows this entire process to be followed in detail for each defect.



## LIST OF REFERENCES





## LIST OF REFERENCES

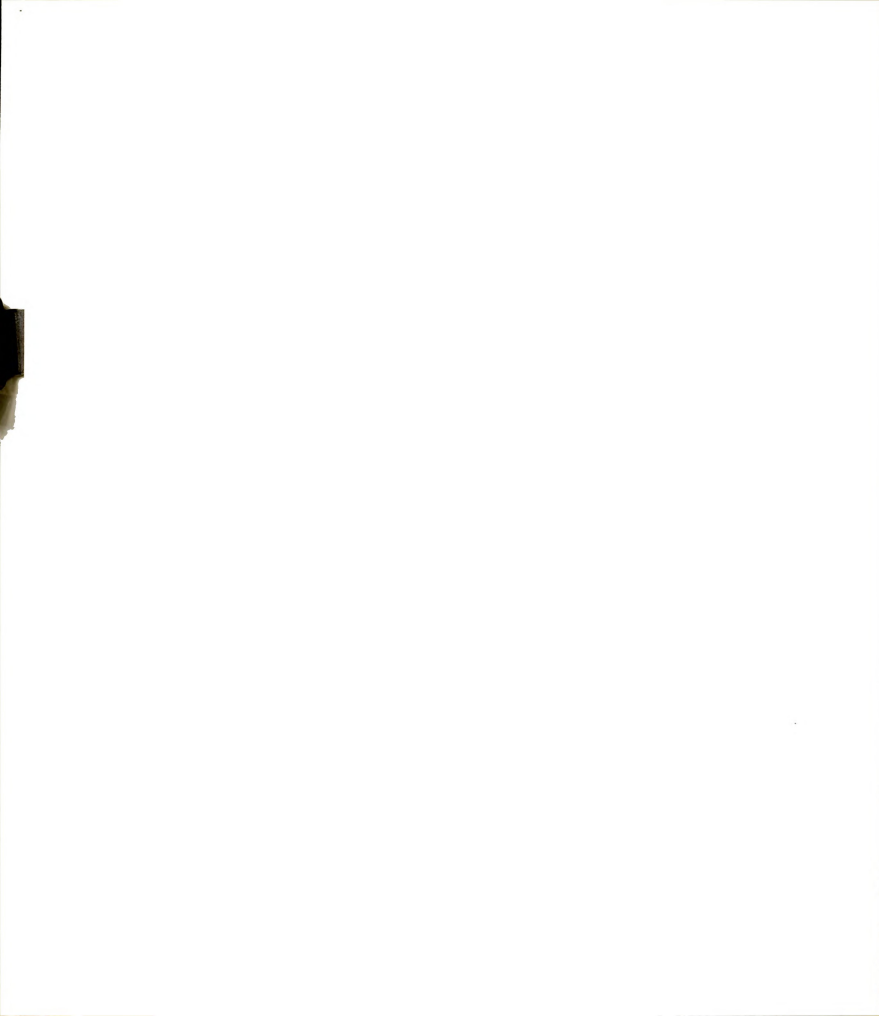
1. Pawel, R. E., and Lundy, T. S., Acta Met. 17, 979 (1969).
2. Robinson, S. L., and Sherby, O. D., Acta Met., 17, 109 (1969).
3. Evans, J. H., and Eyre, B. L., Acta Met. 17, 1109 (1969).
4. Burke, P., and Kothe, A., and Werth, R. R., Phys. Stat. Sol. 36, K171 (1969).
5. Lidiard, A. B., Comm. Sol. St. Phys. III, 116 (1970).
6. Smithells, C. J. Metals Reference Book, Interscience Publishers Inc., New York (1955), p. 534.
7. Kimura, H., (to be published).
8. Evans, J. H., Phil. Mag. 22, 1261 (1970).
9. Simmons, R. O., and Balluffi, R. W., Phys. Rev. 125, 862 (1962).
10. Cotterill, R. M. J., Lattice Defects in Quenched Metals, ed. by R. M. R. Cotterill, Academic Press, New York (1965), p. 97.
11. Kraftmakher, Ya. A., Soviet Physics--Solid State (USA) 4, 1662 (1963).
12. Gripshover, R. J., Ph.D. Thesis, Michigan State University, 1969.
13. Girifalco, L. A., Atomic Migration in Crystals, Blaisdell Publishing Company, New York (1964).
14. Lazarus, D., Phys. Rev. 93, 973 (1964).
15. Rinderer, L., and Schultz, H., Physics Lett. 8, 14 (1964).



16. Kuhlmann, H. H., and Schultz, H., Z Naturf. A 19, 586 (1964); Acta Met. 14, 798 (1966).
17. Temperature, Its Measurement and Control in Science and Industry, Reinhold Publ. Co., New York, (1941), p. 1318.
18. Jones, H. A., and Langmuir, I., Gen. Elec. Rev. 30, 310 (1927).
19. Schultz, H., Acta Met. 12, 761 (1964).
20. Schultz, H., Lattice Defects in Quenched Metals, ed. by R. M. J. Cotterill et al., Academic Press inc., New York (1965), p. 761.
21. Flynn, C. P., Bass, J., and Lazarus, D., Phil. Mag. 11, 521 (1965).
22. Mori, T., Meshii, M., and Kauffman, J. W., J. Appl. Phys. 33, 1671 (1962).
23. Jeannotte, D., and Galligan, J. M., Phys. Rev. Lett. 19, 232 (1967).
24. Flynn, C. P., Phys Rev. 171, 682 (1968).
25. Bauerle, J. E., and Koehler, J. S., Phys. Rev. 107, 1493 (1957).
26. DeJong, M., and Koehler, J. S., Phys. Rev. 129, 49 (1963).
27. Ytterhus, J. A., and Balluffi, R. W., Phil. Mag. 11, 707 (1965).
28. Goldschmidt, H. J., and Brand, J. A., J. less-common Metals 5, 181, (1963).
29. Jortner, J., Meyer, L., Rice, S. A., and Wilson, E. G., Phys. Rev. Lett. 12, 415 (1964).
30. Kunz, W. and Schultz, H., Report on Experiments on Quenched W, presented at Discussion Meeting on Defects in Refractory Metals, Mol/Belgium, Sept., 1971.
31. Müller, E. W., Z. Physik 131, 136 (1951).
32. Müller, E. W., and Tsong, T. T., Field Ion Microscopy: Principles and Applications, American Elsevier Publ. Co., New York, (1969) p. 126.



33. DuBroff, W., and Machlin, E. S., *Acta Met.* 16, 1313 (1968).
34. Bargery, C. J., Adam, J., and Riviere, J. C., *J. Sci. Instru.* 44, 692 (1967).
35. Müller, E. W., and Tsong, T. T., Field Ion Microscopy: Principles and Applications, American Elsevier Publ. Co., New York, (1969), p. 105.
36. Müller, E. W., Nishikawa, O., *Rev. Sci. Instr.* 36, 556 (1965).
37. Weizer, V. G., *J. Appl. Phys.* 36, 2090 (1965).
38. Brandon, D. G., Ranganathan, S., and Whitmell, D. S., *Brit. J. Appl. Phys.* 15, 55 (1964).
39. Wacławski, B. J., and Müller, E. W., *J. Appl. Phys.* 32, 1472 (1961).
40. Boyes, E. D., and Elvin, C. D., *J. Sci. Instrum.* 44, 223 (1967).
41. Brenner, S. S., *Rev. Sci. Instrum.* 39, 588 (1968).
42. McLane, S. B., Müller, E. W., and Nishikawa, O., *Rev. Sci. Instrum.* 35, 1297 (1964).
43. Scanlan, R. M., Styris, D. L., Seidman, D. N., and Ast, D. G., Report #1159 of the Materials Science Center, Cornell Univ. (1969).
44. Gomer, R., *Rev. Sci. Instr.* 24, 993 (1953).
45. Müller, E. W., and Tsong, T. T., Field Ion Microscopy: Principles and Applications, American Elsevier Publ. Co., New York (1969), p. 139.
46. Müller, E. W., and Tsong, T. T., Field Ion Microscopy: Principles and Applications, American Elsevier Publ. Co., New York (1969), p. 123.
47. Robertson, S. H., and Seidman, D. N., *J. Sci. Instr. series 2*, vol. 1, 1244 (1968).
48. Müller, E. W., and Tsong, T. T., Field Ion Microscopy: Principles and Applications, American Elsevier Publ. Co., New York (1969), p. 41.
49. Oppenheimer, J. R., *Phys. Rev.* 31, 67 (1928).



50. Messiah, A., Quantum Mechanics, Interscience Publishers, New York (1962).
51. Müller, E. W., and Tsong, T. T., Field Ion Microscopy: Principles and Applications, American Elsevier Publ. Co., New York, (1969) p. 44.
52. Müller, E. W., J. Appl. Phys. 28, 1 (1957).
53. Mulson, J. F., and Müller, E. W., J. Chem Phys. 38, 2615 (1963).





## APPENDIX



## APPENDIX A

### BASIC PRINCIPLES OF THE FIELD ION MICROSCOPE

To assist the reader in understanding the operation of the field ion microscope, a brief description of the basic apparatus and the principles involved in its operation are given below.

#### I. The Basic Apparatus

Figure A-1 illustrates the major features of a simple glass FIM. The fundamental constituents of the microscope are: 1) a specimen in the form of a wire with a very fine hemispherical tip of diameter 100 to 1000 $\text{\AA}$ ; 2) a power supply to raise the sample to high electrical potential; 3) an imaging gas (usually He) which will ionize in a sufficiently high electric field, yielding ions which move out along field lines to strike a fluorescent screen; and 4) a fluorescent screen which provides from each region a light output proportional to the number of ions striking that region. As we will describe below, the imaging gas atoms are ionized preferentially at locations directly over atomic sites of the sample tip; the ions then move out radially along field lines and strike the



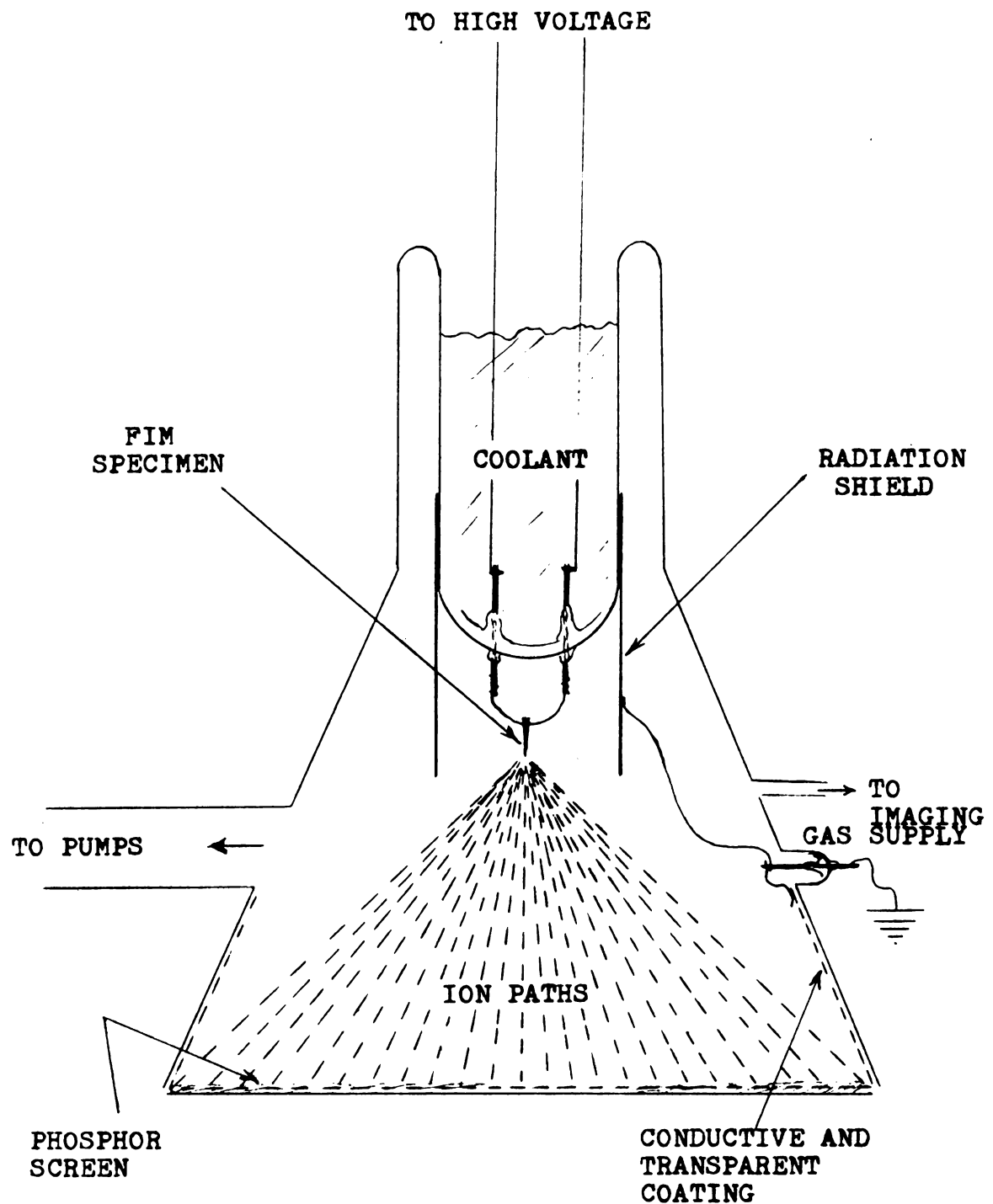


FIGURE A-1: SCHEMATIC DIAGRAM OF A GLASS FIELD ION MICROSCOPE.



fluorescent screen, producing thereon a greatly magnified image of the tip. The magnification of the microscope is purely geometric, and is given by

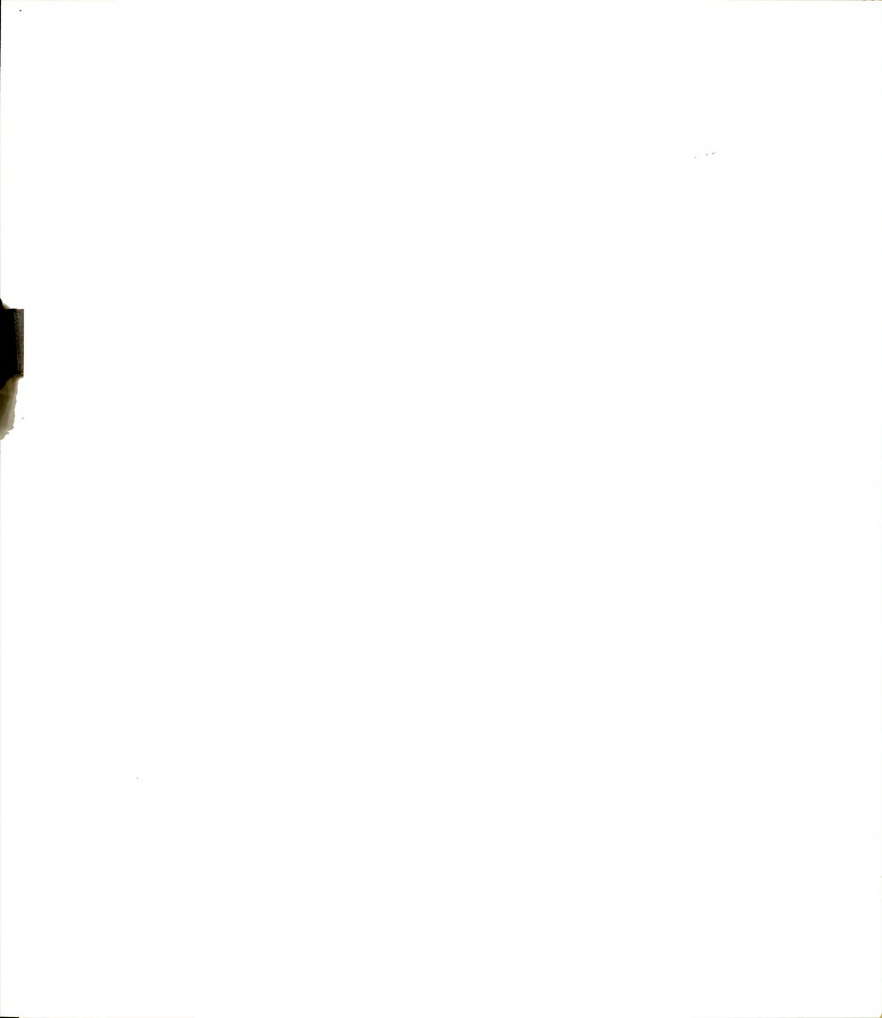
$$M = \frac{R}{\beta r_t} \quad (1)$$

where  $R$  is the distance from the tip to the screen,  $r_t$  is the tip radius and  $\beta$  is a geometrical factor (typical values 1.5 to 1.8 (48)). For typical values of  $R = 4\text{cm}$ ,  $r_t = 400\text{\AA}$ , a magnification of about  $6 \times 10^5$  or more can be obtained (at the expense of image intensity), but this will not result in any improvement in resolution. As we will discuss below, the resolution of the FIM is independent of  $R$  and depends on other variables. It is for optimizing these variables that the major features of the FIM are selected as those shown in Figure A-1.

We now describe in more detail the physical principles upon which the microscope operates:

## II. Field Ionization

The physical effect responsible for the operation of the microscope is quantum mechanical tunneling, as first envisioned by Oppenheimer (49). When a free neutral atom enters a region of high electric field in space, its outer electron has a non-zero probability of tunneling out and field ionizing the atom in the process. Figure A-2(a) shows a simplified one-dimensional potential energy





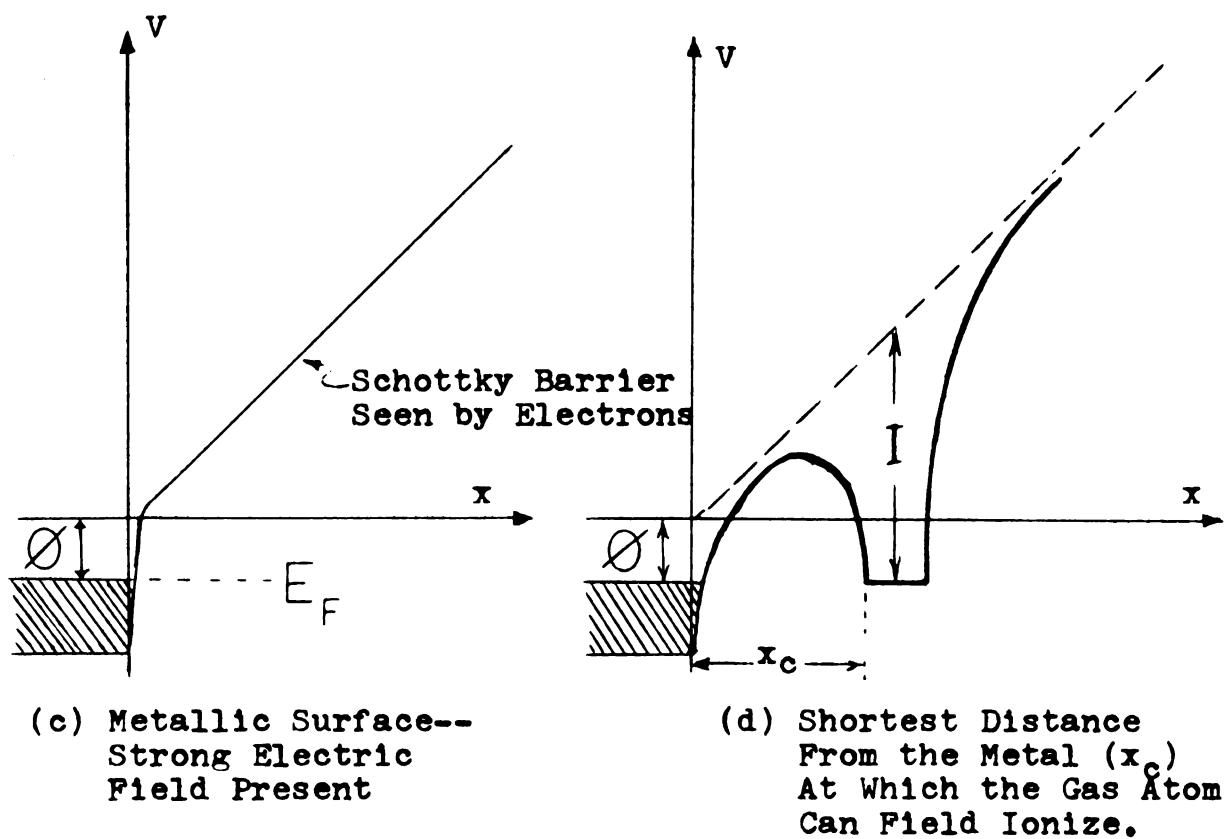
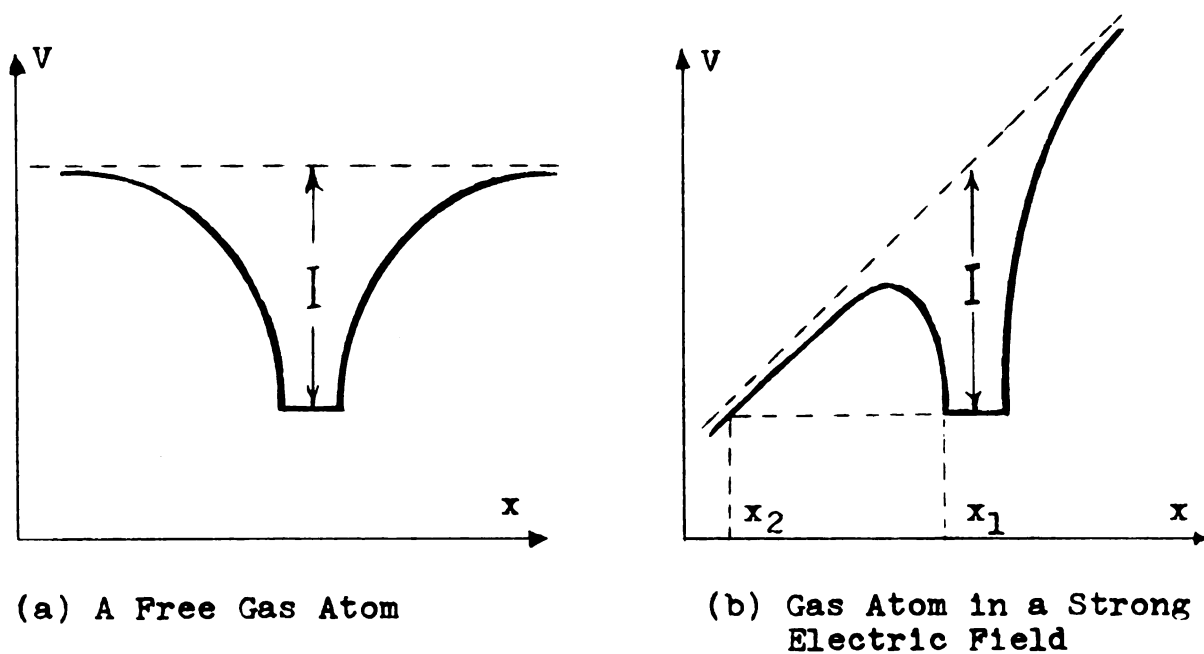


FIGURE A-2: ONE DIMENSIONAL POTENTIAL ENERGY DIAGRAMS FOR FIELD IONIZATION.



diagram for a ground state outer electron in the potential well of a gas atom with ionization energy  $I$ . The distorted potential well of the same atom in a strong electric field is shown in Figure A-2(b). The width of the potential barrier (between  $x_1$  and  $x_2$ ) and its form can be used (by W.K.B. Approximation (50)) to calculate tunneling probabilities for the electron.

The necessary electric field for field ionizing gases in a finite time is of the order of several hundred million volts per centimeter (e.g. 440MV/cm for helium). In 1951 Müller (31) was able to field ionize hydrogen by creating the necessary electric field applying only modest voltages to a sharply pointed tip of a tungsten specimen. At the same time, he discovered that field ionization over the surface of the tip is extremely sensitive to atomic configuration of the surface. Field ionization near a metallic surface is complicated by the effect of the proximity of the conductor on the potential barrier of the electron. Qualitatively, the situation is shown in Figures A-2(c) and A-2(d).

The Schottky barrier as seen by the conduction electrons at the surface of a metal (with work function  $\phi$ ) after the application of a large positive potential is shown in Figure A-2(c). As the imaging gas atom approaches the surface of the metal, the width of the potential barrier for the electron decreases with a resulting increase in the tunneling probability. When the ground state



energy of the electron reaches the top of the Fermi level ( $E_f$ ) in the metal, the ionization probability is a maximum (Figure A-2(d)). Beyond this critical distance the electron no longer can tunnel into the metal since its energy level sinks below the fully occupied Fermi sea of the metal. The ionization probability abruptly falls to zero, the electron is repelled from the surface, and the atom rebounds.

A rough calculation for helium as imaging gas over a tungsten tip yields a value of  $x_c \approx 4\text{\AA}$  for this critical distance.

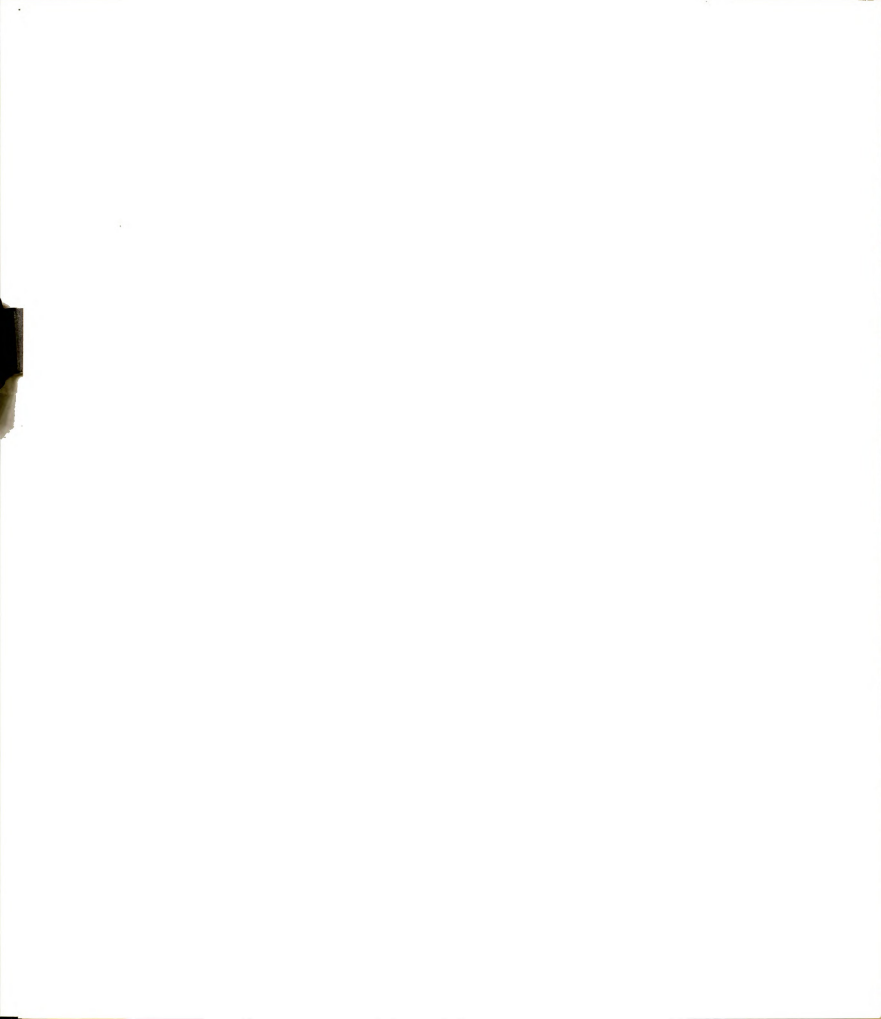
### III. Resolution of the FIM

A conventional field ion microscope operating at temperatures lower than 25K and with helium as imaging gas has a resolution which is often between 2 to  $3\text{\AA}$ , smaller than atomic separation on many crystallographic planes of metals. At present no completely rigorous theory for the calculation of the resolution exists, but a simplified model (51) yields the following result which serves as a very useful guide for estimating the resolution of the microscope.

$$\delta = \delta_0 + \left[ 4 \left( \frac{\beta^2 r_t^2 \hbar^2}{2eMV_0} \right)^{1/2} + 16 \left( \frac{\beta^2 r_t^2 kT}{eV_0} \right) \right]^{1/2} \quad (2)$$



Here  $\delta$  is the resolution and  $\delta_0$  is due to the effect of the size of the imaging gas atom and is assumed to be of the order of the atomic radius of the imaging gas. The variables given in the above formula are the best image voltage  $V_0$ , the tip radius  $r_t$ , the mass of the imaging gas atom  $M$ , and the effective temperature of the gas  $T$ . Electron charge ( $e$ ), Boltzman constant ( $k$ ) and Planck's constant divided by  $2\pi(\hbar)$  are known constants. The first term in the brackets is due to the increased uncertainty in the tangential momentum of the gas atom as it becomes localized (Heizenberg's Uncertainty Principle). The second term is due to the tangential velocity of the gas atom at effective temperature  $T$  due to its thermal energy. This effective temperature is usually much higher than that of the entire imaging gas, which is at near room temperature. The kinetic energy of the gas atoms approaching the tip increases due to their dipole attraction toward the tip surface, and their subsequent diffuse rebounds are responsible for an effective rise of the temperature of the gas in the vicinity of the FIM tip. The coolant bath shown in Figure A-1 is for the purpose of reducing this effective temperature of the imaging gas at the instant of ionization. Since the imaging gas atoms make several rebounds on the average before ionizing, their temperature approaches that of the tip rapidly. Therefore, cooling the tip can improve the resolution of the FIM.





From Equation 2, we can list the following in the order of their efficiency in reducing the resolution  $\delta$ :

- 1) Working with tips of small radius  $r_t$ .
- 2) Using an imaging gas of smallest atomic radius (to reduce  $\delta_0$ ).
- 3) Using an imaging gas of very high ionization potential (large  $V_0$ ).
- 4) Reducing the temperature of the tip.
- 5) Using an imaging gas of a large mass  $M$ .

Because helium has the smallest atomic radius and the largest ionization potential of all gases (#2 and #3), it is usually picked as the imaging gas, despite its small atomic mass (#5).

#### IV. Focusing

Projection of the field ionized gas atoms along the radially outward electric field lines in a FIM automatically insures that the FIM is basically focused at all times. Therefore, any attempt to improve the resolution when the microscope is operating can be thought of as "fine focusing". From Equation 2 we see that  $\delta_0$  and the Heizenberg uncertainty terms are fixed by the imaging gas and the tip radius. Therefore, the only "focusing" applicable may be done by controlling the tip temperature.

Contrary to what may seem from Equation 2, the lowest possible tip temperature does not always lead to the smallest resolution. In the qualitative argument given



below we explore why for a given tip material and imaging gas there exists an optimum range of tip temperatures for best resolution.

Figure A-3 shows (after Müller (52)) the surface of the FIM tip as the very high electric field at the surface has partially drawn back the conduction electrons into the metal, exposing the positive ion cores of the surface atoms. The ionization probability for the gas atoms over the surface is indicated by the density of the contour lines. For example, the ionization is maximum directly over the atoms at the edge of net planes and increases towards the critical distance  $x_c$ . Below  $x_c$  no contour lines are shown since this is the forbidden ionization zone. As shown in Figure A-3, the impression of the surface structure on the ionization probability density is also maximum at  $x_c$ , i.e., gas atoms ionizing high above  $x_c$  do not contribute much to the resolution of the microscope.

As the incoming gas atom A approaches the metal, its normal velocity component given by  $F(\alpha/M)^{1/2}$  ( $F$  = electric field,  $M$  = mass of A,  $\alpha$  = polarizability of A), increases rapidly. We consider the following three cases:

- 1) Tip temperature is too high (e.g. 100K or higher).

The atom will diffusely rebound without losing enough of its kinetic energy (shown as B). If it ionizes, it will have a large tangential velocity with the resulting loss of resolution.

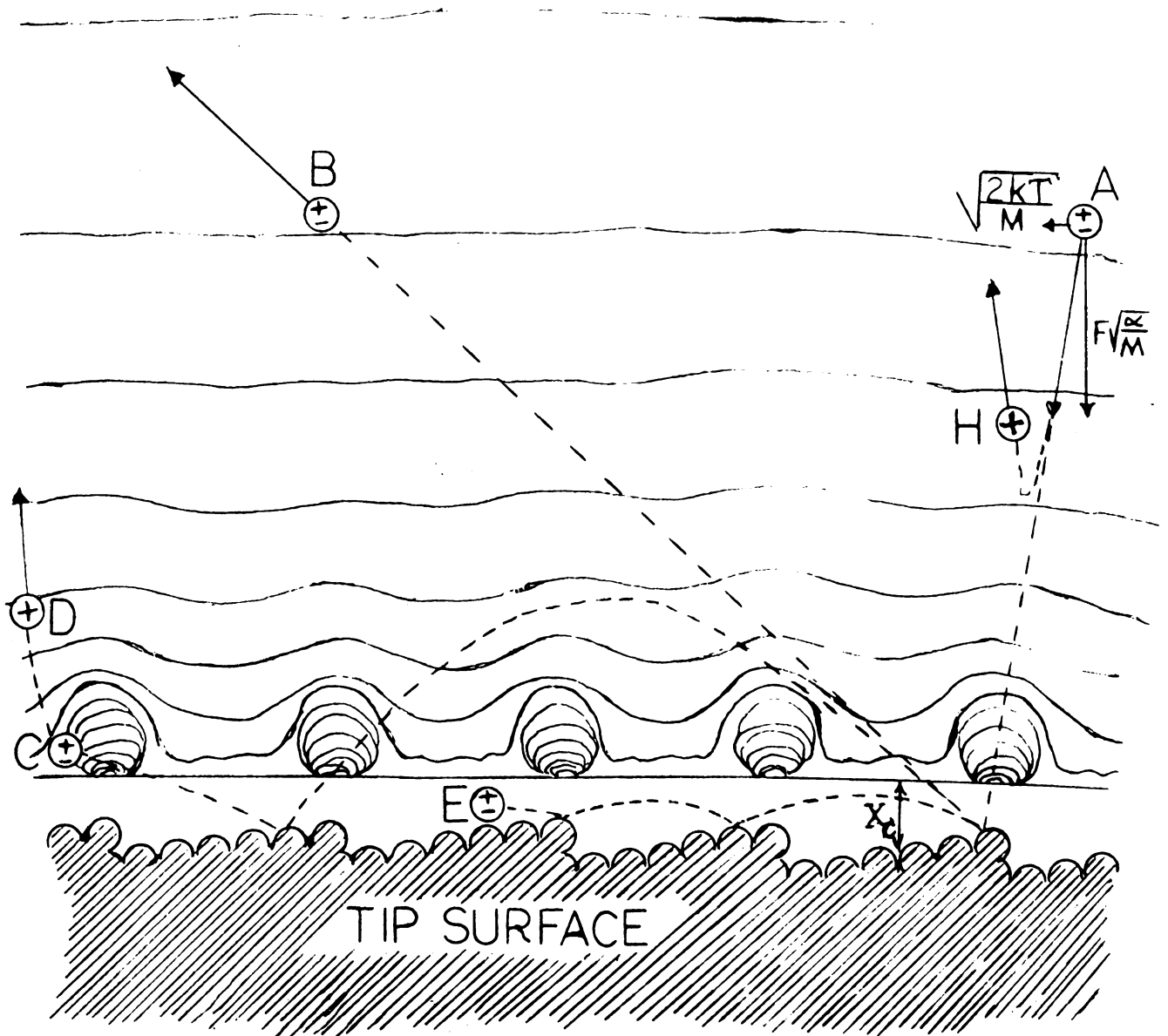
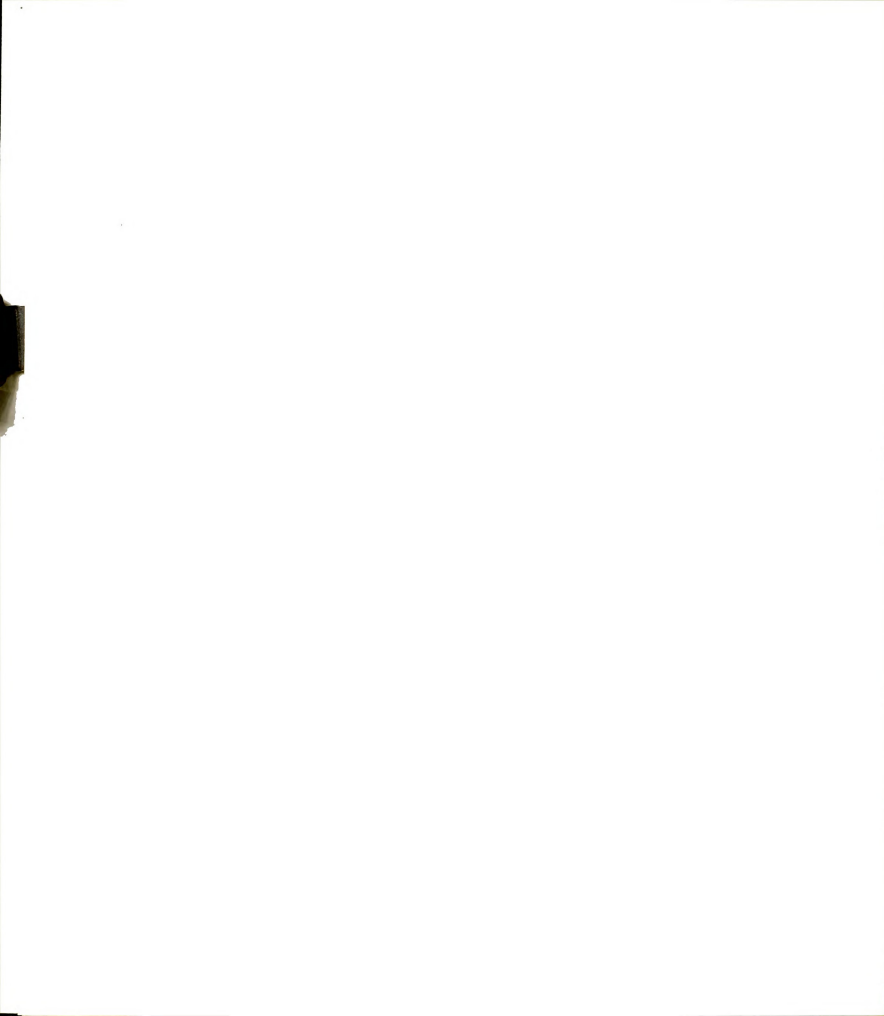


FIGURE A-3: (AFTER MULLER), MOTION OF THE IMAGING GAS ATOMS NEAR THE TIP SURFACE.



- 2) Tip temperature is sufficiently low (5 to 20K for He on tungsten)

The incoming atom loses enough of its kinetic energy on the first rebound that it will be pulled back to the surface by dipole attraction for more rebounds losing more energy. If it ionizes, it will be close to the surface (shown as C) and the ion (shown as D) will travel near normal to the surface.

- 3) Tip temperature is too low (e.g. 4.2K for neon as imaging gas)

The incoming atom may "condense" on the tip surface (shown as E) and will not be able to ionize (below  $x_c$ ). Moreover, the FIM image is then mostly formed by atoms like H ionizing upon their first approach and partly at large distances from the tip. Degradation of the resolution results from either or both of these effects.

## V. Field Evaporation

Next to the process of field ionization, field evaporation is the most important physical effect in field ion microscopy. It is a process in which an atom on the surface of the FIM tip tunnels out of the metal leaving one or more of its electrons behind.

The two factors which most strongly affect the rate of field evaporation are the electric field at the surface and the tip temperature. In this case the electric field shapes the potential barrier through which the atom



has to tunnel, and the tip temperature determines the frequency with which the atom strikes the barrier.

Following is a brief review of some of the most important aspects of field evaporation:

a) Resolution of a FIM is critically dependent on imaging by radial projection which requires a hemispherical, atomically smooth specimen. Conventionally prepared samples are far from such perfection, but they can be field evaporated to nearly perfect end forms. Microprotrusions and nonuniformities on the surface create extremely high local electric fields causing the atoms forming these nonuniformities to field evaporate.

b) The surface of the specimen would normally be covered with impurity atoms left from handling and preparation. Field desorption (term used when the evaporated atom is an impurity) clears the surface of such impurities.

c) The evaporation field is nearly constant for a given tip material, with variations coming from impurities. Since the field necessary for obtaining a FIM image is determined by what imaging gas is used, it is clear that for observing a stable image of a specimen, its evaporation field must exceed the ionization field of the imaging gas. For example, with He (ionization field =  $4.4\text{v}/\text{\AA}$ ) as the imaging gas, no stable image of gold (evaporation field =  $3.5\text{v}/\text{\AA}$ ) can be obtained.

Field induced chemical reactions have so far plagued efforts to observe easily evaporating materials by using





non-inert, low ionization field gases as the imaging gas. The effect of field induced reactions on the FIM image can be observed in a FIM using an inert imaging gas if the microscope has not been properly evacuated prior to the introduction of the imaging gas. The contaminant gases remaining in the microscope chemically etch the surface of the tip at a greatly enhanced rate due to the electric field, resulting in very unstable images (53). For this reason conventional FIMs are equipped with a sophisticated pumping system and are bakeable so that they can be pumped down to ultra-high vacuum ( $p < 10^{-8}$  torr) before the very pure imaging gas ( $p \approx 10^{-3}$  torr) is introduced.







MICHIGAN STATE UNIVERSITY LIBRARIES



3 1293 03062 2306